FLORIDA INTERNATIONAL UNIVERSITY

Miami, Florida

NOVEL PROCESSING AND FUNDAMENTALS FOR HIGH TEMPERATURE NITRIDE CERAMICS

A dissertation submitted in partial fulfillment of

the requirements for the degree of

DOCTOR OF PHILOSOPHY

in

MATERIALS SCIENCE AND ENGINEERING

by

Suprabha Das

2024

To: Interim Dean Ines Triay Melendez
College of Engineering and Computing

This dissertation, written by Suprabha Das, and entitled Novel Processing and Fundamentals for High Temperature Nitride Ceramics, having been approved with respect to style and intellectual content, is referred to you for judgment.

We have read this dissertation and recommend that it be approved.

Nezih Pala

Vadym Drozd

Andriy Durygin

Chunlei Wang

Zhe Cheng, Major Professor

Date of Defense: February 28, 2024

The dissertation of Suprabha Das is approved.

Interim Dean Ines Triay Melendez
College of Engineering and Computing

Andrés G. Gil
Senior Vice President for Research and Economic Development
and Dean of the University Graduate School

Florida International University, 2024

DEDICATION

I dedicate this thesis to my mom, Soma Das.

Without her encouragement, support, and love, the completion of this work would not have been possible.

ACKNOWLEDGMENTS

I am sincerely grateful to my advisor, Dr. Zhe Cheng, for graciously accepting me into his research group and providing me with the invaluable opportunity to pursue my Ph.D. I extend my deepest appreciation for his unwavering support, continuous guidance, and encouragement since the beginning of this academic journey. Working under his mentorship has not only enriched my academic knowledge but also honed essential skills ranging from meticulous result organization and presentation techniques to proficient time management, networking, and multitasking, ultimately shaping me into a more accomplished researcher. I always felt positive, motivated, inspired, and energized after a conversation with him.

I would like to express my heartfelt gratitude to my esteemed committee members, Dr. Vadym Drozd, Dr. Andriy Durygin, Dr. Chunlei Wang, and Dr. Nezih Pala, for their invaluable contributions, insightful suggestions, and continuous guidance throughout the entire research process.

I extend my thanks to the Advanced Materials Engineering Research (AMERI) and the Center for Study of Matter at Extreme Conditions (CeSMEC) at FIU. Special appreciation goes to Dr. Andriy Durygin and Dr. Vadym Drozd for their exceptional support and insightful conversations, serving as true inspirations.

I am grateful to the University Graduate School, FIU, for their support through the Dissertation Year Fellowship (DYF) awards, which have played a pivotal role in facilitating the completion of my doctoral studies. My sincere appreciation to everyone at the MME department who has been part of this transformative journey, contributing to its success.

I extend my heartfelt gratitude to my incredible lab mates, who transcended the bounds of mere colleagues and became a source of support and inspiration. A special thank you to Shariful, my steadfast cheerleader during challenging times; the lessons I learned from you about life are immeasurable. Amirali, Wenhao, Raiyan, and Kiyana, your willingness to share in my happiness and worries has been a tremendous comfort.

My appreciation also goes out to my Advenir friends—Namrata, Shahid, Aditya, Talha, Rakshith, Mayur, and Asim. Those days spent together undoubtedly constituted the best moments of my life. A heartfelt thanks to Denny for being an exceptional friend with the purest heart. Abhijith, Anil, Sohail, Arghyadeep, you have become integral parts of my journey, and the memories we created together will forever hold a special place in my heart.

To Divya, Rohan, and baby Aryan, you have been my family in the US from day one, a constant source of joy. Divya, your caring and nurturing presence in my life, both professionally and personally, has been like a mother. Taniya and Saurabh, your constant love and support have made every moment we shared very precious. Divya, Rohan, and Saurabh, I want to express my sincere gratitude for helping me adapt and acclimate to life in the US by generously sharing your own experiences. Shalini and Anil, I am grateful for your warm welcome and the love that surpassed all expectations. Your kindness and hospitality have made me feel not only accepted but cherished. I appreciate the love and support you've extended to me, and I am truly grateful for the moments we've shared together. Special thanks to the Gangwani family for including me in your special moments, making me feel loved and easing the longing for my family in India. Because of all of you, the distance from home felt a little less daunting.

Finally, I extend heartfelt gratitude to my parents, Soma and Pradip Das, and my brother Soumyadeep Das, for their unwavering faith in me and constant motivation throughout my pursuit of this goal. Their support played a pivotal role, making it possible for me be who I am. Mom, I owe everything I am to you. Hope I made you proud and will make you prouder.

I want to express my profound gratitude to Pranav, who has been the cornerstone of support throughout my Ph.D. journey, enabling me to pursue my dream. A simple "thank you" feels inadequate for the immense impact you've had in keeping my spirits high. Your unwavering support means more to me than words can convey. Thank you for being my rock and for sharing this journey with me. I couldn't have asked for a better partner.

I owe my thesis and graduation to my mother and Pranav.

ABSTRACT OF THE DISSERTATION

NOVEL PROCESSING AND FUNDAMENTALS FOR HIGH TEMPERATURE NITRIDE CERAMICS

by

Suprabha Das

Florida International University, 2024

Miami, Florida

Professor Zhe Cheng, Major Professor

The current research focuses on high temperature nitrides, from binary and ternary to high entropy. The goals are to study the synthesis and processing of representative transition metal nitrides and understand the relationships between composition, processing, microstructure, and their properties.

The first part of the study is focusing on the binary nitride of ZrN. It aims to demonstrate the synthesize of ZrN powders by a facile and low-cost urea route without using any solvent and understand the formation mechanism including the effects of different processing parameters such as metal to urea molar ratio, heat treatment temperature, and dwelling time on the product phase and stoichiometry. In addition, the synthesized ZrN powder was consolidated into fully dense single-phase bulk ceramic in a few minutes with a new flash sintering technique and the microstructure as well as properties such as hardness and oxidation resistance of the sintered ZrN were characterized.

Next, reactive flash sintering (RFS) of ternary metal nitrides TiZrN and TiAlN from TiN-ZrN and TiN-AlN mixtures were demonstrated. Phase transformation was tracked using both conventional XRD and *in situ* synchrotron study. Uniform $Ti_{0.57}Zr_{0.43}N$ solution formed in RFS and persisted upon cooling, while (Ti, Al) N solid solution formed at high temperature was unstable and went through a very quick phase separation in the cooling process.

Finally, novel bulk high entropy nitrides (HEN) such as, $(Al_{0.17}Nb_{0.17}Ta_{0.17}Ti_{0.32}Zr_{0.17})N$ have been successfully synthesized in just a few minutes using the RFS technique. The formation of a single-phase nitride solid solution was confirmed using both *ex situ* XRD and *in situ* synchrotron. Microscopy revealed a dense microstructure without noticeable segregation of elements. The bulk HEN display attractive mechanical property that combines high hardness with exceptional fracture toughness, a very attractive property in ceramics, which is attributed to layered microstructure despite cubic crystal lattice. Some other attractive properties include decent oxidation resistance and superconductivity.

This study provides better understanding of these important nitride materials and the related new technologies, which might help future industrial applications in many fields.

TABLE OF CONTENTS

CHAPTER PAGE

Chapter I: Introduction..1

Chapter II: Literature review 4
2.1. High temperature nitride ceramics...4
2.2 Binary nitride, ZrN...4
2.2.1. Synthesis of ZrN powder 5
2.2.1.1. Hydrogenation–nitridation of metal powders 6
2.2.1.2. Mechanochemical synthesis..7
2.2.1.3. Thermal reduction nitridation using reducing agent.....................................9
2.2.1.4. Benzene–thermal method...11
2.2.1.5. Self-propagating high-temperature synthesis, SHS 11
2.2.1.6. Direct carbothermic nitridation (CN)..13
2.2.1.7. Carbothermal reduction – nitridation methods (CRN) 16
2.2.1.8. Soft urea and modified soft urea method 17
2.2.2. Sintering of bulk ZrN...19
2.2.2.1. Vacuum sintering 20
2.2.2.2. HP 20
2.2.2.3. HIP 21
2.2.2.4. Spark plasma sintering (SPS) and high voltage electric discharge (HVDEC) 21
2.2.2.5. Challenges in sintering bulk ZrN 23
2.3. Ternary Metal Nitrides (TMN) 23
2.3.1. Synthesis of TMN thin films..23
2.3.1.1. TiZrN 24
2.3.1.1.1. D.C. unbalanced magnetron sputtering (UBM) 24
2.3.1.1.2. D.C. reactive unbalanced magnetron sputtering 24
2.3.1.1.3. D.C. reactive magnetron co-sputtering 25
2.3.1.1.4. R.F. magnetron sputtering..25
2.3.1.1.5. Plasma beam sputtering 25
2.3.1.1.7. Arc ion-plating 26
2.3.1.2. TiAlN 26
2.3.1.2.1. Physical vapour deposition (PVD)...26
2.3.1.2.2. Cathodic arc PVD 27

2.3.1.2.3. PVCVD 27
2.3.1.2.4. PVD magnetron sputtering 27
2.3.1.2.5. Radio frequency magnetron sputtering PVD 28
2.3.2 Synthesis of bulk TMN 28
2.4. High Entropy Nitrides 29
2.4.1. Synthesis of HEN 31
2.4.1.1. HEN thin film synthesis 32
2.4.1.2. HEN powder synthesis 33
2.4.1.3. Bulk HEN synthesis 34
2.5. Flash sintering (FS) and reactive flash sintering (RFS) 35

Chapter III: Synthesis and flash sintering of zirconium nitride powder 41
3.1. Introduction 41
3.2. Experimental Procedure 43
3.2.1. Raw materials and powder synthesis method 43
3.2.2. Flash sintering of synthesized ZrN powder 45
3.2.3. Materials characterization 46
3.3. Results and discussions 46
3.3.1. Powder synthesis example 46
3.3.2. Influence of processing conditions 48
3.3.2.1. Zr to urea molar ratio 49
3.3.2.2. Heat treatment temperature & time: 50
3.3.2.4. Carrier gas type and flow rate 54
3.3.2.5. Role of urea 55
3.3.3.2. Oxidation resistance 58
3.3.4. Flash sintering of synthesized ZrN powder 59
3.3.5. Properties of flash sintered ZrN 62
3.4. Conclusion 63
3.5. Supplementary 66

Chapter IV: Reactive Flash Sintering of TiZrN and TiAlN Ternary Metal Nitrides 69
4.1. Introduction 69
4.2. Materials and methods 72
4.2.1. Raw materials and mechanical mixing 72
4.2.2. Flash sintering setup 72

4.2.3. Materials characterization..73
4.3. Results and discussion..76
4.3.1. Reactive flash sintering behaviors for TiZrN and TiAlN..76
4.3.2. Phase transformation *during* reactive flash sintering of TiZrN and TiAlN..79
4.3.2.1. Characterization by *ex situ* XRD..79
4.3.2.2. Characterization by *in situ* synchrotron X-ray diffraction..82
4.3.3. Microstructure of TiZrN and TiAlN from reaction flash sintering..95
4.3.4. Properties of reactive flash sintered TiZrN and TiAlN samples..97
4.3.4.1. Oxidation resistance..97
4.3.4.2. Mechanical properties..99
4.4. Conclusions..100
4.5. Supplementary..103

Chapter V: Reactive flash sintering and characterization of bulk high entropy nitrides..111
5.1. Introduction..111
5.2. Experimental Procedure..113
5.2.1. Raw materials and mechanical mixing..113
5.2.2. Reactive flash sintering set-up..114
5.2.3. Materials characterization..114
5.3. Results and discussions:..117
5.3.1. RFS of HENs..117
5.3.2. Solid-solution formation during RFS of HEN..119
5.3.2.1. Characterization by *ex situ* XRD..119
5.3.2.2. Characterization by *in situ* synchrotron XRD..121
5.3.3. Microstructure analysis..124
5.3.4. Oxidation resistance..127
5.3.5. Mechanical properties and behaviors at high pressure..128
5.3.6. DFT calculations..130
5.3.7. Superconductivity..132
5.4. Conclusions..134
5.5. Supplementary..137

Chapter VI. Summary and Future Work..144
6.1. Synthesis and flash sintering of zirconium nitride powder..144
6.2. Reactive Flash Sintering of TiZrN and TiAlN Ternary Metal Nitrides..145

6.3. Reactive flash sintering and characterization of bulk high entropy nitrides............146

REFERENCES 148

VITA 170

LIST OF TABLES

TABLE... PAGE

Table 3. 1. Summary of processing conditions (nitrogen precursor used, precursors molar ratio, synthesis temperature, dwelling time and mixing atmosphere) for ZrN powder synthesis by the modified soft urea method and the phases of the final product. (The samples are arranged first by precursor molar ratio, then heat treatment temperature, then time, and then mixing atmosphere of the precursors. Some other parameters that were varied are listed in the footnotes.) 65

Table 4. 1. Summary of standard RFS experiments including sample ID, the precursors used and their molar ratio, maximum current reached (all with initial 8 V DC), total time, products' final phase(s), relative density (from sample weight and dimension),properties such as oxidation onset temperature, fracture toughness, and Vickers hardness. For comparison purpose, the results for standard flash sintering of binary nitrides of TiN and ZrN, respectively, are also listed. 102

Table 5. 1. Summary of the (reaction) flash sintering experiments in this study. The experimental conditions include precursor and molar ratio, initial DC voltage, maximum current reached, and total time, as well as products' final phase composition and properties 136

Table 5. 2. Literature, computation, and experimental data on mechanical properties of binary and high entropy nitrides. 136

LIST OF FIGURES

FIGURE PAGE

Figure 2. 1. SEM image of the synthesized powder (Sun Y et al., J Alloys Compd . 2009) 8

Figure 2. 2. TEM image showing crystalline ZrN particles along with amorphous carbon in the outer shell (from Naim Katea S, Ceram Int., 2021) 14

Figure 2. 3. Steps for the mechanism of nitriding ZrC to ZrN (from Harrison R, J Eur Ceram Soc. 2015) 17

Figure 2. 4. Dependence of density on sintering temperature in SPS of ZrN (from Chernyavskii AS., Inorg Mater, 2019) 22

Figure 2. 5. SEM image of bulk ZrN consolidated by a) HIP, b) SPS, c) HDVEC and d) conventionally (from Chernyavskii AS., Inorg Mater, 2019) 23

Figure 2. 6. Symmetrical structures of high entropy ceramics (from Oses C, Nat Rev Mater. 2020) 29

Figure 2. 7. Vickers hardness and hardness in HENs compared to other ceramics (From Moskovskikh D, Sci Rep. 2020) 30

Figure 2. 8. Change in hardness as a function of VEC of high entropy nitrides and carbo-nitrides (from Dippo OF, Sci Rep., 2020) 31

Figure 2. 9. Comparison of hardness in HEN coatings (from Novikov V, Metals (Basel)., 2022) 32

Figure 2. 10. Comparison of Flash sintering with previously used sintering techniques (from Cologna M, J Am Ceram Soc., 2011) 36

Figure 2. 11. Sintering strain as a function of temperature and electric field (from Biesuz M, J Eur Ceram Soc., 2019) 37

Figure 2. 12. Typical stages in a flash sintering experiment (from Du Y, J Eur Ceram Soc., 2016) 38

Figure 2. 13. Flash sintered and conventionally sintered 3 mol% yttria added to zirconia compared for grain size based on their fracture surfaces (bottom row) and polished surfaces (top row (from M'Peko J-C, J Am Ceram Soc., 2013)......................................39

Figure 3. 1. Photos of graphite boat and powders (a and b) synthesized from the modified soft urea route using Zr : urea molar ratio of 1:4 with 2 h heat treatment in N_2 at (a) 1400 °C (N11) and at (b) at 1600 °C (N15); (c) Photo of a golden- brown FS pellet..44

Figure 3. 2 (a) XRD for sample N11 synthesized using Zr : urea ratio of 1:4, heat treated at 1400 °C for 2 h in N_2. (b) comparison of (220) and (311) XRD peaks for the as-prepared N11 powder with the expected peak for ZrN and ZrC. The composition is determined by Vegard's law to be $Zr(C_{0.09}N_{0.91})$. m and t are for trace amount of monoclinic and tetragonal ZrO_2 48

Figure 3. 3. XRD patterns of samples synthesized using the modified soft urea route with different Zr : urea molar ratio of 1:1 (N1), 1:2 (N2), 1:4 (N11) and 1:6 (N16). The precursor mixing was in air and the heat treatment was at 1400 °C for 2 h in N_2............50

Figure 3. 4. (a) XRD patterns of samples synthesized using modified soft urea method (Zr : urea molar ratio of 1:4) at different temperatures of 600 (N3), 900 (N4), 1200 (N6), 1300 (N8), 1400 (N11) and 1600°C (N15) for 2 h in N2; (b) comparison of the (200) peak to illustrate the shift to lower angle (increase in lattice parameter), which indicates increase in carbon content or decrease in nitrogen content with temperature....52

Figure 3. 5. XRD patterns for products synthesized at 1300 for 10 min (N7) and 2 h (N8) and at 1400 °C for 0 min (N9) and 10 min (N10)..53

Figure 3. 6. (a) comparison of XRD patterns for samples synthesized using modified urea method (at 1400 °C for 2 h) in N_2 (N11) and Ar (N13), (b) zoomed in (220) peak showing more obvious peak splitting for the sample synthesized in Ar, compared with N2...54

Figure 3. 7. (a-b) SEM images of the ZrN powder synthesized with the modified soft urea route (Zr: urea molar ratio of 1:4, heat treatment at 1400 °C for 2 h in N_2)............56

Figure 3. 8. Figure 8 TEM images (a, b, c) of ZrN powder synthesized by modified soft urea route (Zr: urea molar ratio of 1:4, heat treatment at 1400 °C for 2 h in N_2) showing (a) an agglomerated ZrN particle with non-uniform grain size, (b) separated ZrN nano particles in amorphous carbon, (c) a single ZrN particle with ZrO_2 around it, (d) and (e) are lattice fringe profiles obtained from the region in c. (d) is for the light grey area in the upper left showing lattice plane spacing of 3.0 Å corresponding to the (101) plane of t-ZrO_2 , and (e) is for the lower darker region showing lattice plane spacing of 2.3 Å corresponding to the (002) plane of ZrN...57

Figure 3. 9. TGA and DSC plots in air up to 1400◦C for ZrN powder synthesized with the modified soft urea route (Zr: urea molar ratio of 1:4, heat treatment at 1400 °C for 2 h in N2). 58

Figure 3. 10. Plot of applied voltage and resulting current vs. time (in log scale) for flash sintering of synthesized ZrN powder. 60

Figure 3. 11. (a-b) SEM images of a fractured surface of bulk flash sintered ZrN using powder synthesized from the modified soft urea route (Zr : urea molar ratio of 1:4, heat treatment at 1400 °C for 2 h in N_2). 62

Figure 3. 12. TGA and DSC plots in air up to 1400◦C for bulk ZrN flash sintered from synthesized powder (Zr: urea molar ratio of 1:4, heat treatment at 1400 °C for 2 h in N_2). 62

Figure 4. 1. (a) A photo of the setup including the environmental chamber used for in situ synchrotron XRD study of the reactive flash sintering (RFS) process. Note the sample assembly had been installed, pressure was applied, and the front panel was removed to show the inside of the chamber. (b) A photo showing the reactive flash sintering setup installed on the 16ID-B General Purpose Table located at Sector 16 of the Advanced Photo Source (APS) facility in Argonne National Laboratory (ANL) for the in situ synchrotron RFS study: (1) flash sintering setup, (2) 2D X-ray detector, (3) X-ray focusing setup, (4) power supply used in the RFS experiment, (5) water chiller for the chamber. 76

Figure 4. 2. Plot of applied voltage (dotted line) and resulting current (solid line) vs. time for RFS of the std-TZN sample from TiN and ZrN powder mixture (both conducting, 1: 1 molar ratio). Note the maximum current of 200 A corresponds to a current density of 26.5 A/mm^2. 77

Figure 4. 3. Plot of applied voltage (dotted line) and resulting current (solid line) vs. time for RFS of the std-TAN sample from TiN and AlN powder mixture (TiN conducting, AlN insulating, 1: 1 molar ratio). Note the experiment started in the constant voltage mode and the power supply switched to constant current mode when the current reached the set limit of 200 A (26.5 A/mm^2). 78

Figure 4. 4. XRD patterns of the std-TZN sample (from TiN-ZrN equimolar mixture targeting Ti0.5Zr0.5N) before and after standard RFS. The sample formed a single-phase solid solution with composition of Ti0.57Zr0.43N (as determined by XRD and EDS) after RFS. Impurities such as ZrO_2 and graphite were also present after RFS. The insert is the zoomed-in section showing the (200) diffraction peak. The expected peak positions for pure TiN and ZrN are also marked. 80

Figure 4. 5. XRD patterns of the std-TAN sample (from TiN-AlN equimolar mixture targeting Ti0.5Al0.5N) before and after standard RFS. Note TiN peaks shifted slightly to the left (lower angle) after RFS, while h-AlN seems to have disappeared. Impurities of TiO (likely due to partial oxidation of doped TiN) and $Ti_{0.9}Al_{0.1}C$ (likely due to conversion from nitride to carbide upon extended holding at high temperature) are also present after RFS. 81

Figure 4. 6. Plots of (a) current and total resistance and (b) voltage and power versus time for the in situ TZN sample (from TiN-ZrN equimolar mixture) with the RFS processing monitored in real time by synchrotron at the APS facility in ANL. The voltage was linearly ramped up from 0 V at a rate of 0.1 V/s, while the power spiked up non-linearly from ~40 s, reaching the max power of ~1.3 kW with a max current of ~92 A (52 A/mm^2) at ~140 s, and then stabilized. 84

Figure 4. 7. Plot of (a) current and total resistance, (b) voltage and power versus time for the in situ TAN sample (from TiN-AlN equimolar mixture) with the RFS processing monitored in real time by synchrotron at the APS facility in ANL. The voltage was linearly ramped up from 0 V at a rate of 0.1 V/s, while the power displayed incubation before ~123 s, flash at ~123-124 s. After ~125 s, as the voltage continued to ramp up, current kept increasing but slowly, reaching a max power of ~1.3 kW with current of 91.1 A (~52 A/mm^2) at ~138 s. At 170 s, the electrode fractured, and the current dropped to zero, after which the experiment was stopped. It should be mentioned that the zig-zagged shaped data for resistance in (a) before ~120 s were purely an artefact from the power supply due to limitation with electrical control, while the black dash line is for guidance only, showing the behavior of gradual and then sudden drop in resistance with time. 86

Figure 4. 8. (a and b) 2D X-ray scans of the flash sintering cell assembly loaded with TiN-ZrN equimolar mixture before (a) and after (b) in situ RFS. (c) Selected integrated 1D in situ synchrotron XRD patterns of the TiN-ZrN mixture during RFS. The numbers on the right show time in seconds after the beginning of the experiment. (TiZr)N-1 represents the solid solution formed in Spex milling; (TiZr)N-2 and (TiZr)N-3 correspond to solid solutions formed during the heating stage of the RFS; (TiZr)N-4 corresponds to the final single phase nitride solid solution. (d) Zoomed-in sections for selected patterns at different time showing gradual changes in the (111) peak for TiN, ZrN, and related (Ti, Zr)N solid solutions in the 2θ range of 8.5-10.5 degrees. Note the gradual disappearance of individual TiN and ZrN peaks and the appearance and merging of peaks for (Ti, Zr)N solid solutions. (e) Change in lattice parameter of the parent TiN and ZrN as well as the final single phase (Ti, Zr)N product with time during in situ RFS. 91

Figure 4. 9.(a and b) 2D X-ray scans of flash sintering cell assembly loaded with TiN-AlN equimolar mixture before (a) and after (b) in situ RFS. (c) Selected integrated 1D in situ synchrotron XRD patterns of the TiN-AlN mixture during in situ RFS in the 2θ range of 6.5 and 12.5 degrees. The numbers on the right show time in seconds after the beginning of the experiment. Note the appearance of peaks to the left of TiN from ~125 s, which are attributed to Al doped TiN. (d) Change in unit cell volume of TiN, hAlN, and TiAlN solid solution with time during RFS. 94

Figure 4. 10. (a and b) SEM images for a fractured surface of an std-TZN sample from standard RFS, (c) EDS elemental maps of the sample showing the uniform distribution of Ti, Zr, and N..96

Figure 4. 11. (a-b) SEM images for the fractured surface of an std-TAN sample from standard RFS. (c) EDS elemental maps of the sample showing uniform distribution of Ti and N and the association of Al and O. 97

Figure 4. 12. Comparison of TGA plots for std-TZN and std-TAN samples from standard RFS with flash sintered binary nitrides of TiN and ZrN in air up to 1400◦C......98

Figure 5. 1. Plot of applied voltage (dotted line) and resulting current (solid line) vs. time for reactive flash sintering of HEN with nominal composition of $(Al_{0.17}Nb_{0.17}Ta_{0.17}Ti_{0.32}Zr_{0.17})N$ from non-equimolar binary nitride powder mixture. 118

Figure 5. 2. XRD patterns of the (Al0.17Nb0.17Ta0.17Ti0.32Zr0.17)N sample before and after standard RFS. The sample transformed from a mixture of binary nitrides to a cubic, NaCl structured solid solution with minor impurities after RFS. The insert is the zoomed-in section showing the (111) diffraction peak, and the expected positions for (111) peaks of pure h-AlN, c-NbN, h-TaN, c-TiN and c-ZrN are also marked. 120

Figure 5. 3. Plots of (a) voltage and power versus time and (b) current and total resistance versus time for the in situ RFS of $(Al_{0.17}Nb_{0.17}Ta_{0.17}Ti_{0.32}Zr_{0.17})N$ sample monitored in real time by synchrotron at the APS facility in ANL. The voltage was linearly ramped up from 0 V at a rate of 0.2 V/s up to 14.7 V, while the power spiked up non-linearly from ~55 s, reaching the max power of ~1.3 kW with a max current of ~85 A (48 A/mm^2) at ~80 s, and then stabilized. 122

Figure 5. 4. Selected integrated 1D insitu synchrotron XRD patterns of the $(Al_{0.17}Nb_{0.17}Ta_{0.17}Ti_{0.32}Zr_{0.17})N$ during RFS (note the synchrotron radiation has wavelength of 0.4246 Å). The numbers on the right show time in seconds after the beginning of the experiment. 123

Figure 5. 5. SEM images of a fractured surface of reactive flash sintered (a and b) $(Al_{0.17}Nb_{0.17}Ta_{0.17}Ti_{0.32}Zr_{0.17})N$, (c) $(Al_{0.20}Nb_{0.20}Ta_{0.20}Ti_{0.40})N$ and (d) $(Al_{0.20}Nb_{0.20}Ti_{0.40}Zr_{0.20})N$. 125

Figure 5. 6. EDS area map of reactive flash sintered $(Al_{0.17}Nb_{0.17}Ta_{0.17}Ti_{0.32}Zr_{0.17})N$ showing the uniform distribution of Al, Nb, Ta, Ti, Zr, and N. 126

Figure 5. 7. HAADF STEM images of reactive flash sintered $(Al_{0.17}Nb_{0.17}Ta_{0.17}Ti_{0.32}Zr_{0.17})N$... 126

Figure 5. 8. Comparison of TGA plots for binary nitrides of NbN, TaN, TiN and ZrN versus bulk high entropy nitrides of $(Al_{0.17}Nb_{0.17}Ta_{0.17}Ti_{0.32}Zr_{0.17})N$, $(Al_{0.2}Nb_{0.2}Ta_{0.2}Ti_{0.4})N$, and $(Al_{0.2}Nb_{0.2}Ti_{0.4}Zr_{0.1})N$ for bulk subsequent reactive flash sintering... 128

Figure 5. 9. Selected powder synchrotron (λ=0.424590Å) XRD patterns of $(Al_{0.17}Nb_{0.17}Ta_{0.17}Ti_{0.32}Zr_{0.17})N$ high entropy nitride collected at different pressures in diamond anvil cell.. 130

Figure 5. 10. (a) Temperature dependence of magnetic susceptibility at magnetic field B = 30 Oe for HEN sample, (b) Field-dependent magnetization M(H) at 2 K for HEN sample, the inset shows the enlargement of the lower field data. (c) Temperature dependence of longitudinal resistivity ρ_{xx}, (d) Field-dependent magnetoresistance at 2K.. 133

Chapter I: Introduction

High temperature nitrides are a variety of ceramics, with melting point at or above ~2500 ºC. They include groups IV and V transition metal nitrides. These nitrides are of significant interest because to their outstanding properties. For instance, they have very high Vickers hardness, good thermal conductivity, low electrical resistivity, and outstanding corrosion and abrasion resilience [1–5]. Despite the studies already done on high temperature nitrides, many problems remain unresolved. For example, traditional nitride powder synthesis methods may have severe safety concerns, while the understanding about new method such as the urea method is lacking. On the other hand, high temperature nitrides are still susceptible to oxidization and mechanical failures [6]. Previous studies show that, the control of the composition can influence materials performance [7]. For example, ternary metal nitrides, which has two metals alloyed at the metal site in their crystal structure, display enhanced mechanical and oxidation properties compared to binary systems [8–12].

Apart from ternary nitrides, in the past decade, high-entropy ceramics including high entropy nitrides have drawn significant research interest. They typically have five or more metallic elements randomly occupying the same cation site and one or two nonmetal elements occupying the same anion site. The compositional disorder in the cation sublattice leads to increasing molar configurational entropy and accompanied high-entropy effects such as sluggish diffusion and severe distortion in their lattice, which may lead to enhanced properties.

All of these motivate the current research on high temperature nitrides, from binary and ternary to high entropy systems. The goals are to study the synthesis, processing, and formation mechanism of selected transition metal nitrides and understand the relationships between composition, processing conditions, microstructure, and their properties. Such study would provide better understanding of these important materials, which might lead to future industrial applications in machinery, electronics, and other fields.

This thesis is divided into 7 chapters. Chapter 1 begins with the basic introduction of binary, ternary, and high entropy metal nitrides. Chapter 2 summarizes the literature and identifies the limitations in previous studies on binary transition metal nitrides (e.g., ZrN), ternary nitrides solid solutions/composites (e.g., TiZrN and TiAlN), as well as high entropy nitrides (e.g., (Al,Nb,Ta,Ti,Zr)N). Chapter 3 focuses on the synthesis of ZrN fine powders using the soft urea method. It includes a detailed study of the influence of synthesis parameters on the resulting ZrN powder characteristics. It also demonstrates for the first time, the flash sintering of synthesized ZrN powder into dense ceramic body. It is based on the author's paper Das S, Dubois D, Sozal MSI, Emirov Y, Jafarizadeh B, Wang C, et al. Synthesis and flash sintering of zirconium nitride powder. J Am Ceram Soc. 2022; 105: 3925–3936. https://doi.org/10.1111/jace.18421.

Chapter 4 demonstrates reactive flash sintering of ternary metal nitrides, TiZrN and TiAlN. Their phase transformations are studies using both *ex situ* XRD and advanced *in situ* synchrotron experiment that tracks the structural changes in real time. In addition, the products' microstructure and properties such as oxidation resistance and mechanical properties including hardness and fracture toughness were also characterized (it is based on the author's paper Suprabha Das, Andriy Durygin, Vadym Drozd, Md Shariful Islam Sozal, Zhe Cheng, Reactive flash sintering of TiZrN and TiAlN ternary metal nitrides, Journal of the European Ceramic Society, Volume 44, Issue 4, 2024, Pages 2037-2051, ISSN 0955-2219, https://doi.org/10.1016/j.jeurceramsoc.2023.11.079.)

Chapter 5 delves into the synthesis of novel *bulk* high entropy nitride solid solutions such as $(Al_{0.17}Nb_{0.17}Ta_{0.17}Ti_{0.32}Zr_{0.17})N$, $(Al_{0.20}Nb_{0.20}Ta_{0.20}Ti_{0.40})N$ and $(Al_{0.20}Nb_{0.20}Ti_{0.40}Zr_{0.20})N$ by reactive flash sintering. Apart from detailed study of phase evolution using both *ex situ* and *in situ* synchrotron techniques, the microstructure of these HENs were characterized at both micro-scale and atomic-scale analysis. In addition, a broad range of properties from oxidation resistance and mechanical properties (e.g., hardness and fracture toughness) to high pressure response and super conductivity were reported. Finally, chapter 6 summarizes each of the three studies in this dissertation and points out the directions for future research in related fields.

Chapter II: Literature review

2.1. High temperature nitride ceramics

High-temperature nitride ceramics (HTNs) constitute covalently bonded nitrides of transition metals from Groups IV and V, including Ta, Ti, Zr, Hf, and Nb. Possessing elevated melting points, HTNs exhibit a compelling amalgamation of metal-like traits such as high thermal conductivity, and ceramic-like characteristics like substantial hardness and modulus. This unique combination enables them to endure extreme conditions where conventional structural materials falter. HTNs demonstrate chemical stability in high temperatures (surpassing 2000 ℃) and in reactive atmospheres, including environments with atomic oxygen. They exhibit resistance to oxidation ablation at elevated temperatures and maintain structural integrity in oxidizing environments exceeding 1800 ℃, along with exceptional mechanical properties.

These exceptional physical and chemical attributes position HTNs as promising candidates for a new era of high-temperature applications. With potential applications in rockets and hypersonic vehicles, HTNs find utility in critical components such as nozzles, engines, hypersonic vehicles, cutting tools, furnace elements, and high-temperature shielding.

2.2 Binary nitride, ZrN

In the high temperature nitrides, zirconium nitride (ZrN) stands out as an interesting material with a myriad of unique characteristics that render it promising for a diverse range of applications. ZrN is a refractory ceramic characterized by its golden hue. Possessing a fcc crystal structure, it showcases covalent bonding attributed to interaction with zirconium

(Zr) in its 4d state and nitrogen (N) in its 2p state. This interaction gives rise to Zr–N and Zr–Zr bonds only, without the formation of N–N bonds. Non-stoichiometric ZrN is represented by ZrN_{1-x}.

Zirconium nitride, renowned for its exceptional electrical conductivity, high melting point, thermal stability, and hardness. Because of its exceptional resistance to wear and corrosion as a refractory ceramic, it is a desirable option for a variety of industrial applications, including protective layers, coatings, and cutting tools. ZrN's fascinating electronic qualities and compatibility with semiconductor processes provide opportunities for its incorporation into electronic devices and new technologies.

The synthesis process plays a pivotal role in determining the products' composition and properties. Therefore, understanding the synthesis methodologies of zirconium nitride, exploring both conventional and new techniques, as well as tailoring its processing parameters to affect its composition is of vast interest in the scientific community. Hence, a comprehensive understanding of these methods is essential for harnessing ZrN's vast applications. Moreover, a thorough investigation into the fundamental properties of zirconium nitride, including its mechanical, and oxidation characteristics, provides the foundation for its application in diverse fields. Therefore, the first part of this literature review is a comprehensive exploration of synthesis techniques of zirconium nitride.

2.2.1. Synthesis of ZrN powder

Zirconium nitride (ZrN) has been produced through various physical and chemical procedures. Nonetheless, methods such as plasma vapor deposition (PVD) or laser deposition processes, predominantly serve for coating applications. Ensuring the ZrN powders maintain a composition closely aligned with stoichiometry, devoid of impurities from oxide phases and traces of precursors, is crucial. This section focuses on the various chemical methods employed for the synthesis of powder ZrN, exploring both traditional and innovative approaches and the challenges faced.

2.2.1.1. Hydrogenation–nitridation of metal powders

One of the conceptually simplest methods for synthesizing zirconium nitride powders involve the process of nitration of zirconium hydrides or metallic Zr powders. Pukari et al. synthesized ZrN by heating Zr metal chips and ingots to a temperature of 733 K. The hydrogenation process took place over 24 hours in a mixed gas flow of high purity H_2 and Ar. The obtained $ZrH_{1.92}$ underwent nitridation at 1300 °C in purified nitrogen gas for 5 hours [13]. The corresponding reactions are given below:

$Zr+H_2 \rightarrow ZrH$

$ZrH+N_2 \rightarrow ZrN+H_2$

This technique synthesizes ZrN with composition $Zr(N_{0.99}O_{0.01})_{0.97}$ (0.11 wt.% O and 0.01 wt.% C).

Fokin et al. synthesized ZrN by the reactions of powder or bulk Zr with ammonia [14]. The metal interacted with ammonia and hydro-nitridated while using NH_4Cl as an activating agent. Ammonium chloride was removed by dissolving the product in pure ethanol for 1 h at room temperature.

Konuma et al. used high purity N_2 and H_2 gas as plasma gases and radio frequency power was applied [15]. With the increase in power the temperature of the specimen rose to 900 - 950 ˚C in the N_2-H_2 plasma. After nitriding for 49 h, ZrN powder was synthesized with impurities of α-Zr.

These aforementioned methods require high-purity nitrogen, hydrogen, or ammonia (irritant and harmful) gases or produce hazardous reagents like azides, hydrides etc. and need prolonged period of 20–50 h. Moreover, micron-sized Zirconium (Zr) powder can readily undergo ignition and combustion in the presence of air, especially when activating agents (such as NH_4Cl) are mixed with the starting Zr metal powder. Consequently, handling fine powders necessitates specialized equipment, like glove box and an inert atmosphere. As a result of these limitations, the need for a simpler and more cost-effective technique to be adopted.

2.2.1.2. Mechanochemical synthesis

Literature documents that the direct reaction of Zr with N_2 can be attained at room temperature through ball milling of elemental Zr powder, provided a continuous supply of N_2 is introduced into the ball miller. This milling process initiates a solid-state reaction among distinct species.

Calka, used an custom made ball miller to mill Zr metal [16]. A constant supply of high-purity N_2 was provided during the milling. After 120 h of ball milling, ZrN was synthesized.

El-Eskandarany et al. employed high-energy reactive ball-milling (RBM) to synthesize equiatomic spherical ZrN powders (grain size diameter < 8 nm) [17]. The process involved milling of elemental Zr powders under N_2 gas at ambient temperature. Initially, the Zr metal powder agglomerates. On further milling intense disintegration is observed, forming smaller particles in ~3-12 h. These disintegrated particles, featuring fresh surfaces, initiated reactions with the N_2 milling atmosphere in the final stage of milling, resulting in the formation of cubic zirconium nitride powder along with unreacted zirconium powder. After milling for 24–48 h, single phase ZrN with a rock salt structure was achieved.

Sun et al. utilized a blend of $ZrCl_4$ and Li_3N powders, subjecting them to high-energy ball milling in an argon atmosphere [18]. The milling process facilitated a mechanochemical reaction between the $ZrCl_4$ and Li_3N precursors, resulting in the production of LiCl and ZrN with a rock salt structure. The authors also concluded from *in-situ* and DSC measurements, as well as thermodynamic and kinetic analyses, that the reaction is self-propagating, and with increase in milling time the ignition temperature decreases. Fig 2.1. shows the SEM of the synthesized powder.

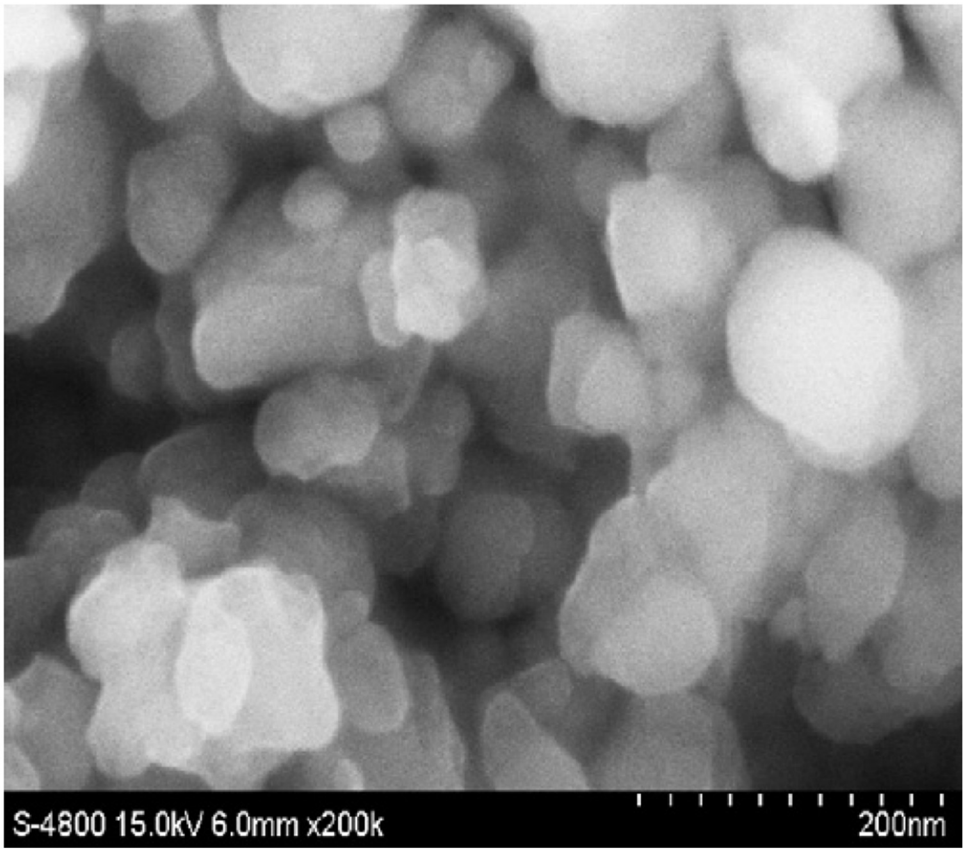

Figure 2. 1. SEM image of the synthesized powder (Sun Y et al., J Alloys Compd. 2009)

Puclin et al. utilized a three step ball milling process [19]. Initially, zircon ($ZrSiO_3$) and aluminum mixtures underwent 120 h of low energy milling in vacuum. No chemical reduction and X-ray amorphous phases were observed. Afterwards the precursors were milled in vacuum at high speed for 120 h, followed by milling under a N_2 atmosphere at a pressure of 100 kPa for 70 hours. Although ZrN was formed, the abrasive nature of zircon led to substantial iron contamination as well as $A1_2O_3$, $ZrSi_2$ and $FeZrSi_2$.

Despite significant efforts in the mechanochemical synthesis of ZrN powder, there are several drawbacks for this route. The synthesis route, which involves diffusion during the milling process, results in prolonged milling times. The final products often exhibit Zr impurities that are challenging to remove. Furthermore, there is a notable presence of iron and oxide contamination in the products, attributed to extended milling using stainless steel tools. The use of nitrogen and/or argon gas for long time increase the complexity and cost.

2.2.1.3. Thermal reduction nitridation using reducing agent

Another method for synthesizing ZrN powder involves the thermal reduction of ZrO_2 using active reducing agent (such as Mg). Wu et al. conducted a reaction by combining ZrO_2, NaN_3, and metallic magnesium within a autoclave made of stainless steel [20]. The container was tightly closed and subjected to heating from room temperature to 1000 ˚C for 8 hours. Subsequently, the setup was allowed to naturally cool, and the resulting product underwent multiple washings with HCl, H_2O, and ethanol to eliminate excess unreacted Mg, followed by a drying process. This method involves a one-step synthetic process without the need for expensive precursors and apparatuses.

Chen et al. synthesized ZrN via similar magnesium thermal reduction nitridation of ZrO_2 as above but in a molten salt ($MgCl_2·6H_2O$ / NaCl eutectic) environment [21]. The mixture was prepared in an alumina mortar, transferred to an alumina crucible, and subjected to heat treatment inside a corundum furnace at 1000°C for 3 hours in a nitrogen atmosphere. The products were washed with hydrochloric acid and water.

Fu et al. first prepare ZrO_2 powder by dissolving used zirconium-oxychloride in distilled water and gradually introduced an ammonia solution. The resulting ZrO_2 precipitate was combined with Mg powder, ground, and then nitrided in a quartz tube furnace in flowing ammonia gas at 1000°C for 6 hours. The nitridation process involved a temperature range of 800° to 1000°C, with varying nitridation times ranging from 2 to 6 hours. The resulting nitridation product underwent washing with HNO_3 and alcohol to eliminate by-products, followed by drying at 85°C for 12 hours to yield nanosized ZrN powder [22].

The synthesis of ZrN via aluminothermic reduction nitridation of zirconium oxide under N2 gas flow is another approach, as shown by Yin et al [23]. Al metal is the reducing agent while $CaCaO_3$ was used as an activating agent and the corresponding reaction is given below:

$6ZrO_2 + 8Al + 2CaCO_3 + 3N_2 \rightarrow 6ZrN + 2CaAl_4O_7 + 2CO_2$ (g)

The powder mixtures underwent ball milling, followed by drying in a rotary evaporator. Subsequently, the dried mixtures were inserted in a BN crucible and ignited in a graphite gas furnace under pure N_2 gas. Nitridation occurred at 1400°C for 6 hours. Following the nitridation process, the resultant products were dissolved with HCl acid and subsequently washed using distilled water to acquire the final material.

Tan et al. employed a sol-gel technique to prepare ZrO_2 powder [24]. Zirconyl nitrate was dissolved in water and ammonium hydroxide, resulting in a sol-gel that underwent centrifugation. After firing at 1000 °C in air for 11 h, the gel converted into zirconium oxide. The ZrO_2 powders were placed into a reactor in a tube furnace with flowing NH_3 (N_2 source) and CH_4 (reducing agent), and the mixture was fired till 1100°C for 3 h.

Despite the efficiency of these process in synthesizing pure ZrN powder, it involved complex and multi-step operating procedures. The need for a reducing agent added complexity, and the removal of byproducts proved time-consuming, requiring multiple solvents and prolonged time.

2.2.1.4. Benzene–thermal method

ZrN powder has also been synthesized by Gu et al. using benzene as a solvent [25]. Anhydrous $ZrCl_4$ powder and Li_3N and benzene were used a precursor. The mixture was added in a stainless steel autoclave and was closed in a N_2 filled dry tank. The autoclave underwent heating at 380 – 400 °C for 48 hours in an oven and was subsequently cooled to ambient temperature. The resulting product mixture underwent multiple washings with ethanol, HCl solution, and distilled water to eliminate benzene, $LiCl_4$, and impurities. The product was then vacuum-dried for six hours at 50 °C. ZrN synthesized was slightly N_2 deficient. Also, oxide was observed, and amorphous carbon was present from carbonization of solvent benzene. The need for starting materials with high purity, the potential hazards associated with high pressure autoclave and handling toxic organic solvents, and the low efficiency in production collectively hinder the viability of the above techniques for industrial mass production.

2.2.1.5. Self-propagating high-temperature synthesis, SHS

The process of combustion synthesis, also known as self-propagating high-temperature synthesis, involves the growth of a combustion front inside the reactant to synthesize compounds. The heat generated during the reaction provides the energy needed to propel the combustion.

Wu et al. used commercial powders of Zr, Si_3N_4 or BN powders as raw materials to synthesize ZrN powder using combustion synthesis [26]. The products are formed by these two routes.

$11\ Zr + 2\ Si_3N_4 \rightarrow 8\ ZrN + 3\ ZrSi_2$

$3\ Zr + 2\ BN \rightarrow 2\ ZrN + ZrB_2$

After 1 h of ball milling, the reactants were dried and then cold-pressed into a cylindrical sample. Combustion was performed in an argon-nitrogen chamber. An electric current was applied to the sample for 2 s and a small (Ti + C) mixture assisted in the reaction.

The formulas show that Zr and Si_3N_4 exclusively generated ZrN and $ZrSi_2$, with no precursors or contaminants. On the other hand, unreacted BN impurities were present in the reaction between the Zr and BN samples. This demonstrates clearly that nitriding Zr using solid Si_3N_4 as the nitrogen source is practical.

Malikova et al. used a mixture of non-pressed powders of Zr, ZrO_2 and Y_2O_3 (as a catalyst), at 500 °C and ignited them in air at a relative humidity of 60%, pressure of 1 atm, and quenched at 30 s after ignition to prevent re-oxidation of ZrN [27]. Air was used as a source of nitrogen gas. However, the product contained Zr, and ZrO_2 impurities. The highest concentration of ZrN obtained is 66 wt. %. Metal carbides and leftover graphite can occasionally contaminate solid combustion products (SCP) when ZrO_2 is reduced by carbon in N_2.

Tsuchida et al. used a similar approach to synthesize ZrN powder [28]. Zr metal and graphite was ball milled for 30 min. The activated sample when exposed in air reacted exothermically instantly. The reaction started emitting a red light and propagated throughout the mixture with a stronger white emission. The setup was immediately protected afterwards to prevent oxidation in air. ZrN was formed along with a trace of zirconium dioxide which could not be prevented by changing carbon content in the precursors.

Zakorzhevskii et al. synthesized ZrN in an SVS-8 laboratory reactor [28]. Zr metal powder was loaded in a crucible and placed into the reactor filled with nitrogen gas and pressurized with N_2 to 50 atm. The combusted product was cleaned and again milled. The product contained ZrN powder with impurities of ZrO_2.

Hector et al. initiated a SHS between lithium nitride and anhydrous $ZrCl_4$ to synthesize ZrN [29]. LiN_3 and anhydrous $ZrCl_4$ were mechanically ground in a nitrogen atmosphere and sealed under vacuum. The crucible was heated at 500°C for 10 mins and cooled to RT. The SHS products were $LiCl_4$ coated ZrN.

Self-propagating reactions are very exothermic and can release large amount of nitrogen gas. An explosion may happen if the reactions are contained in a tiny vial. It is advised that a blast-proof safety screen be used for all reactions. Other than the safety issue the examples above showed that getting pure ZrN is not easy as the products has contaminants in all cases which cannot be easily removed.

2.2.1.6. Direct carbothermic nitridation (CN)

Zhao et al. synthesized zirconium nitride nano powders by the carbothermic nitridation process with starting materials prepared from internal gelation [30]. $ZrO(NO_3)_2 \cdot xH_2O$ and carbon black was the zirconium and carbon source respectively. $ZrO(NO_3)_2 \cdot xH_2O$ was dissolved in deionized water to give ZrO_2 precursor. HMTA and urea was also mixed in deionized water and carbon black was added into it. By an intricate process of hydrolysis and condensation Zr-O-Zr gel network was formed. Carbon particles was added to it and the mixture was dried in flowing N_2 gas. Zirconium nitride nano-powders were successfully prepared by CN reaction of the dried zirconium hydroxide gel with carbon black.

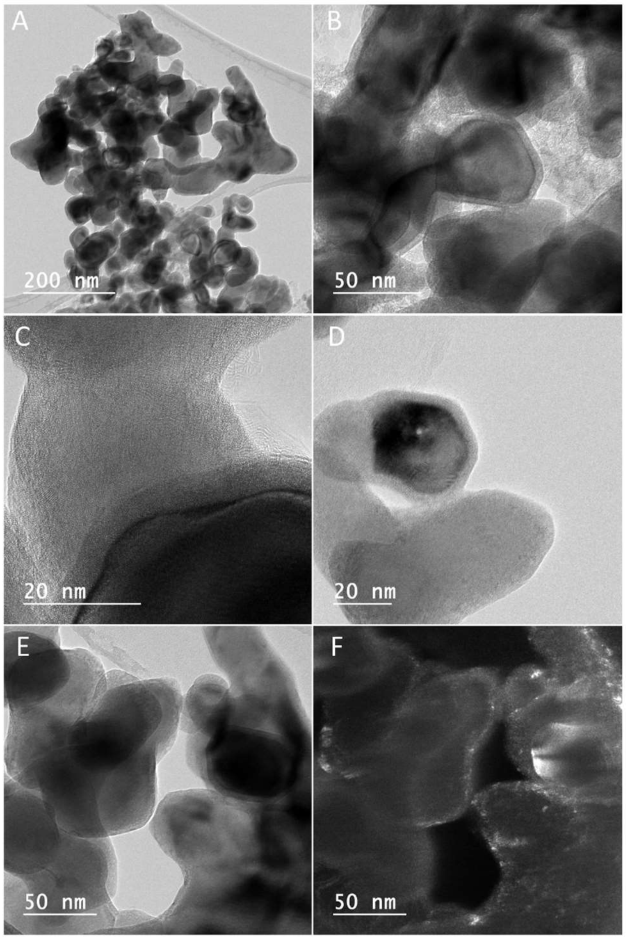

Figure 2. 2. TEM image showing crystalline ZrN particles along with amorphous carbon in the outer shell (from Naim Katea S, Ceram Int., 2021)

Katea et al. synthesized ZrN from mixture with 2–4 nm sized ZrO_2 particles were prepared by hydrolysis of zirconium-(IV)-1-propoxide and sucrose in water and heated to 600 ˚C [31]. A white voluminous gel-like powder precipitate was formed which was sucrose-Zr-gel samples. The precipitate was dried and ground to fine powder. The samples were prepared by pressing the powder into an indium foil, which was connected with an Si-wafer. The samples were heated in a tube furnace at 1500 ◦C under nitrogen gas flow. The products consisted of agglomerated single-crystalline Zr(C,N) particles along with minor amounts of r-$Zr_7O_8N_4$ and m-ZrO_2. The single-crystalline Zr(C,N) particle cores had a 4–6 nm thick distinctive amorphous or nano-crystalline Zr(N,C,O) shell. Fig 2.2 shows the TEM image showing crystalline ZrN particles along with amorphous carbon in the outer shell [31].

Yamamura et al. used zirconia and graphite powder as a starting material [32]. ZrO_2 powder and graphite powder were mixed and pressed into disks and fired in flowing nitrogen gas. The compact transformed first into a nitrogen rich phase, then almost stoichiometric ZrN at 10 h, and finally a carbo-nitride solid solution.

Based on the aforementioned studies, it can be inferred that one of the most popular methods for producing ZrN powders on an industrial scale is carbothermic nitridation of zirconia, which is allow cost reactant. With a high chance of producing zirconium nitride on a large scale, CN techniques are suitable for a wide range of powder sizes and morphologies.

According to literature, for the conversion of oxide to nitride, carbon black must be added and the C/Zr ratio must be carefully regulated. Carbon primarily served as an oxygen getter in the CN process, which produced zirconium oxynitride as an intermediate product, which is then completed by nitrogen replacing its oxygen atoms. Nevertheless, this process still leaves residual carbon powder in the zirconium nitride product, and it is hard to remove.

2.2.1.7. Carbothermal reduction – nitridation methods (CRN)

Another popular method for producing ZrN is carbothermic reduction nitridation of zirconia. It is typically carried out industrially utilizing zirconia as a raw material to cut costs. The CRN process typically contains two-step: ZrO_2 is first reduced by carbothermal means in an Ar atmosphere, and the resulting carbide is subsequently treated in a nitrogen-hydrogen environment to undergo nitridation. Therefore, carbon not only acts as a reducing agent to take away O but also bonds with Zr atoms to form carbide as an intermediate product. The pathway of nitride formation is believed to be as follows:

$ZrO_2(s) + 3C(s) \rightarrow ZrC(s) + 2CO(g)$

$2\ ZrC(s) + 2\ N_2(g) + H_2(g) \rightarrow 2\ ZrN(s) + 2\ HCN(g)$

Harrison et al. synthesized ZrN using carbothermic reduction nitridation [33]. Powders of monoclinic ZrO_2 and carbon black were mixed to achieve a C/Zr molar ratio of 2.7 and homogenized by ball milling a slurry (in acetone) for 12 h using ZrO_2 milling media and dried at 363 K. Powders were then subject to a 24 h dwell at 1873 K under H_2(10%)/N_2 atmosphere in a graphite furnace. The product stoichiometry is $ZrC_{0.3}N_{0.65}$ and ZrC which can be further nitrided. Fig 2.3 shows the mechanism of nitriding ZrC to ZrN [33].

The traditional method of carbothermic reduction and nitridation takes considerable time to finish. To address this, Yugeswaran et al. used transferred arc plasma process to synthesize ZrN from zircon sand via the CRN route [34]. The mixture of zircon–carbon samples were prepared by ball milling with using corundum balls and placed in a graphite anode crucible in a reactor filled with N_2 gas. After cooling, the molten material is like a slag. Although ZrN was formed, m-ZrO_2 impurity lingers even after adding excess C and taking other precautions.

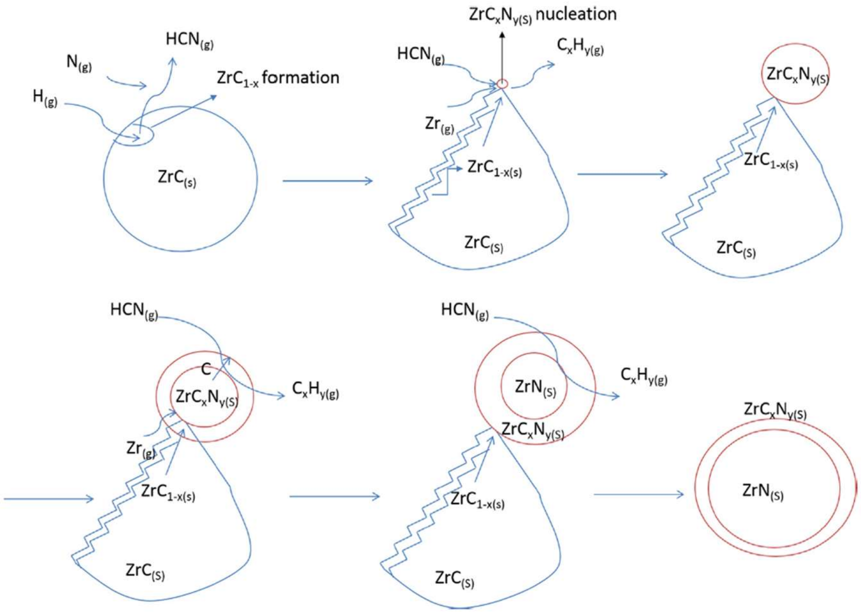

Figure 2. 3. Steps for the mechanism of nitriding ZrC to ZrN (from Harrison R, J Eur Ceram Soc. 2015)

In summary for all CRN processes, carbon is essential to the nitridation processes, but if the ratio is off, the products frequently contain too much carbon or oxides. This makes the process unreliable for mass production.

2.2.1.8. Soft urea and modified soft urea method

Recently, carbothermal reduction method for creating different metal carbides and nitrides in the presence of a N/C source has gained considerable popularity. In particular, the soft urea method (SUM) is an attractive approach due to its simplicity, scalability, and versatility. One interesting feature of "urea technology" is the way urea and a metal precursor combine to generate a gel-like beginning material. This method is ammonia-free, provides an easy way to reduce the amount of hazardous gas/solvents used, and does not require refining.

A sol–gel-based soft-urea route was developed by Antonietti et al., aimed to demonstrate its applicability and versatility in synthesizing crystalline binary transition metal nitrides [35] [36] [37] [38] [39] [40] [41]. They mixed various metal chlorides and/or other salts with ethanol solvent. The metal precursor reacted with the alcohol forming a gel, releasing a significant portion of chlorine as HCl, and forming the corresponding metal precursors. The gels were then placed in an oven and treated under a N_2 flow at 800°C for 7h. It is crucial to note that the heat treatment is a sensitive step in the entire procedure. To prevent excess gel foaming and the explosive discharge of solvent residue, the temperature must be raised gradually. Additionally, the products must be allowed to cool before being exposed to air to prevent oxidation. After processing, the products are stable against oxidative atmospheres.

Yuan et al. synthesized rock salt structured ZrN from $ZrCl_4$, ethanol and urea [42]. At temperatures higher than 200°C, the reductive urea breaks down into ammonia groups, which, upon further heat treatment, ultimately resulting in the synthesis of ZrN. In addition, the urea regulates the particle size. Also, there was no requirement for purifications prior to or following the nitridation process, and no adverse reactions or byproducts were noticed.

Joseph et al. synthesized zirconium oxynitride via this method from $ZrOCl_2.8H_2O$, ethanol, and urea (CH_4N_2O) [43]. Fei et al. synthesized ZrN nano powders from both $ZrCl_4$ and $ZrOCl_2{\cdot}8H_2O$ as Zr source via the soft urea pathway at 1400°C [44].

It is evident from the aforementioned instances that this procedure is rather straightforward because no additional purification is required prior to or during the synthesis. In addition, this procedure does not exhibit any solid precipitations, recrystallization, undesirable reactions, or significant side products. It is possible to maintain very low levels of amorphous carbon, a common byproduct of metal nitride production. It is relatively easy, inexpensive, and quick and is very promising for scaling up to larger applications

Although the soft urea technique demonstrates efficient synthesis of binary transition metal nitride powders, many concerns remain, particularly about the utilization of ethanol as a solvent: It is not involved in the reaction, but its removal (by drying, for example) increases the process cost and complexity and makes waste management more difficult, particularly in large-scale production. In addition, there is still a lack of understanding about the nitride formation process using this route. For example, how various parameters influence the product’s composition and their microstructure is not clear.

2.2.2. Sintering of bulk ZrN

This section focuses on various techniques to sinter bulk ZrN. The sintering temperature, pressure, dwell time, and atmosphere all affect the bulk's relative density and other characteristics. Because of its high melting point, low mutual diffusion, strong covalent bonds, and oxide coating on its surface, ZrN presents significant hurdles when sintering using conventional methods. The nitrogen stoichiometry in ZrN lattice is influenced by the sintering temperature and atmosphere, which need to be controlled well.

The research on ZrN sintering by different techniques—conventional, vacuum, hot pressing (HP), hot isostatic pressing (HIP), spark plasma sintering (SPS), and high voltage electric discharge—is summarized in the sections below.

2.2.2.1. Vacuum sintering

Pshenichnaya et al. used vacuum sintering to synthesize bulk ZrN from milled commercial powders [45, 46]. Vacuum sintering at temperatures between 2000 and 2100°C produced bulk samples with relative densities as high as 95%. Notably, vacuum pressing at lower temperatures resulted in ceramics with higher densities than those in an argon environment. On the other hand, the ceramic with the lowest density was created at 1500°C in a nitrogen atmosphere. Despite this, the ceramic that was vacuum sintered had a grain size of 961 nm, whereas the ceramic that was sintered in a nitrogen atmosphere had the smallest grain size, measuring 641 nm. The nitride content did, however, trend towards the lower bound of its homogeneity range (i.e., ZrN_{1-x}, x ~ 0.10 at 1700°C and ~0.17 at 2100°C).

2.2.2.2. HP

Petrykina et al. performed hot-pressing on $ZrN_{0.95}$ powder under protective Ar temperature at 2500 ◦C for 30 mins and obtained a relative density of ~99% [47].

El-Eskandarany consolidate Zr metal and ZrN mixture without the use of any binding agents [17]. ZrN powder was first cold pressed at ambient temperature in an Ar environment. This was followed by a hot pressing in vacuum at 1.5 GPa pressure at 1600 ◦C for 43 ks.

Lee et al. hot pressed commercial ZrN powder at 1900 ˚C at 60 MPa for 60 mins. The product relative density was 99.42% [48].

Tang et al. had attempted to densify ZrN by adding metallic Zr additive to lower the sintering temperature to 1700 ◦C. [49]. After mixing and drying, the powders were put into a graphite die that had been blasted with boron nitride. The hot pressing with flowing Ar gas contained two stages, first below 1300 ◦C to remove absorbed gases from the powder surface: then at temperature up to 1700 with 30 MPa for densification. It was found though high relative density was obtained; the sintered part has severe nitrogen deficient ($ZrN_{0.83}$). If no Zr metal used, sintering temperature has to be higher at 2000 ºC to obtain similar density.

2.2.2.3. HIP

Alexendra et al. carried out HIP at 1600–1950 °C for 2 h at ~ 190 MPa. The sintered product's relative density was ~ 95.5% [46]. The density of ZrN bulk obtained by Park et al. through HIP of micron-sized powders at ~1400°C was ~83%, while at 1800°C, it was ~ 99% [50]. After a 24-hour HIP process, the grain size is 1 mm.

2.2.2.4. Spark plasma sintering (SPS) and high voltage electric discharge (HVDEC)

SPS and HVDEC are the most popular sintering technology using electrical current. Applying an electrical current and pressure to the samples produces internal heat, which starts the sintering process. High relative density and nanoscale grains are found in the resultant ceramic. This sintering process often takes only a few minutes to finish.

Lee et al. performed both SPS and HVDEC on commercial ZrN powders [51]. For SPS, the maximum density of ~100% were attained at 1700 °C under 120 MPa and the final composition was $ZrN_{0.88}O_{0.10}$. For HVEDC, the maximum relative density was ~93%

at 3 kV and 200 MPa. SPS shows more homogeneous microstructures while, samples consolidated with HVEDC have irregular shaped grains and edges with higher porosity.

Adachi et al. sintered bulk ZrN using SPS at 1873 K for 1 min in N_2 atmosphere [52]. A 91.3% relative density was obtained with a grain size of 10–20 µm. However, the material was nitrogen deficient. In a separate paper, the group again sintered ZrN using SPS at 1773 K, 1873 K and 2073 K resulting in a relative density of 82.2%, 91.3% and 93.4%, respectively [53]. Lee et used commercial ZrN for SPS [48]. The sintering parameter were 1500 °C, 60 MPa for 30 mins. Compared to HP, SPS reduces the time to half and the density was 99.81%.

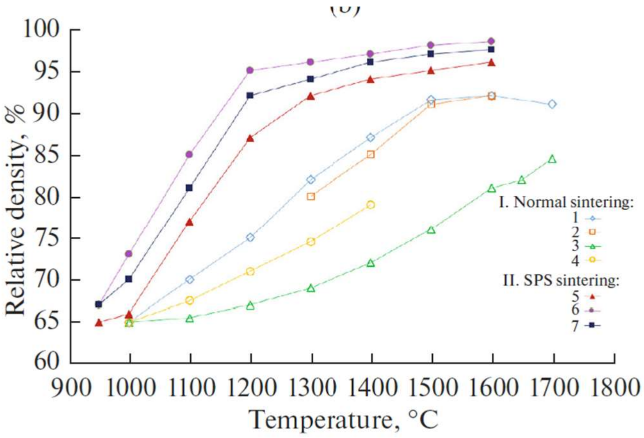

Figure 2. 4. Dependence of density on sintering temperature in SPS of ZrN (from Chernyavskii AS., Inorg Mater, 2019)

Although, HVDEC and SPS share some similarity with hot pressing technologies [48], the capability to accomplish consolidation with lower temperatures, higher heating rates, and shorter times and resulting fine grain size are what make these technologies advantageous [54]. Fig 2.4. shows the dependence of relative density on sintering temperature for SPS of ZrN [55]. Fig 2.5 shows the SEM images of bulk ZrN consolidated by HIP, SPS, HDVEC and conventionally [55].

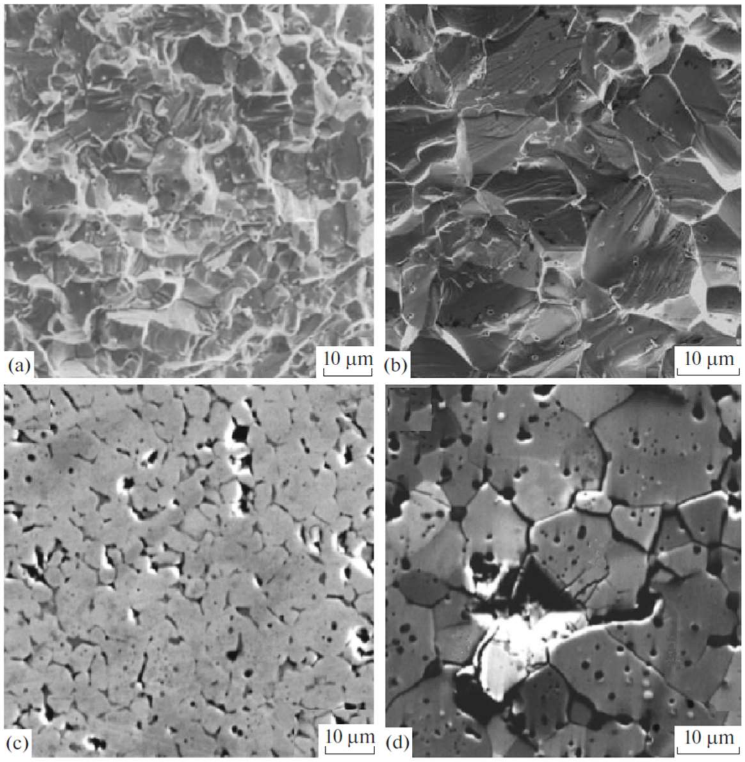

Figure 2. 5. SEM image of bulk ZrN consolidated by a) HIP, b) SPS, c) HDVEC and d) conventionally (from Chernyavskii AS., Inorg Mater, 2019)

2.2.2.5. Challenges in sintering bulk ZrN

Sintering methods like pressure-less sintering and HP require temperature higher than 2000˚C and long dwell times (60 mins and longer). The temperature at which SPS operates can be lower (e.g., ~1600˚C) but the holding period is still about half an hour. Long sintering time leads to grain growth.

2.3. Ternary Metal Nitrides (TMN)

2.3.1. Synthesis of TMN thin films

The majority of research done on TMNs, for example, $Ti_{1-x}Zr_xN$ and $Ti_{1-x}Al_xN$, have been focused on thin films. The section below summarizes some the earlier studies.

2.3.1.1. TiZrN

2.3.1.1.1. D.C. unbalanced magnetron sputtering (UBM)

Lin et al. synthesized TiZrN thin films on Silicon (001) substrates via unbalanced magnetron sputtering [56]. The current was set to 0.24 A and high-purity argon and nitrogen gas was utilized. The negative bias voltage was set at -80V and the operating temperature was 400°C. The resulting coating thickness was 240-690 nm.

UBM sputtering techniques can deposit very high quality thin films and is cost efficient. However, if the nitrogen supply is low, binary nitride peaks of TiN and ZrN are observed in the XRD of the deposited thin films. Also, impurities of TiNO, TiO_2, ZrNO, and ZrO_2 are observed on high N_2 flow while Ti and Zr impurities are observed at insufficient N_2 gas flow.

2.3.1.1.2. D.C. reactive unbalanced magnetron sputtering

In a separate publication, Lin et al. used reactive D.C. unbalanced magnetron sputtering to deposit TiZrN thin films on AISI D2 steel [57]. High purity Ti and Zr metal was used as sputtering sources. Before deposition, the chamber pressure was 6.7×10^{-4} Pa, the temperature was maintained at 450 ˚C, and the substrate was pre-sputtered with high-purity Ar gas. During deposition, high-purity argon and nitrogen gas flow was maintained, and the chamber pressure was $\sim 2 \times 10^{-3}$ Torr. The coating was performed at 450 ˚C with a negative bias of 70 V for the substrates. The nitride coating was sputtered for a duration of 40 to 240 min. TiZrN thin films had a thickness of 3 μm and a Ti inter-layer of 250 nm was observed. The coatings were brittle with low wear resistance.

2.3.1.1.3. D.C. reactive magnetron co-sputtering

Chinsakolthanakorn et al. deposited TiZrN coatings at room temperature on Si wafers with no biasing via reactive DC Magnetron co-sputtering technique using Ti and Zr co-sputtered targets [58]. The pressure during sputtering was 5.0 x 10^{-3} mbar with constant argon and nitrogen gas flow. The focus of this research was understanding the effect of sputtering current on crystal structure and microstructure. As the current was increased the microstructure changed from a dense one to highly porous with large variation of Ti, Zr and N concentration.

2.3.1.1.4. R.F. magnetron sputtering

Lin et al. used R.F. magnetron sputtering for depositing TiZrN coatings on p-type Si wafers from a Ti-Zr alloy target [59]. The sputtering was performed at 400°C, 6.7×10^{-1} Pa. High-purity Ar gas and reactive N_2 gas was maintained throughout the sputtering and the substrate bias was -60V. The thickness of nano-grain thin film was ~147-403 nm after a deposition of 2 h.

2.3.1.1.5. Plasma beam sputtering

Milosev et al. deposited TiZrN thin films on CK 45 steel by the plasma beam sputtering technique [60]. The deposition was performed at 200 °C for 200 s. To solve the adhesion issue, an intermediate layer of TiZr was deposited. It was observed that TiZrN thin film oxidation resistance was lower than that of binary nitrides, TiN and ZrN.

2.3.1.1.6. Cathodic arc evaporation

Musil et al. deposited TiZrN thin films using cathodic arc evaporation on steel substrates [61]. Zr and Ti targets were implemented, and the chamber maintained a N_2 pressure of 0.5 Pa. The elemental distribution was homogeneous with increased Zr concentrations.

2.3.1.1.7. Arc ion-plating

Du et al. deposited TiZrN coating using arc ion plating (like vapor phase deposition) on a substrate of Ti alloy [62]. A negative bias of 250 V was applied on the substrate and an Ar-N_2 gas flow was maintained throughout the 1 h processing. Arc current at Ti and Zr targets were 80 and 90 A respectively. XRD showed that individual Ti, Zr and N peaks were present along with TiZrN peaks. Also, slight oxygen content was observed which might be due to contamination during deposition. Excess N was observed along the grain boundary.

2.3.1.2. TiAlN

2.3.1.2.1. Physical vapour deposition (PVD)

Jang et al. deposited TiAlN coatings on Ti dental implant by PVD [63]. The coating was deposited at 400 °C for 70 mins under a constant N_2 partial pressure (0.05 Pa). Prengel et al. deposited TiAlN coatings on a carbide and cermet cutting tools using PVD [64]. The deposit had a dense microstructure compared to conventional sputtering and a hardness of ~21-24 GPa. Zhang et al. also deposited TiAlN using PVD on carbide and cermet cutting tools [65]. The deposition temperature was ~ 200 °C under a N_2 gas pressure of 1.5 Pa for 100 min. The coating thickness was ~ 3±0.2 µm and the hardness was ~35.4 GPa. By creating a gradient in composition from the outside to the inside, the PVD procedure is used to increase hardness. But this method has drawbacks like surface inhomogeneity and the need for higher temperatures, which negatively affect the substrate's microstructure and friction coefficient.

2.3.1.2.2. Cathodic arc PVD

Another popular approach to deposit TiAlN coatings is by using the cathodic arc PVD. Unlike conventional PVD, in cathodic arc PVD the operation temperature is much lower, and the friction coefficient is improved. Santana et al. deposited TiAlN on WC-Co substrate using TiAl alloy targets in the presence of N_2 gas at 1000 °C [66]. The deposit has a columnar structure, and the hardness is low for the samples due to hex-AlN impurities. For the annealed samples the hardness was even lower as the concentration of hex-AlN increased along with other compositions of non-stochiometric AlN. In addition, milling may also lead to partial oxidation.

Staia et al. deposited a variety of compositions of TiAlN coatings on WC substrates [67]. Staia observed that the hardness and Youngs modulus increases with increasing Al content. However, when 50% Al concentration is reached (i.e., $Ti_{0.5}Al_{0.5}N$), all these properties start deteriorating. Sliding tests at 500 °C indicated that due to the formation of Ti and Al oxide layers during deposition, the coatings friction coefficient increases.

2.3.1.2.3. PVCVD

PVCVD is an alternative where steel tools can be coated at a much lower temperature without the movement of the substrate. Heim et al. employed this method to deposit TiAlN from N_2, H_2, Ar, $TiCl_4$ and $AlCl_3$ (from Al + HCl) [68] in 4 h. A high quality coating was achieved.

2.3.1.2.4. PVD magnetron sputtering

Fernandes et al. deposited $Ti_{40}Al_{60}N$ films on AISI D2 steel using PVD magnetron sputtering [69]. The deposition was performed in a chamber filled with Kr, Ar and N_2 at 480 °C and 600 mPa for 180 mins. The bias was at – 90 V and current was set at 10 A. The reactor containing the setup rotated during the deposition to ensure homogeneity. EDS results showed nitrogen deficiency in the films composition and lower hardness and wear resistance.

2.3.1.2.5. Radio frequency magnetron sputtering PVD

Using RF magnetron sputtering to deposit TiAlN films is a popular technique as it produces a high quality and uniform thin films. Ait-Djafer et al. deposited hard TiAlN coatings using pure Ti and Al sputtering targets in Ar and N_2 plasma atmosphere [70]. The deposition time was 1 h and the film has a thickness of ~ 1µm and a columnar structure. TiN and AlN phases were also observed in the XRD. Hermann et al. also utilized similar techniques to deposit TiAlN thin films [71]. However, the high pressure gases used in this technique leads to porous surfaces due to enhanced nitride formation and lack of deposition. Also, from scratch test it was observed that the hardness and adhesion co-efficient were quite low.

2.3.2 Synthesis of bulk TMN

Despite the progress with thin film technologies, there is a lack of research on synthesis of bulk $Ti_{1-x}Zr_xN$. Not much is known about the relationship between processing parameters and their bulk properties. Borodianska et al. was one of the few researchers to synthesize bulk $Ti_{1-x}Al_xN$ and AlN nanocomposite using SPS from nano-structured $Ti_{1-x}Al_xN$–AlN powder mixture [72]. The precursors were activated in a ball mill filled with nitrogen gas. Finally, SPS was performed at 25 MPa for 600 s at a temperature of 1600 °C. For lower AlN concentration (< =10 wt. %), the hardness is comparable to TiN, while for 40 wt.% AlN, the hardness was lower. It might be due to the presence of unusable AlN from spinodal decomposition at high temperature.

Radune et al. also utilized SPS to synthesize bulk TiAlN [73]. The TiN-AlN powder mixture was ball milled for 100 h, which leads to mechanical alloying and formation of $Ti_{1-x}Al_xN$ solid solution. Then the solid solution powder was sintered using SPS at 1400 °C for 10 min. The process was two-step and very long with iron contamination from extended milling [74].

Despite these studies many things are unknown. For example, is it possible to synthesize/sinter dense bulk TMNs. If and how would the phase transformation occur in bulk TMN ceramics and will it differ from thin films. What is the chemical/physical properties for the bulk TMNs.

2.4. High Entropy Nitrides

The development of high entropy ceramics (HEC) was sparked by the discovery of high-entropy effects in alloys [75–81]. HECs typically have four or more metallic elements randomly occupying the same cation sites and one or two nonmetal elements occupying the same anion sites. High entropy ceramics have broad compositions and diverse structures. Fig 2.6. shows a variety of structures of high entropy ceramics [81] and they now comprise of oxides, borides, carbides, nitrides, sulfides, and silicides [82–86].

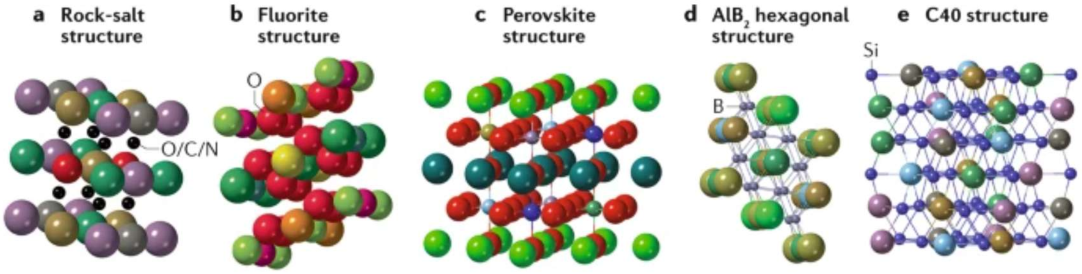

Figure 2. 6. Symmetrical structures of high entropy ceramics (from Oses C, Nat Rev Mater. 2020)

High entropy nitrides (HENs) are unique among high entropy ceramics as they offer exciting opportunities to tune mechanical properties beyond those found in traditional bulk ceramics [87]. Nitrides of transition metals have a mixed bond nature, meaning they have metallic, ionic, and partial covalent properties. The fascinating qualities of these materials, such as elevated melting temperature in covalent and ionic compounds and very low electrical and thermal resistivity for metallic compounds, are partly due to this complex bonding [88]. Literature suggests two major factors that influence the HEN properties, especially mechanical properties.

The first factor is valence electron concentration (VEC). Specifically, the bonding character can be changed by adjusting the HEN composition (metal content), which controls VEC, that in turn influences mechanical properties. As nitrogen gives HENs higher VECs than their carbide counterparts due to the extra valence electron in nitrogen, literature show cubic nitrides with higher VEC give higher toughness than other high entropy ceramics such as carbides [89, 90]. However, there seems to be some discrepancies in terms of the influence on hardness. For example, Fig 2.7. shows the enhanced Vickers hardness as well as fracture toughness in HENs compared to other ceramics [91]. On the other hand, Fig 2.8. shows lower hardness for high entropy nitrides than carbo-nitrides [92].

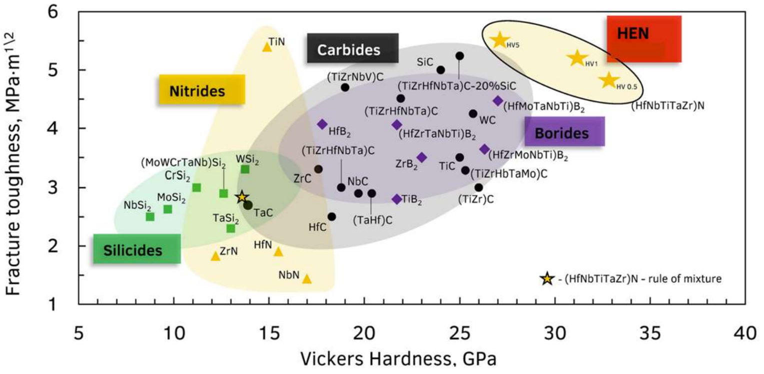

Figure 2. 7. Vickers hardness and hardness in HENs compared to other ceramics (From Moskovskikh D, Sci Rep. 2020)

The second factor is configurational entropy. Some literature suggest that high-entropy nitrides are consistently harder than their ROM values. This is attributed to entropic strengthening, a phenomenon resulting from enhanced compositional randomness and higher configurational entropy [93]. The non-uniform lattice structure hinders dislocation motion and hence increases hardness.

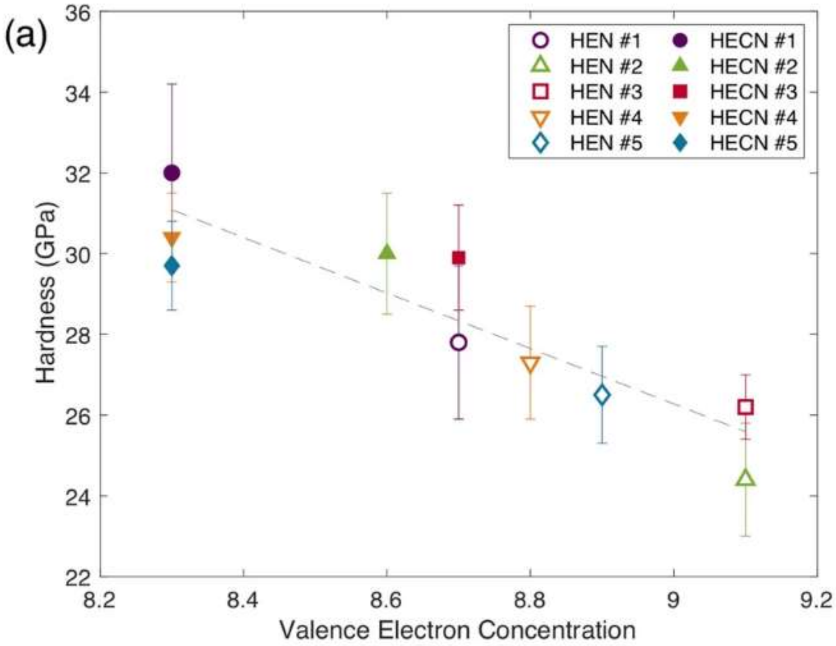

Figure 2. 8. Change in hardness as a function of VEC of high entropy nitrides and carbo-nitrides (from Dippo OF, Sci Rep., 2020)

2.4.1. Synthesis of HEN

High entropy nitrides have been widely synthesized as thin films. There are limited studies on powder and even fewer on bulk. The next section highlights some of these studies.

2.4.1.1. HEN thin film synthesis

Thin films and coatings play a crucial role in enhancing the performance and durability of various materials by providing a protective layer against wear, corrosion, and other environmental factors. HEN thin films have shown comparable hardness to multilayer nitrides as shown in Fig 2.9. [94].

Plasma vapor deposition, vacuum arc deposition and magnetron sputtering are some of the common techniques used to deposit HEN coatings [95–98]. Multicomponent targets are used in an argon and nitrogen gas atmosphere. Transition metals have high tendency to bond with nitrogen and are an ideal choice for targets [99–101]. And they form stable single phase nitride solid solutions with cubic crystal structures and have high hardness.

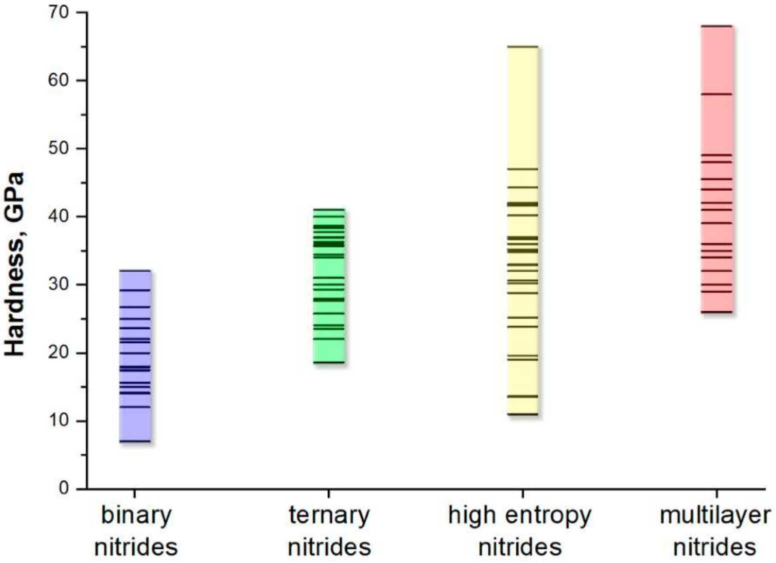

Figure 2. 9. Comparison of hardness in HEN coatings (from Novikov V, Metals (Basel)., 2022)

The hardness and grain structure of the HEN thin film is strongly dependent on the technique used for deposition. Vacuum arc deposition reports some of the highest values

[99, 102]. Li et al. synthesized hard and tough $(NbTaMoW)N_x$ thin films by reactive magnetron sputtering at 575 K in argon - nitrogen atmosphere. These thin films show bcc structure (more like metal) at lower nitrogen concentration and convert to fcc structured solid solution at higher nitrogen concentration. The coatings show excellent hardness, fracture toughness and wear resistance due to the antisite defect of the transition metal on the nitrogen sub-lattice and solid solution strengthening [96]. Another researcher synthesized hard $(MoSiTiVZr)N_x$ HEN coatings also using reactive magnetron sputtering with a deposit time of 150 mins [96]. Here the thin film crystal structure is initially amorphous due to rapid quenching. Later with increase in nitrogen content the solid solution with fcc crystal structure is formed. Shen et al. deposited $(Al_{0.34}Cr_{0.22}Nb_{0.11}Si_{0.11}Ti_{0.22})_{50}N_{50}$ HEN coating by reactive magnetron sputtering [103]. After 50 h annealing at 900˚C, 290 nm thick oxide layer was formed, and the weight gain was much lower compared to binary nitride coatings due to the dense Al_2O_3 layer and Si-rich amorphous network.

Although a lot of these coatings are classified as single phase in the literature, they often have significant residual binary nitride phases [99, 102, 104, 105].

2.4.1.2. HEN powder synthesis

Various techniques have also been adopted to synthesize single-phase solid solution HENs powders, including the modified mechanochemical synthesis [24] (2018), milling and combustion synthesis [91] (2020), soft urea method [106] (2022), and ammonia nitridation [107] (2023). HEN $(Hf_{0.2}Ta_{0.2}Zr_{0.2}Nb_{0.2}V_{0.2})N$ has been successfully synthesized from urea and metal chlorides by the modified soft urea method [106]. Similarly, (VCrNbMoZr)N was synthesized by first mixing the metal chlorides with urea and then ball milling for 30 min followed by pyrolysis at 800 °C in an N_2 atmosphere [24]. Another HEN composition,

$(Co_{0.2}Cr_{0.2}Fe_{0.2}Mn_{0.2}Ni_{0.2})N_{0.956}$ was synthesized by first using a surfactant-assisted hydrothermal method to obtain a high entropy oxide and then nitridation in ammonia atmosphere [107]. Similarly, (HfTaTiNbZr)N was synthesized through initial low-speed milling of metal powders, followed by nitrogen injection to the system and combustion synthesis.

2.4.1.3. Bulk HEN synthesis

Research on the synthesis of bulk high-entropy nitrides (HEN) is a rapidly developing topic with a small but promising group of publications. Recent studies investigating the synthesis of bulk HEN with an emphasis on new compositions have revealed a range of distinct and improved characteristics in the bulk material.

Jin et al. was one of the first researchers to obtain bulk HEN, $V_{0.2}Cr_{0.2}Nb_{0.2}Mo_{0.2}Zr_{0.2}N_{1-x}$ in a two-step process. First they synthesized the HEN precursor powder from a mixture of metal chlorides with urea via the mechanochemical method [108]. The mixture was ball milled for 30 mins and then pyrolyzed in nitrogen atmosphere for 3 h at 800 °C. Finally, the powder was sintered in nitrogen atmosphere. No details of the sintering or the mechanical properties of the newly synthesized bulk material was reported in this study.

Similarly, (HfTaTiNbZr)N was synthesized through a three step synthesis route [109]. First low-speed milling of metal powders was performed to form multi-metal composite powder. This was followed by nitrogen injection to the system to form multiple nitride phases through a combustion reaction. Finally, SPS was conducted in nitrogen atmosphere to convert the powder mixture into bulk HEN. Although the bulk nitride formed was dense, the complete process takes around 13 hours and create oxide impurities. Dippo et al.

synthesized (Hf,Nb,Ta,Ti,Zr)N, (Cr,Nb,Ta,Ti,V)N, (Cr,Hf,Nb,Ta,Ti)N, (Cr,Hf,Nb,Ti,Zr)N and (Cr,Hf,Ta,Ti,Zr)N using high-energy ball milling for three hours, followed by SPS densification for one hour under a pressure of 50 MPa at a temperature of 1600-2200 °C. Carbon impurities were found in large quantities in all the HENs synthesized along with chromium oxide phases.

Therefore, all the current work on bulk HENs necessitates long milling time, high processing temperatures, or long dwell times, leading to high energy consumption and impurities. Because of this there is a need for new technology to prepare bulk HEN with reduced time and temperature and minimal impurities. In addition, the bulk properties need to be characterized and compared with binary nitrides.

2.5. Flash sintering (FS) and reactive flash sintering (RFS)

As we have discussed above, sintering is essential to the process of producing dense ceramic from powders. Conventionally, a high-temperature furnace is used, and the green body is sintered at very high temperature for a long time. Other than being an inefficient process, extensive time and temperature leads to large grain size which may compromises some of its mechanical properties [110]. Therefore, a modern approach is needed for sintering with shorter time and at a lower temperature.

For the past few decades, electricity has been incorporated in ceramic manufacturing to quicken the sintering process and reduce the working temperature. These techniques are grouped as field-assisted sintering technologies (FAST). Examples of conventional FAST technique include microwave sintering [111] and SPS [112]. These techniques lower the sintering temperature and time, but the process still takes tens of minutes or even hours.

Recently, flash sintering (FS) has emerged as a new FAST technique for sintering ceramics. As shown in Figure 2.10, this method is much faster, and the sintering temperature is lower. In fact, this method can produce fine microstructures in a matter of seconds [113].

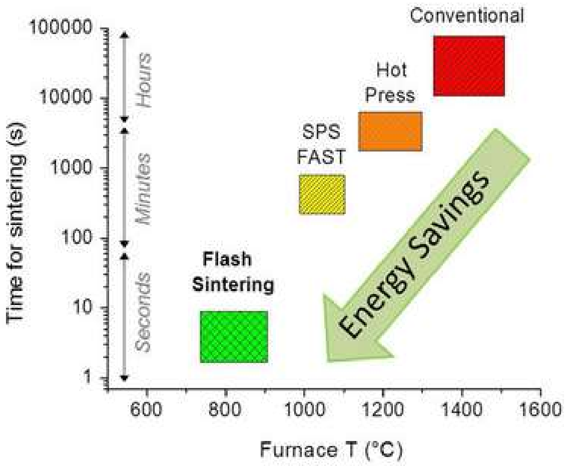

Figure 2. 10. Comparison of Flash sintering with previously used sintering techniques (from Cologna M, J Am Ceram Soc., 2011)

Flash sintering was discovered in 2010 by Cologna et al. and prof. R. Raj [114]. The goal of the original experiment was understanding the effect of current in sintering of zirconia. However, the zirconia was sintered in a matter of seconds when a certain temperature was reached when applying the electric field. Since then, this technique has been implemented to a variety of ceramic materials. Fig 2.11 shows the effect of electric field and temperature on the sintering strain [115].

Flash sintering offers several key benefits, including diminished energy consumption attributed to the lowered sintering temperature and reduced time [116, 117]. The lowered temperature and reduced time also offer the possibility of finer microstructure [118]. It can also sinter material that may decompose in conventional sintering or preserve the meta-stable phase from high temperature [119, 120]. Additionally, the mechanical properties of flash sintered products are comparable to or better than those of conventional ones [121, 122]. Furthermore, FS can consolidate ceramic multilayers or composites [123, 124].

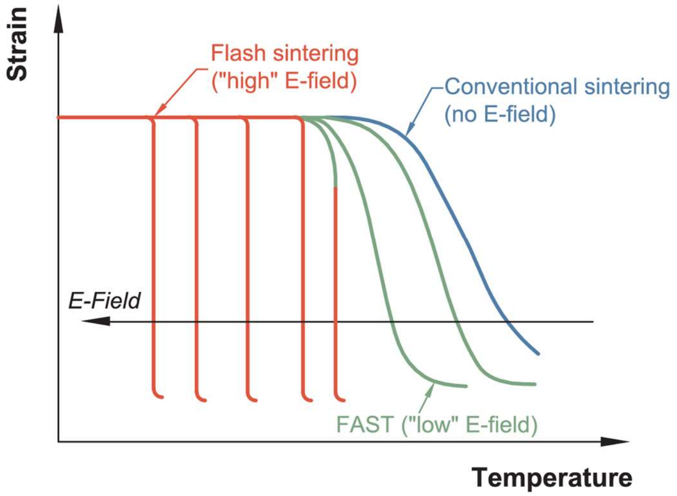

Figure 2. 11. Sintering strain as a function of temperature and electric field (from Biesuz M, J Eur Ceram Soc., 2019)

Typically flash sintering has three stages as illustrated by Figure 2.12 [125]:

a. Stage of incubation: An electric field is introduced, causing conductivity to grow slowly with temperature. The temperature gradually rises with the current density.

b. Flash stage: There is generally a quick thermal runaway brought on by Joule heating caused by dramatic increase in sample effective conductivity [126–128]. These things come together to form the flash event. Finally, the current density reaches the preset maximum, and the power supply switches to current control from voltage control. The green body of the ceramic quickly densifies (often in a few seconds), but the grain growth is very little.

c. Stable stage: The rate of ceramic densification slows down as the current density stabilizes. Grain size, however, keeps increasing steadily until the applied field is turned off.

In order for the flash to initiate the sample must exhibit some conductivity; otherwise, no Joule heating can be generated even with the application of high electric field.

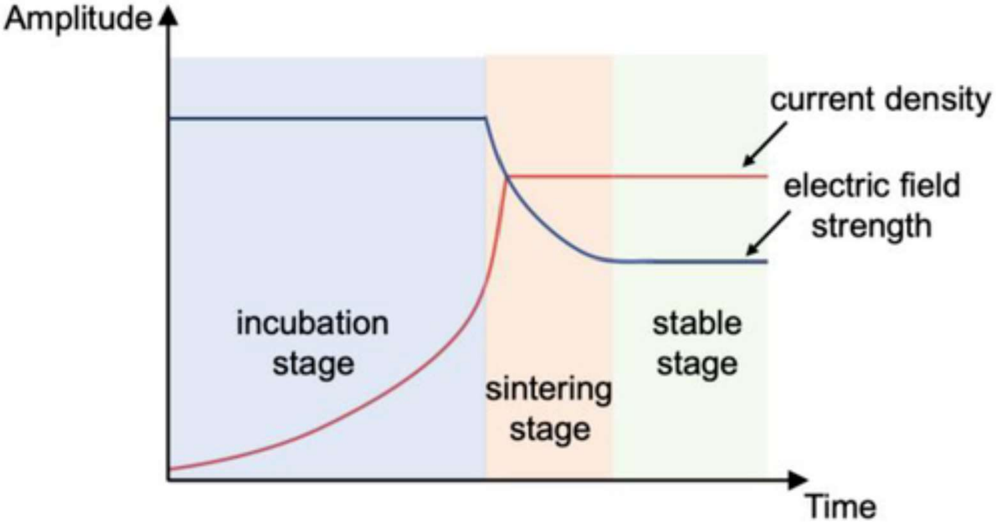

Figure 2. 12. Typical stages in a flash sintering experiment (from Du Y, J Eur Ceram Soc., 2016)

To date, flash sintering has predominantly been applied to oxide ceramics, with a notable focus on zirconia. Specifically, 3 mol% yttria-stabilized zirconia (3Y-TZP) stands out as the most extensively flash-sintered material within the oxide category [114]. A study conducted by Cologna et al in 2010 employed initial electric fields exceeding 40 V cm^{-1}, leading to rapid sintering of 3Y-TZP at 950 °C in dog bone samples within 5 seconds. Fig 2.13 shows that flash sintered can achieve similar relative density and microstructure as for conventionally sintering for 3 mol% yttria stabilized zirconia (3YSZ), but with much shorter time and lower temperature [129].

Within the realm of non-oxides, carbides and borides have the highest number of reported flash sintering publications. Silicon carbide and boron carbide, in particular, have been subjects of FS conducted by numerous research groups [130–133].

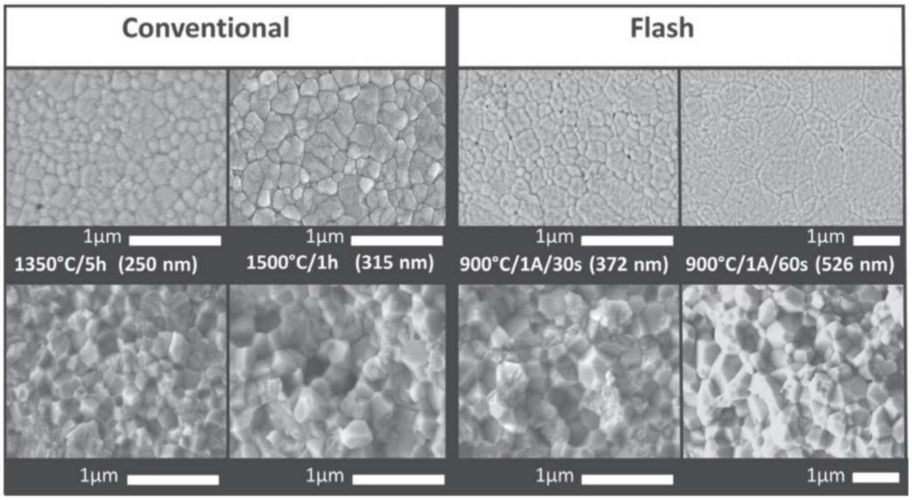

Figure 2. 13. Flash sintered and conventionally sintered 3 mol% yttria added to zirconia compared for grain size based on their fracture surfaces (bottom row) and polished surfaces (top row (from M'Peko J-C, J Am Ceram Soc., 2013)

Advancing beyond binary oxides, carbides, and borides, flash sintering has extended its application to ternary and high entropy compositions. In 2018, a new category for flash experiments involving both sintering and synthesis (reactions) was introduced: "reactive flash sintering" (RFS). This idea came about when dense $BiFeO_3$ ceramics were synthesized from binary oxides [134]. $CaCu_3Ti_4O_{12}$ was subsequently formed by the reactive flash sintering from non-crystalline precursor powder [135]. Similarly, titania-alumina system has also been investigated by flash sintering [136].

Our research group has delved into the investigation of ternary borides $(Hf_{1-x}Zr_x)B_2$ [137, 138]. Additionally, our group has undertaken the flash sintering of $(Nb_{1/3}Ta_{1/3}Ti_{1/3})N_{1-\delta}$ [139].

$Mg_{0.2}Ni_{0.2}Co_{0.2}Cu_{0.2}Zn_{0.2}O$, a single-phase rock-salt entropy-stabilized material, was the first high entropy oxide synthesized by Rost et al [77]. Many more high entropy oxide synthesis have since been reported [140–143]. Notably, flash sintering research of non-oxide high entropy has not yet been conducted.

However, it can be deduced from the aforementioned studies that there is a lack of studies on the flash sintering phenomenon in nitrides across binary, ternary, and high entropy compositions. In particular there has not been studies tracing the phase evolution during reactive flash sintering process.

Chapter III: Synthesis and flash sintering of zirconium nitride powder

The following *chapter* is based on the author's paper Das S, Dubois D, Sozal MSI, Emirov Y, Jafarizadeh B, Wang C, et al. Synthesis and flash sintering of zirconium nitride powder. J Am Ceram Soc. 2022; 105: 3925–3936. https://doi.org/10.1111/jace.18421.

3.1. Introduction

Zirconium nitride (ZrN) is a transition metal nitride of great interest due to its excellent physical and chemical properties. For example, it has a Vickers hardness of 15 GPa [53], a high melting point of 2980 °C [144], good thermal conductivity of 20 W/mK [52], low electrical resistivity of ~25 μΩ·cm [52 145], and excellent resistance to abrasion and corrosion [146]. These make ZrN a good candidate for protective ceramic coating on tools for materials processing [147] and ultra-high temperature refractories [148]. In addition, it is also used as a diffusion barrier material in semi-conductor industry [149 150].

Zirconium nitride has been synthesized by a number of physical and chemical processes. Physical procedures like PVD or plasma and laser deposition processes can produce well-defined and chemically pure materials, but they are primarily limited to coating preparation [35]. On the other hand, chemical approaches can be cost-effective and adaptable for producing a wide range of metal nitrides especially as powders [151]. For example direct nitriding of Zr metal [13], reactive ball-milling [17] , and Li_3N mediated reaction with $ZrCl_4$ [25] have been used for synthesizing ZrN powder. However, some of the precursors used above (Zr metal powder, Li_3N and NH_3) are hazardous or have severe safety concerns [152 153].

Carbothermic nitridation of metal oxide is a relatively safer chemical approach for nitride powder synthesis [30]. It can start from either metal oxide and carbon powder mixture or their precursors, which enable better mixing at molecular scale. For example, Antonietti et al. adopted a soft urea method for the synthesis of various metal nitrides, such as TiN, CrN, VN, NbN, Ta_3N_5, Sn_3N_4, and $Ti_{1-x}Nb_xN$ [35] [36] [37] [38] [39] [40] [41]. Only low-cost starting ingredients such as urea ($CO(NH_2)_2$), metal chlorides, and ethanol are needed, and metal nitride are synthesized after mixing, drying, and heat treatment. However, the alcohol solvent does not participate in the reaction, but its removal (for example, by drying) adds cost and complexity to the process, and complicates waste management, especially for large-scale production.

Once the nitride powder is synthesized, it can be densified into bulk ceramics for different applications. However, due to ZrN's high melting point [144] and the easy formation of an oxide shell (ZrO_2) even at ~600˚C in air [154], obtaining fully dense ZrN bodies is difficult. ZrN has been previously sintered using pressure less sintering [155], hot-pressing(HP) [156], hot isostatic pressing (HIP) [157], spark plasma sintering (SPS) [158], and high voltage electric discharge consolidation [159]. Pressure less sintering and hot pressing require high temperature above 2000˚C and hours of holding time [156] [160]. SPS works at lower temperature ~1700˚C, but the holding time is still ~30 min [159].

Recently, flash sintering (FS) appeared as a unique sintering technique to densify ceramics using electric current. Compared to traditional SPS, flash sintering is even quicker and the current only goes through the sample instead of the graphite die as in SPS. Flash sintering has been used to densify refractory ceramic such as $(Hf_{0.5}Zr_{0.5})B_2$ [137] [139].

The present study aims to demonstrate facile and low-cost synthesis of ZrN fine powders using a modified soft urea route that avoids the use of any solvent. The influence of different processing parameters on product characteristics, such as, stoichiometry is studied. In addition, flash sintering of the synthesized ZrN powder was demonstrated using a homemade setup for the first time. A nearly fully dense sample was obtained from a green pellet under a constant DC electrical field of ~80 V/cm and pressure of ~14 MPa without pre-heating in ~200 secs. The flash sintered sample's composition, microstructure, density, hardness, and oxidation properties were also characterized. Finally, the directions for future research are also pointed out.

3.2. Experimental Procedure

3.2.1. Raw materials and powder synthesis method

As stated, the synthesis of zirconium nitride powder was carried out through a modified soft-urea route. Different from the conventional soft-urea process, no organic solvent (e.g., ethanol) was used. Commercial powder of zirconium (IV) chloride (98%, cont. 1-2% hafnium(IV) chloride, Alfa Aeser#14891) was used as the metal precursor and urea (ultrapure, 99% crystalline, Alfa Aeser #65769) was used as carbon and nitrogen source to synthesize zirconium nitride powder.

$ZrCl_4$ precursor was directly mixed with urea, typically in a 1:4 molar ratio. The mixed powders were then ground (in open air or in an argon glove box) using a mortar and pestle. If the grinding was in air, the mixture released heat and gradually absorb moisture to form a white slurry. Then, the slurry was transferred into a graphite boat with a graphite cap and heat treated in a tube furnace (MHI H18-40HT) at elevated temperature for some time such as 1400°C for 2 h with heating and cooling rate of 3°C/min. An inert (N_2 or Ar, Airgas, UHP Grade) gas flow with a flow rate of 80 cc/min was maintained throughout the heat treatment.

In order to understand the reaction process as well as the advantage and limitation for the modified soft urea method, the processing parameters were varied systematically. For the example of starting recipe, Zr : urea molar ratio of 1:1, 1:2, 1:4 and 1:6 was tried while keeping other parameters (e.g., precursor mixing condition, heat treatment temperature and time) the same. Another example is about the influence of heat treatment temperature; different temperature such as 600, 900, 1200, 1300, 1400 and 1600°C was used while keeping other parameters (e.g., precursor ratio, mixing condition, and heat treatment time) constant. Table 3.1. summarizes the ID and the exact synthesis conditions for various samples in this study. (The samples are listed first by Zr : urea molar ratio, then heat treatment temperature, then holding time, and then mixing atmosphere of the precursors. Some other parameters that were varied are indicated in the footnotes). The ceramic powder, typically golden-brown colored, was collected for further characterization. Figure 3.1. and 3. 1b are example photos of the graphite boat with cap containing the final products synthesized at 1400°C (N11) and 1600°C (N15), respectively.

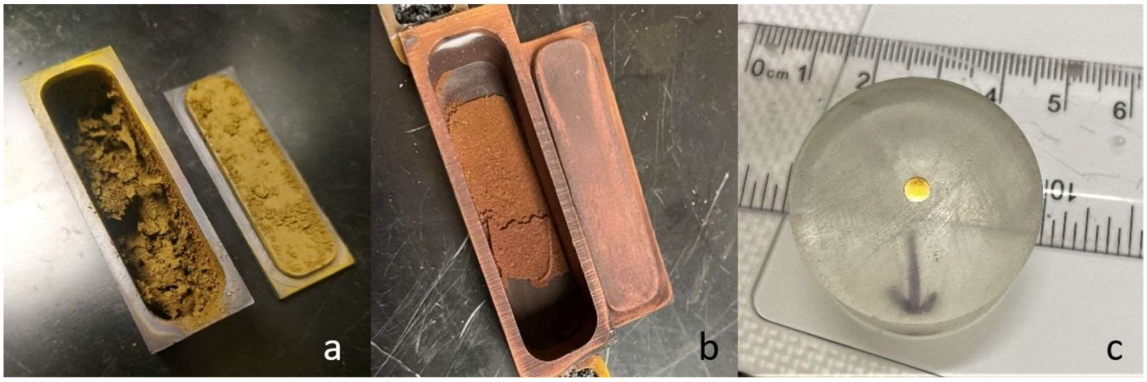

Figure 3. 1. Photos of graphite boat and powders (a and b) synthesized from the modified soft urea route using Zr : urea molar ratio of 1:4 with 2 h heat treatment in N2 at (a) 1400 °C (N11) and at (b) at 1600 °C (N15); (c) Photo of a golden- brown FS pellet.

3.2.2. Flash sintering of synthesized ZrN powder

Flash sintering was performed with the ZrN powder synthesized using the modified soft urea method. A homemade setup was used and has been explained in detail in previous publications [137 139]. The ZrN powder was hand-ground in a mortar pestle for about 10 mins to break down agglomeration. Then around 50 mg of the powder was uniaxially cold pressed (pressure up to ~2400 MPa) to form cylindrical pellets with diameter of 3.1 mm and thickness of ~1 mm. Pressing the powder forms a compact green body and helps the flash sintering process. Finally, the pellet was inserted into a hexagonal boron nitride (h-BN) tube (inner diameter of 3.1 mm, outer diameter of 6 mm and height of 15 mm). Two graphite rods (each with diameter of 3.1 mm and height of 7.5 mm) serve as electrodes to pass the electric current directly through the pellet, which is contained inside the insulating h-BN tube. There are also external structure to provide mechanical support and thermal insulation, as explained in previous publications [137 139]. A constant DC voltage of 8 V (corresponding to a DC electrical field of ~80V/cm for ~1 mm thick green samples) and a constant pressure of 14 MPa were applied between the two graphite electrodes. The flash occurred without external pre-heating. The entire process at constant voltage took 200 secs. Then the power was shut off and the system was allowed to cool down to room temperature. Figure 3.1. c is a photo of a flash sintered pellet embedded in resin after grinding and polishing. As mentioned in previous studies [137 139], some shortcomings of this flash sintering setup are the lack of a protective environment to prevent oxidation of the graphite components, while the temperature measured is much lower than sample actual temperature. This is because the thermocouple inserted in the set-up is not in contact with the sample due to limited melting temperature (~1480°C) of the type R thermocouple. Further improvement will be adopted in future to address these limitations.

3.2.3. Materials characterization

For characterization of synthesized powders and the flash sintered pellet, the X-ray diffraction patterns were collected by a Siemens D5000 diffractometer with Cu-K_{α} radiation (λ=1.541874 Å). The microstructure, particle size, and energy dispersive X-Ray spectroscopy (EDX) for both the sintered powder and flash sintered pellet were analyzed under a scanning electron microscope (SEM JEOL JSM-F100). Thermogravimetric analysis (TGA) and differential scanning calorimetry (DSC) for both the powder and fractured flash sintered pellet from 25°C to 1400°C in air at 10°C/min heating rate were carried out using a SDT Q600. The relative density was calculated from sample weight and dimensions. The sintered pellet was mounted in epoxy, polished, and tested for Vickers hardness using LECO LM810AT (LECO Corporation). The indentation was performed with a diamond tip at a load of 2 N. The test was repeated at 10 different places to ensure accuracy of the result.

3.3. Results and discussions

3.3.1. Powder synthesis example

As stated, Table 3.1 summarizes the different synthesis conditions used (e.g., nitrogen source, mixing atmosphere, metal to urea molar ratio, heat treatment temperature and holding time, carrier gas) and the resulting products' phase information. The target composition for this research was ZrN. Comparing with the conventional soft urea method that involves alcohol solvent, the current work adopted a modification: zirconium chloride precursor was directly mixed with urea without solvent and then the ground mixture (typically a slurry after absorbing moisture from atmosphere) was heat treated in a tube furnace in flowing nitrogen. The simplified chemical reaction, assuming Zr : urea = 1 : 1 by mole, is :

$$2ZrCl_4 + 2\,(NH_2\text{-}CO\text{-}NH_2) \rightarrow 2ZrN + 8HCl + N_2\uparrow + 2CO\uparrow \quad (1)$$

Of course, the actual process will be much more complex involving ZrO_2 formation and subsequent reactions from ZrO_2 to ZrN, as discussed in detail later.

N11 is an optimal example of the synthesized powders in this study. It was started with Zr to urea molar ratio of 1:4, mixed in air, and heat treated at 1400°C for 2 h in N_2. Figure 3. 2a shows its XRD pattern. Sharp and intense diffraction peaks corresponding to single phase ZrN are observed. There is no obvious peak splitting, but there are very minor peaks corresponding to tetragonal and monoclinic ZrO_2. Since ZrN often forms solid solution with ZrC, the (220) and (311) diffraction peaks of the synthesized powder as well as expected XRD peak positions for pure ZrN (PDF Card No.: 04-004-2860, lattice parameter 4.585 Å) and ZrC (PDF Card No.: 04-004-2979, lattice parameter 4.698 Å) are shown in Figure 3. 2b. The obtained XRD peaks are close to the standard pattern for pure ZrN. The lattice parameter obtained from the XRD pattern is 4.594 Å. Based on Vegard's law, the composition is determined to be $Zr(C_{0.09}N_{0.91})$. This is consistent with literature that show carbon is often present as a dopant in the nitrogen sub-lattice for nitrides synthesized using similar methods [30] [24].

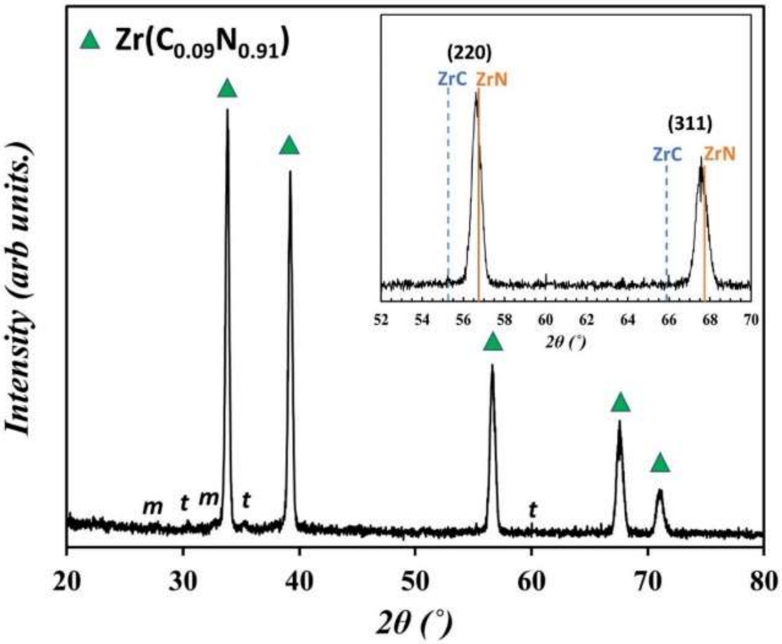

Figure 3. 2 (a) XRD for sample N11 synthesized using Zr : urea ratio of 1:4, heat treated at 1400 °C for 2 h in N_2. (b) comparison of (220) and (311) XRD peaks for the as-prepared N11 powder with the expected peak for ZrN and ZrC. The composition is determined by Vegard's law to be Zr($C_{0.09}N_{0.91}$) . *m* and *t* are for trace amount of monoclinic and tetragonal ZrO_2.

3.3.2. Influence of processing conditions

As explained in section 3.2.1, the powder synthesis was carried out under different conditions to understand the effects of different processing parameters on products characteristics. For example, by keeping other parameters constant, different Zr to urea molar ratio was used to study its effect on product stoichiometry such as the carbon and nitrogen content. It is assumed that urea is the nitrogen and carbon source in this method and varying the Zr to urea molar ratio might change the nitrogen content in the final product. Similarly, for the same precursor molar ratio, heat treatment temperature and time were changed to understand the kinetics of ZrN phase formation. Other synthesis parameters explored include alternative nitrogen precursor (NH_4Cl), precursor mixing atmosphere, and carrier gas type (N_2 vs. Ar) during heat treatment to understand the reaction process. The following section presents detailed study on the effects of various processing parameters and their implications for the reaction mechanism.

3.3.2.1. Zr to urea molar ratio

Figure 3.3 shows XRD patterns of samples synthesized using different Zr : urea molar ratio of 1:1, 1:2, 1:4 and 1:6, all at 1400°C for 2 h. It is worth noting that the Zr : urea molar ratio seems to play a crucial role in ZrN formation. When the ratio is 1:1 (sample N1), the major phase is m-ZrO_2 and the minor phase is t-ZrO_2. When it is increased to 1:2 (sample N_2), the major phases are t-ZrO_2 and $Zr(C_{0.02}N_{0.98})$, while the minor phase is m-$ZrO_{2.}$ At 1:4 molar ratio (N11), as discussed before, $Zr(C_{0.09}N_{0.91})$ was obtained with almost no oxide. When the Zr: urea molar ratio is increased further to 1:6 (sample N16), no oxides were found but the amount of carbon in the product seems to increase, as indicated by the stochiometry of $Zr(C_{0.25}N_{0.75})$. These indicate when the urea content is too low in the starting recipes, there is not enough nitrogen or carbon to avoid oxide formation. On the other hand, when the urea content is too high, oxides are removed, but excess carbon goes into the lattice.

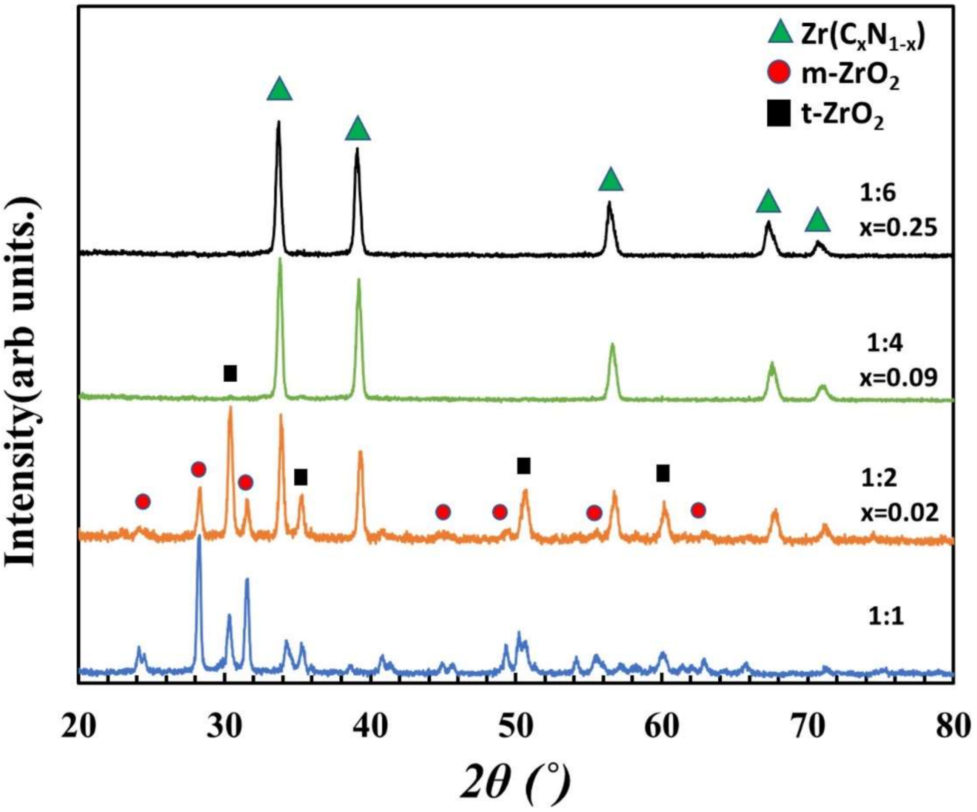

Figure 3. 3. XRD patterns of samples synthesized using the modified soft urea route with different Zr : urea molar ratio of 1:1 (N1), 1:2 (N2), 1:4 (N11) and 1:6 (N16). The precursor mixing was in air and the heat treatment was at 1400 °C for 2 h in N_2.

3.3.2.2. Heat treatment temperature & time:

Figure 3.4a shows the XRD patterns of samples synthesized at different temperatures for 2 h, with the same Zr to urea molar ratio of 1:4. At 600°C (N3), the major phase was t-ZrO_2 with no hint of ZrN formation. At 900°C (N4), the major phase is t-ZrO_2, and the minor phase is m-ZrO_2, while ZrN just started to form. When the temperature was increased to 1200°C (N6), t-ZrO_2 and m-ZrO_2 were still present, but the major phase was ZrN. When the synthesis temperature was further increased to 1300°C (N8) and above (1400°C (N11) and 1600°C (N15)) almost pure ZrN with very little oxide phase was obtained. This indicates that in this synthesis route, the precursor mixture first goes through oxide formation followed by reduction/nitridation to form ZrN. The reduction/nitridation is a thermally activated process and high temperature (above ~1300°C) was needed to remove oxide and complete the nitridation. Supplementary figure S1 shows the calculated reaction free energy change for the reaction

$$2ZrO_2 + 4C + N_2 \rightarrow 2ZrN + 4CO \qquad (2)$$

It shows when the temperature is low (e.g., below ~1200 °C), the free energy change for the reaction from oxide to nitride is positive. When the temperature is high (e.g., 1400 °C or higher) the free energy change becomes negative. The exact equilibrium temperature depends on the atmosphere such as CO partial pressure (pCO).

Figure 3.4b shows the (200) peak for those products synthesized at 1200, 1400 and 1600°C for 2 h. It shows that, as heat treatment temperature increases, the diffraction peak shifts to lower 2θ angle indicating increase in lattice parameter. As mentioned before, ZrN and ZrC form continuous solid solution, while ZrC has a larger lattice parameter than ZrN. Therefore, the observation means, as temperature increases, the product carbon content increase while nitrogen content decrease. Actually, based on Vegard's law , the stoichiometry for the 1200, 1400, and 1600°C was $Zr(C_{0.02}N_{0.98})$, $Zr(C_{0.09}N_{0.91})$, and $Zr(C_{0.27}N_{0.73})$, respectively.

Figure 3.5. shows the XRD patterns for products synthesized at 1300 and 1400°C for different time. When the holding time was only 10 min at 1300°C (N7), apart from ZrN significant amount of ZrO_2 phases were identified. When the dwell time was increased to 2 h (N8), most of the oxides was removed and $Zr(C_{0.10}N_{0.90})$ was obtained. Similarly, at 1400°C with no holding (N9), significant ZrO_2 phases were observed. When the dwell time

increased to 10 min (N10), oxides were largely removed. This is expected because at higher synthesis temperatures, the reaction kinetics are faster, and less dwell time is needed to remove oxides and form nitride.

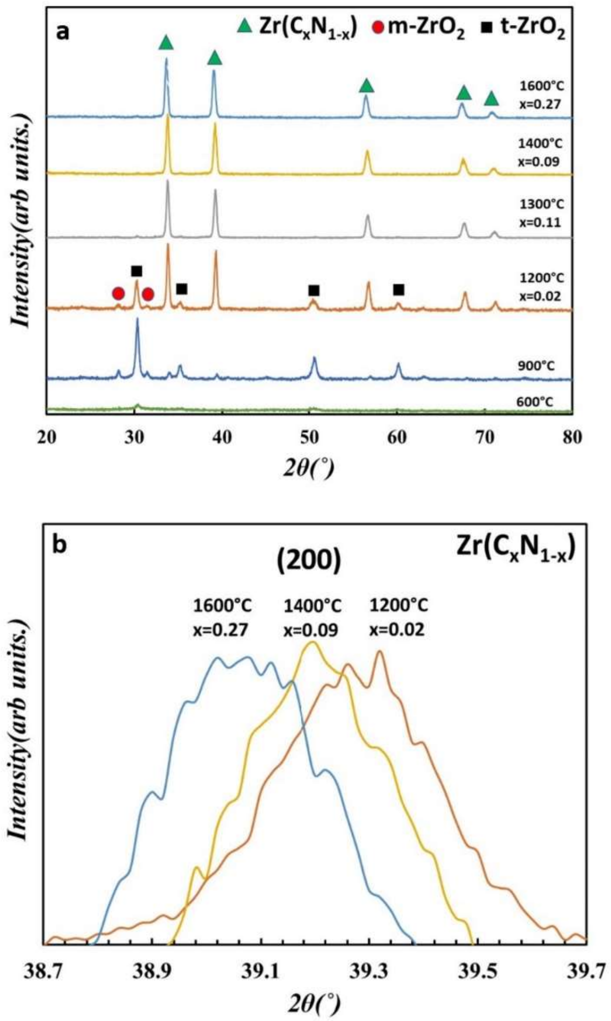

Figure 3. 4. (a) XRD patterns of samples synthesized using modified soft urea method (Zr : urea molar ratio of 1:4) at different temperatures of 600 (N3), 900 (N4), 1200 (N6), 1300 (N8), 1400 (N11) and 1600°C (N15) for 2 h in N_2; (b) comparison of the (200) peak to illustrate the shift to lower angle (increase in lattice parameter), which indicates increase in carbon content or decrease in nitrogen content with temperature.

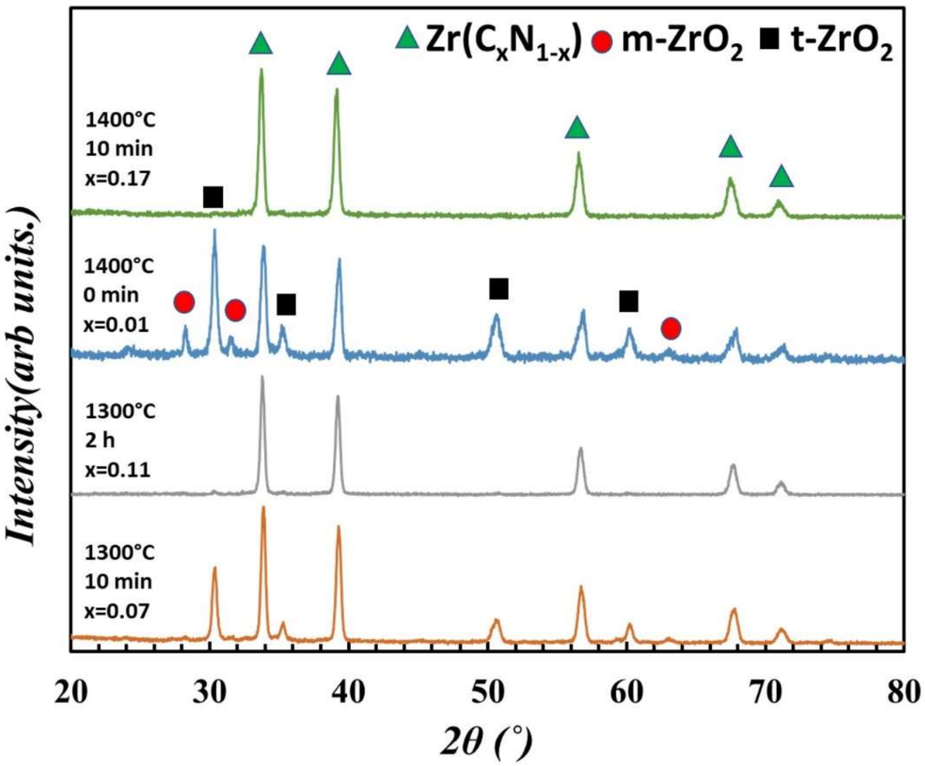

Figure 3. 5. XRD patterns for products synthesized at 1300 for 10 min (N7) and 2 h (N8) and at 1400 °C for 0 min (N9) and 10 min (N10).

3.3.2.3. Precursor mixing atmosphere

To explore if ZrN can be obtained directly instead of first forming ZrO_2 and then convert to nitride, we explored the effect of precursor mixing atmosphere. The hypothesis was, because the precursors were mixed in air, moisture absorbtion leads to the formation of a slurry. As a result, $ZrCl_4$ converts to $ZrOCl_2$ and then to ZrO_2 upon heat treatment. Therefore we explored mixing the precursors in the glove box while keeping other parameters the same. Figure S2a compares the XRD patterns of samples synthesized at 1200 °C for 2 h with glove box mixing to those with air mixing. The hope was glove box mixing would reduce or even avoid oxide formation. However XRD patterns showed that both yield monoclinic and tetragonal oxides, indicating similar reaction paths despite different mixing atmospheres. At 1400°C, nitrides were formed with almost no oxides for both methods, as shown in Figure S2b. This suggests that the oxide formation is not due to mixing in the air but, maybe, the formation of Zr-O bond when $ZrCl_4$ and urea were mixed. It may also be due to inadequate N_2 purity or O_2 leak into the system or preffered association between Zr and oxygen from urea. Further study is needed to clarify this.

3.3.2.4. Carrier gas type and flow rate

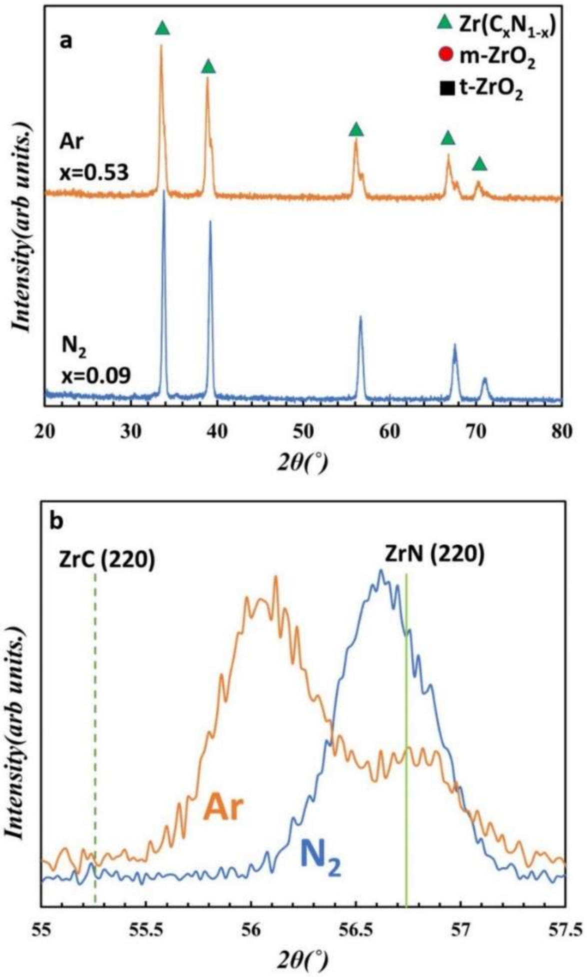

Figure 3. 6. (a) comparison of XRD patterns for samples synthesized using modified urea method (at 1400 °C for 2 h) in N_2 (N11) and Ar (N13), (b) zoomed in (220) peak showing more obvious peak splitting for the sample synthesized in Ar, compared with N_2.

Figure 3.6a shows the XRD patterns of samples synthesized in nitrogen vs. argon as the carrier gas inside the tube furnace. XRD shows that argon atmosphere causes peak splitting unlike nitrogen atmosphere. Focusing on the (220) peak in Figure 3.6b, a single peak centered at 56.62° was obtained for nitrogen. When using argon as the carrier gas, the peak slits in two, with the smaller peak at 56.78° representing ZrN, and the larger peak at 56.04° representing $Zr(C_{0.52}N_{0.48})$. Such an observation indicates that the nitrogen in urea appears not enough to form single-phase nitride. When the atmosphere is low in nitrogen concentration, significant amount of carbon rich nitride was obtained. This proves N_2 gas is necessary along with urea as the nitrogen source to form a single-phase ZrN with low carbon content in the lattice.

3.3.2.5. Role of urea

To understand the role of urea, some additional experiments were carried out. For example, it was hypotheized that a carbon free nitrogen source like NH_4Cl might lead to formation of pure ZrN and avoid carbon dissolution in the nitrogen sub-lattice, as observed when using urea. Figure S3 shows XRD patte rns for samples synthesized using NH_4Cl (Zr:NH_4Cl molar ratio=1:8) in comparision to urea as the nitrogen precursor. The major phases were t-ZrO_2 and m-ZrO_2 and the minor phase was ZrN. Indeed, different molar ratios for $ZrCl_4$:NH_4Cl of 1:4, 1:5 and 1:8 have been used. However as the NH_4Cl content increase, all three products contained major phases of t-ZrO_2 and m-ZrO_2 and the amount of ZrN does not seem to increase significantly. This indicates that NH_4Cl does not appear to be as good a nitrogen source as urea for nitride formation, and carbon seems necessary for the modified soft urea method to obtain high purity ZrN.

3.3.3. Characterization of synthesized powder

3.3.3.1. SEM and TEM

Figure 3.7a and 3.7 b show the SEM image of the ZrN synthesized at 1400°C for 2 h (under condition same to N11, same for discussion below). Most of the particles are aggregated together as a result of high heat treatment temperature. The grain size is mostly sub-micron. EDS shows that the N:Zr atom ratio is 1.01±0.06, which is close to the ratio of ~0.91 determined by the Vegard's' law for this sample. In order to further understand the microstructure of the synthesized ZrN powder, the sample was also analyzed using TEM.

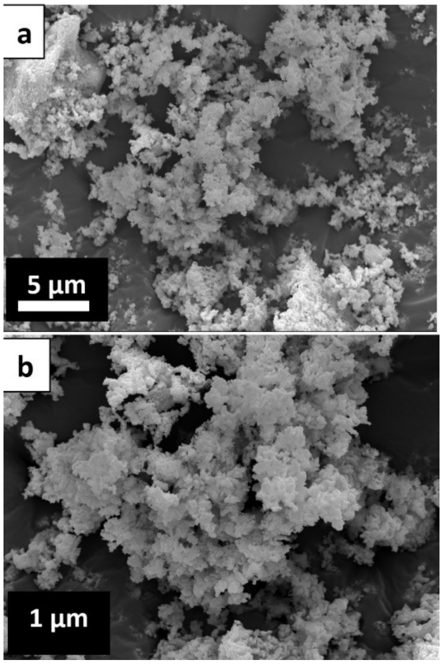

Figure 3. 7. (a-b) SEM images of the ZrN powder synthesized with the modified soft urea route (Zr: urea molar ratio of 1:4, heat treatment at 1400 °C for 2 h in N_2)

Figure 3.8a shows a TEM image of an agglomerated ZrN particle consisting of non-uniform sub-micron to nanosized grains. Figure 3.8b shows that in selected areas the individual ZrN grains appear separated but still highly non-uniform in size. The ZrN particles are embedded in amorphous carbon which is the light grey area in the image. Some particles have a low atomic mass crystalline region around them, which is ZrO_2. In fact, Figure 3.8c shows a ZrN particle with ZrO_2 on the upper left-hand side. Figure 3.8d and 3.8e are lattice fringe profiles of the region, which show that the left lighter area is t-ZrO_2 with lattice plane spacing of 3.0 Å corresponding to its (101) plane, while the darker area is cubic ZrN with lattice plane spacing of 2.3 Å corresponding to the (002) plane.

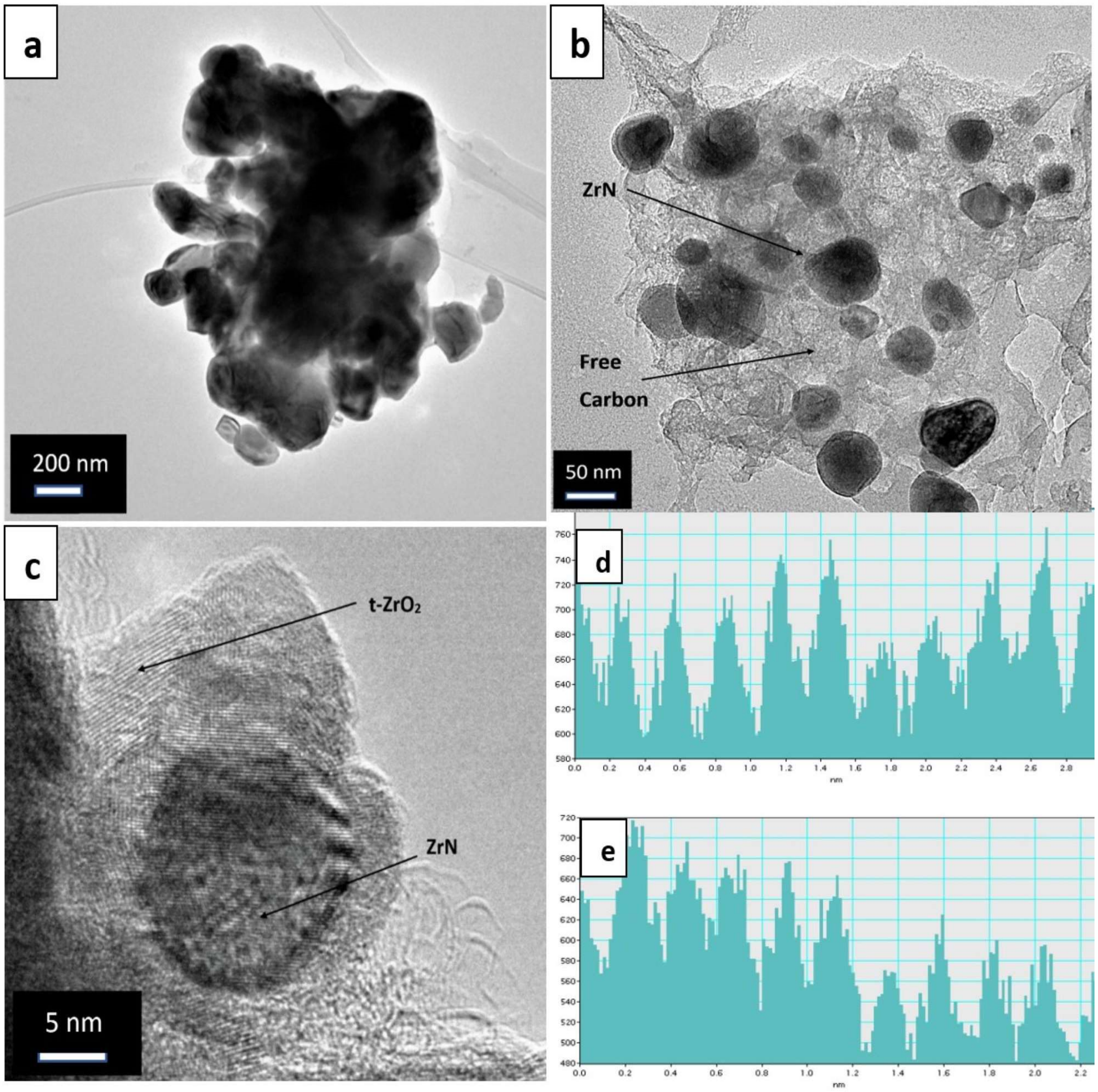

Figure 3. 8. Figure 8 TEM images (a, b, c) of ZrN powder synthesized by modified soft urea route (Zr: urea molar ratio of 1:4, heat treatment at 1400 °C for 2 h in N_2) showing (a) an agglomerated ZrN particle with non-uniform grain size, (b) separated ZrN nano particles in amorphous carbon, (c) a single ZrN particle with ZrO_2 around it, (d) and (e) are lattice fringe profiles obtained from the region in c. (d) is for the light grey area in the upper left showing lattice plane spacing of 3.0 Å corresponding to the (101) plane of t-ZrO_2 , and (e) is for the lower darker region showing lattice plane spacing of 2.3 Å corresponding to the (002) plane of ZrN.

3.3.3.2. Oxidation resistance

Figure 3.9 shows the TGA-DSC plot of ZrN in air up to 1400˚C. No significant weight change was observed till 250˚C. There is a gradual increase in weight from 250˚C to 525˚C. At 525˚C the measured weight gain is around 9%. This weight change corresponds to the exothermic peak at 425˚C. There is a slight weight loss after that, presumably due to the burning of residual carbon in the sample. From 650˚C till 740˚C significant weight gain is observed, and the total weight gain at 740˚C is around 14.5%. This weight change corresponds to the exothermic peak at 625˚C. Higher than 740˚C the weight starts to decrease, which is attributed to release of N_2 and possibly burning of residual carbon. Due to the complexity of the system including the presence of excess carbon and minor traces of ZrO_2 impurities and the range of oxynitride phases possible, further study using other techniques such as TGA-MS or high temperature *in situ* XRD is needed to fully understand the detailed oxidation process.

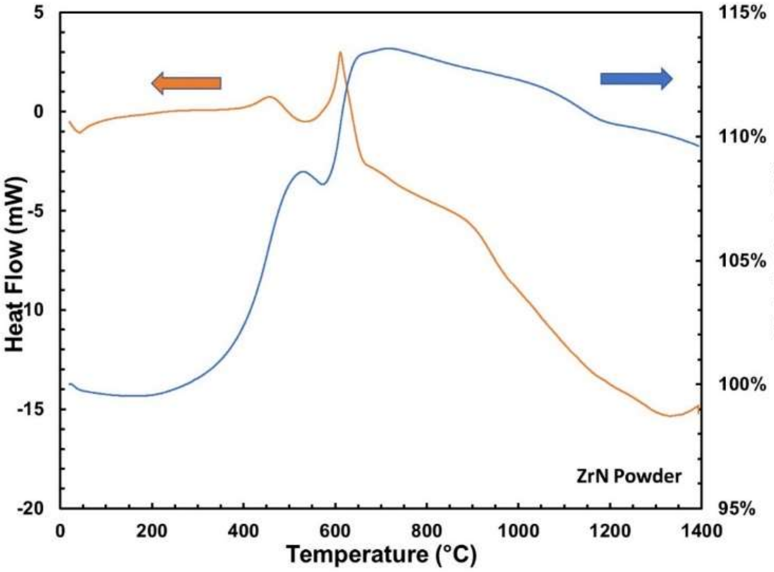

Figure 3. 9. TGA and DSC plots in air up to 1400◦C for ZrN powder synthesized with the modified soft urea route (Zr: urea molar ratio of 1:4, heat treatment at 1400 °C for 2 h in N_2).

The theoretical weight gain for complete oxidation to ZrO_2 should be 17.2% for pure ZrN and 17.4% for $Zr(C_{0.09}N_{0.91})$. On the other hand, the actual weight gain at 1400°C is only 9.7%. This suggests that the as-synthesized powder contain significant amount of free carbon up to ~6-7 wt.%. In fact, the sample was additionally analyzed for carbon content using LECO ASTM E1019-18 as a guide. The result shows that the *total* carbon content is around 6.03 wt.%. Because carbon exists as both as free carbon (see TEM images in figure 3.8) and in the lattice occupying the N site, it is difficult to precisely determine how much carbon is dissolved in the lattice replacing nitrogen and how much exists as free carbon. Nevertheless, the observation of much lower than ideal weight gain and the LECO analysis suggest significant amount of excess carbon in the powder, which is clearly a limitation for the modified soft urea method.

3.3.4. Flash sintering of synthesized ZrN powder

As mentioned before, flash sintering of the synthesized ZrN powder was performed in a homemade flash sintering setup. A constant voltage of 8 V was applied for 200 secs and the change in current with time is plotted in Figure 3.10 (Note the time is in log scale). Current in the sample increased first very quickly from ~ 4 A (current density 0.5 A/mm^2) at 0 secs to 100 A (current density 13.3 A/mm^2) at 5 secs, representing the flash phenomenon. After that current continues to increase up to 147 A (current density 19.5 A/mm^2) at ~100 secs. Beyond 100 secs the current decrease slightly to 140 A at ~200 secs. Figure S4 shows the change of electrical power and nominal temperature with time. Consistent with the current, power dissipation increased dramatically from ~29 W at 0 sec to 825 W at ~5 secs. It increased further to ~1200 W at ~100 sec. After that the power stabilized and became constrained by the power supply used (voltage limit 8 V). The measured temperature from the thermocouple is only up to 1040°C. However as explained before, the real sample temperature must be much higher because the thermocouple tip is several millimeters away from the sample. This limitation for our current flash sintering setup needs to be addressed in future [137] [139]. It should be noted that the flash sintering phenomenon observed here shares some similarity with the electrical resistive sintering (ERS) for metal powders such as Ti and Al [161] [162] [163] [164]. But it is also different due to the *high non-linearity*. In particular, if the amount of ZrN powder is doubled to 0.1 g, no flash occurred under the same pressure and applied voltage (meaning half of the electrical field of ~40 V/cm for ~2 mm thick green samples), while the current stayed below ~1 A even after >200 sec.

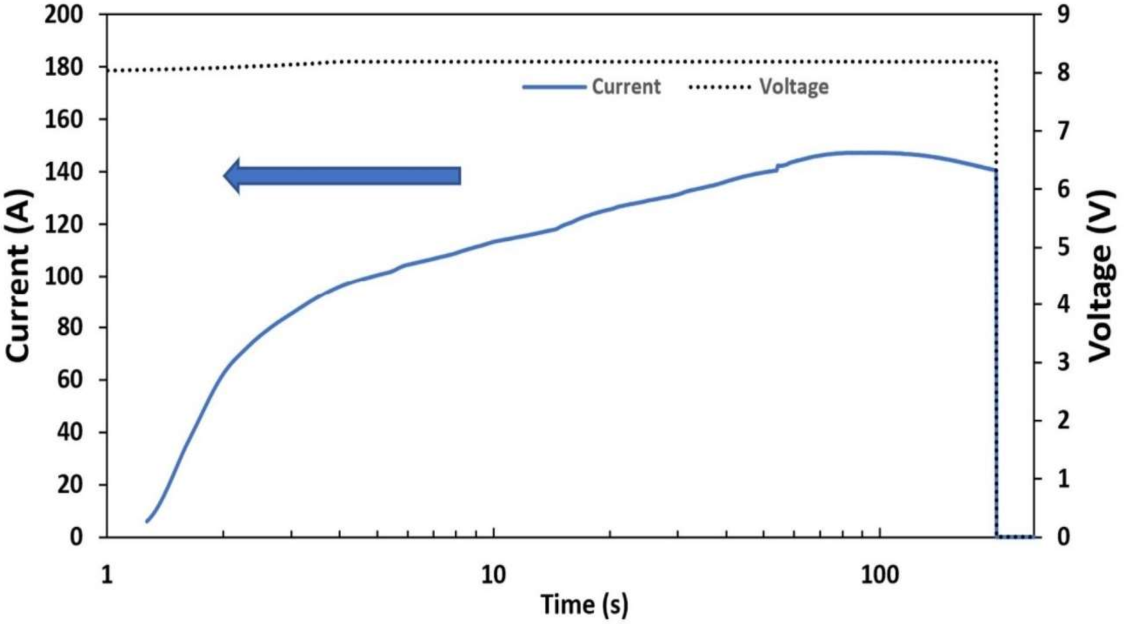

Figure 3. 10. Plot of applied voltage and resulting current vs. time (in log scale) for flash sintering of synthesized ZrN powder.

After flash sintering the sample was taken out by breaking the h-BN tube and the graphite electrodes. The obtained pellet was a golden in color after grinding and polishing to remove the graphite attached to the surface, as seen in Figure 3.1c. Relative density was calculated from the mass and dimension of the pellet to be 95.5% (Archimedes method was not used as sample size was too small). The XRD pattern for flash sintered sample (see S5) is very close to the powder except that the peaks become narrower indicating grain growth.

SEM images of the cross-section in Figure 3.11 show the flash sintered sample is quite dense. The grain size is approximately 10 μm. It is noted that the sample is not completely uniform, with some area containing more pores as shown in upper left of Figure 3.11a. Some other regions were extremely dense as shown in the lower part of Figure 3.11a and Figure 3.11b. SEM also shows the grains seem to contain many dimple-like structures. The nature of these is not clear and will be investigated in future. EDS on the flash sintered pellet shows that the N to Zr atomic ratio is 0.78± 0.15, while Vegard's law analysis based on XRD also shows stoichiometry of $Zr(C_{0.22}N_{0.78})$. This indicates that there might be nitrogen loss and enrichment in carbon in the sample during high temperature flash sintering.

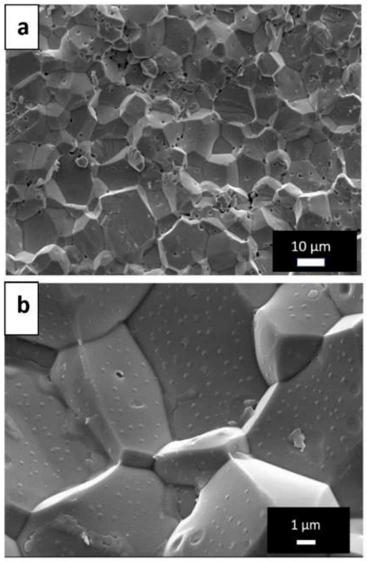

Figure 3. 11. (a-b) SEM images of a fractured surface of bulk flash sintered ZrN using powder synthesized from the modified soft urea route (Zr : urea molar ratio of 1:4, heat treatment at 1400 °C for 2 h in N_2).

3.3.5. Properties of flash sintered ZrN

Adachi et al reported Vickers hardness of 13.5 GPa[53] and Kathuria reported 13.8 GPa [165] for bulk ZrN. The Vickers hardness for the flash sintered ZrN was 16.6 ± 0.7 GPa, which was comparable to the above values.

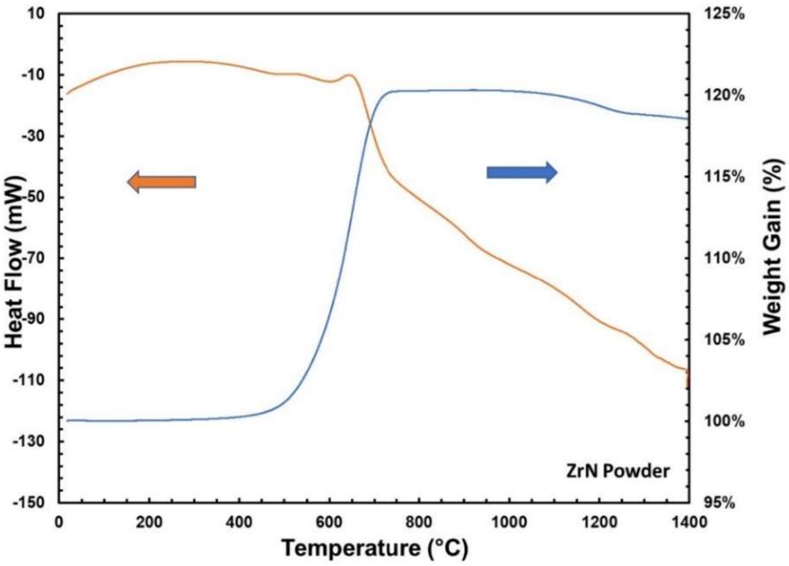

Figure 3. 12. TGA and DSC plots in air up to 1400◦C for bulk ZrN flash sintered from synthesized powder (Zr: urea molar ratio of 1:4, heat treatment at 1400 °C for 2 h in N2).

The thermal oxidation resistance of flash sintered ZrN was measured by TGA-DSC up to 1400˚C in air, as shown in Figure 3.12. From 25˚C to 450˚C no change in heat flow or weight of the bulk sample was observed. Starting from 450˚C there was a significant weight gain of up to 20.2% at 740 ◦C. This weight change also corresponds to the exothermic peak at 650◦C . The theoretical weight gain for complete oxidation of pure ZrN and $ZrC_{0.2}N_{0.8}$ to ZrO_2 is 17.2% and 17.6%, respectively. The higher-than-expected weight gain suggests that at 740˚C there might be residual nitrogen in the oxidation product. The measured weight gain at 1400˚C was 18.5 wt.%., The small sample weight loss from 740 to 1400˚C is hypothesized to be due to loss of nitrogen from the $Zr(O_xN_y)$ to ZrO_2, and further study is needed to verify this. Nevertheless, the low onset oxidation temperature of around 400˚C for such a dense sample suggest that ZrN might not be a good candidate for applications that require excellent oxidation resistance.

3.4. Conclusion

In the current study, a facile and low-cost modified soft urea route without using any solvent was used to synthesize ZrN powders. The products are fine powders and have low crystalline impurities but contains some carbon lattice dopant as well as free carbon. ZrO_2 was formed at lower temperature followed by carbothermal reduction/nitridation process to form the nitride. It was found that different synthesis parameters would influence ZrN formation. For example, a proper Zr : urea molar ratio is required to mitigate oxide formation and avoid too high carbon doping in the lattice. Enough temperature, dwell time and N_2 flow gas are needed to complete the reduction/ nitridation, but excess leads to undesirable results such as high carbon content. In addition, synthesized ZrN powder has been successfully flash sintered in a few minutes. The samples are dense with grain size of ~10 μm. TGA of the powder and the sintered pellet shows that ZrN has limited oxidation resistance with onset oxidation from 400˚C or even lower. To fully understand the materials properties, future study aimed at revealing the roles of defects especially vacancy in the nitrogen sub-lattice and the detailed oxidation process need to be carried out. Nevertheless, the methods and knowledge obtained here might be applied to the synthesis and processing of other technical ceramic materials.

Table 3. 1. Summary of processing conditions (nitrogen precursor used, precursors molar ratio, synthesis temperature, dwelling time and mixing atmosphere) for ZrN powder synthesis by the modified soft urea method and the phases of the final product. (The samples are arranged first by precursor molar ratio, then heat treatment temperature, then time, and then mixing atmosphere of the precursors. Some other parameters that were varied are listed in the footnotes.) * Argon gas instead of nitrogen gas **NH4Cl as N2 source instead of Urea

Sample ID	$ZrCl_4$: Urea molar ratio	T (◦C)	Holding time	Mixing Atmosphere	Actual phase(s) from XRD
N1	1:1	1400	2 h	Air	Major m-ZrO_2 & t-ZrO_2
N2	1:2	1400	2 h	Air	Major m-ZrO_2 & t-ZrO_2 minor $Zr(C_{0.02}N_{0.98})$
N3	1:4	600	2 h	Air	Major m-ZrO_2 & t-ZrO_2
N4	1:4	900	2 h	Air	Major m-ZrO_2 & t-ZrO_2
N5	1:4	1200	2 h	Glove Box	Major m-ZrO_2 & t-ZrO_2 minor $Zr(C_{0.04}N_{0.96})$
N6	1:4	1200	2 h	Air	Major m-ZrO_2 & t-ZrO_2 minor $Zr(C_{0.02}N_{0.98})$
N7	1:4	1300	10 min	Air	Major m-ZrO_2 & t-ZrO_2 minor $Zr(C_{0.07}N_{0.93})$
N8	1:4	1300	2 h	Air	$Zr(C_{0.11}N_{0.89})$
N9	1:4	1400	0 min	Air	Major $Zr(C_{0.00}N_{1.00})$ and t-ZrO_2 and minor m-ZrO_2
N10	1:4	1400	10 min	Air	Major $Zr(C_{0.17}N_{0.83})$ minor t-ZrO_2
N11	1:4	1400	2 h	Air	$Zr(C_{0.09}N_{0.91})$
N12	1:4	1400	2 h	Glove Box	$Zr(C_{0.25}N_{0.75})$
N13*	1:4	1400	2 h	Air	$Zr(C_{0.53}N_{0.47})$
N14**	1:8	1400	2 h	Air	Major m-ZrO_2 & t-ZrO_2 minor $Zr(C_{0.00}N_{1.00})$
N15	1:4	1600	2 h	Air	Major $Zr(C_{0.27}N_{0.73})$
N16	1:6	1400	2 h	Air	$Zr(C_{0.25}N_{0.75})$

3.5. Supplementary

S1 Calculated reaction free energy change versus temperature for the reaction $2ZrO_2 + 4C + N_2 = 2ZrN + 4CO$ at different partial pressure of CO.

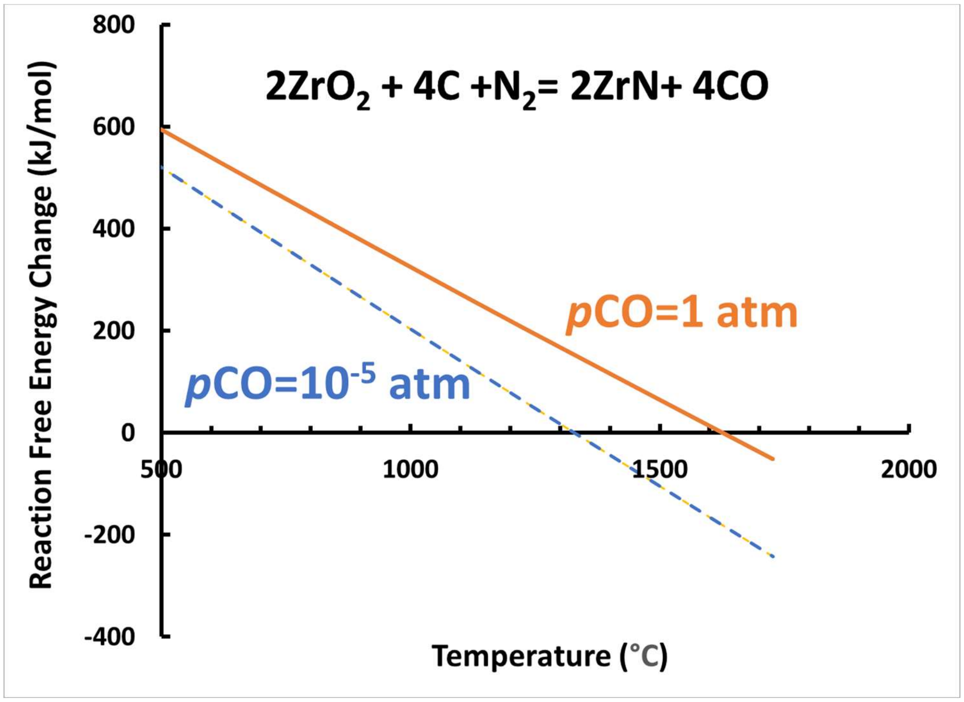

S2 XRD patterns of samples for which precursors were mixed in the glove box and air respectively with Zr: Urea molar ratio 1:4, and heat-treated at (a)1200°C and (b)1400°C for 2 h in N_2 (air mixing 1200°C N6; air mixing 1400°C N11; glove box mixing 1200°C N5; glove box mixing 1400°C N12)

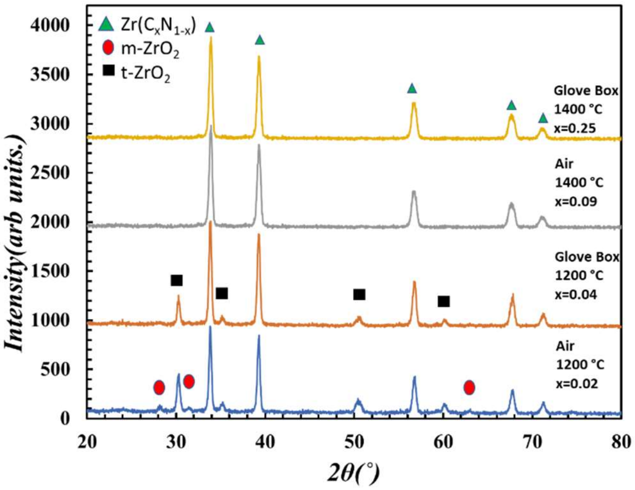

S3 XRD patterns of samples synthesized using NH_4Cl (Zr: NH_4Cl molar ratio 1:8, N14) and urea (Zr: urea molar ratio 1:4, N11), respectively with heat treatment at 1400 °C for 2 h in N_2

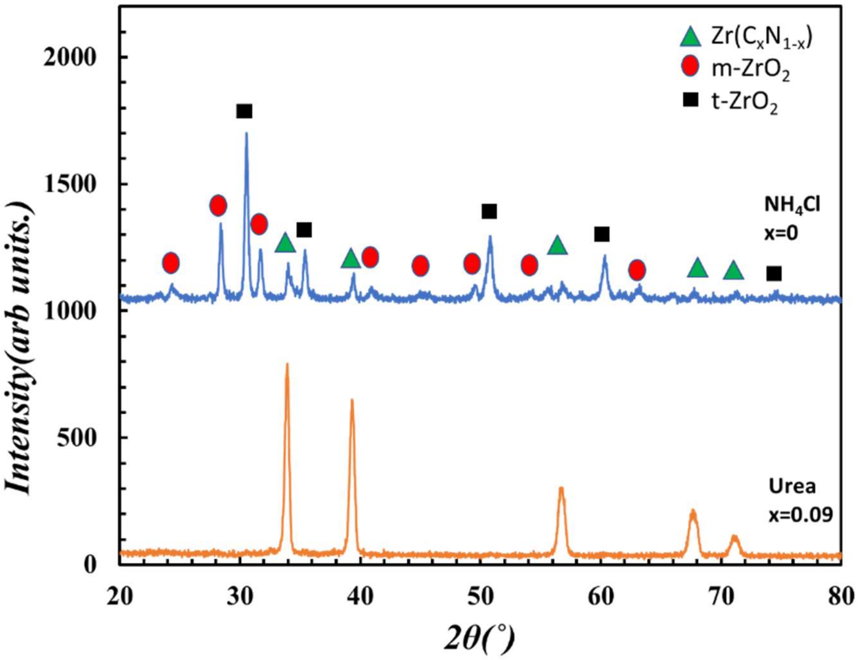

S4 Plot of temperature and power vs. time for flash sintering of synthesized ZrN powder. Note the temperature increase was delayed relative to the sudden increase of power because of insensitivity of the thermocouple used at low temperature and the distance between the thermocouple tip and the sample, as explained in the experimental section.

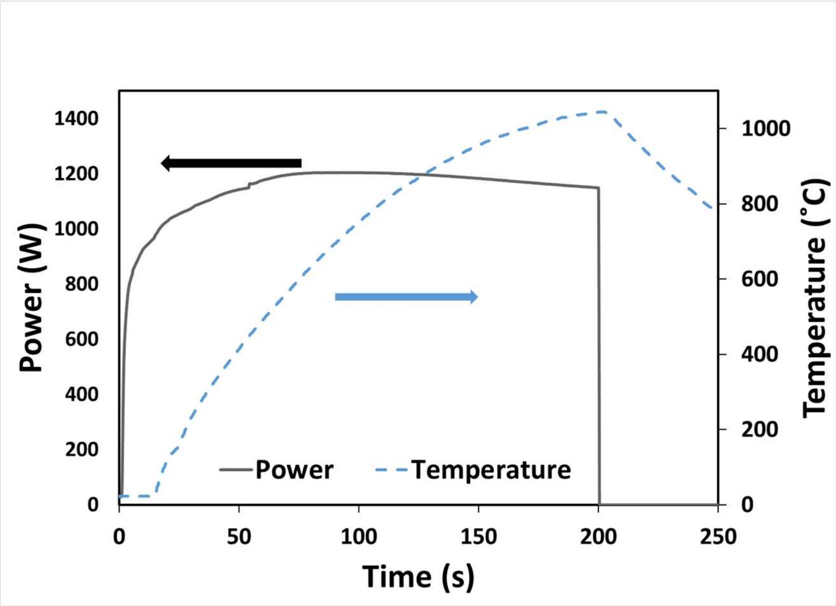

S5 XRD pattern for flash sintered ZrN pellet after it was crushed into powder. *m* and *t* are for trace amount of monoclinic and tetragonal ZrO_2. EDS on the flash sintered pellet shows that the N to Zr atomic ratio is 0.78 ± 0.15, while Vegard's law analysis based on XRD also shows stoichiometry of $Zr(C_{0.22}N_{0.78})$.

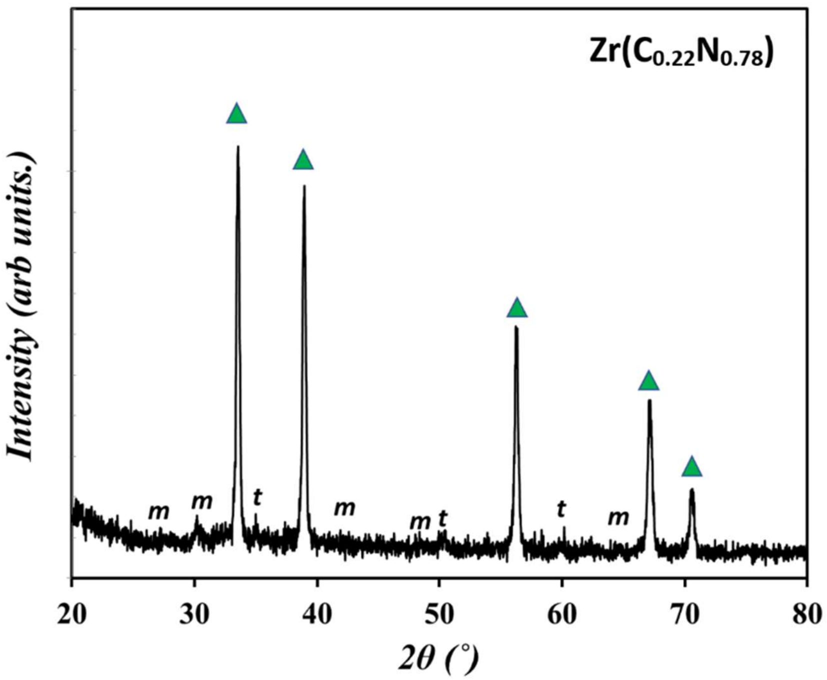

Chapter IV: Reactive Flash Sintering of TiZrN and TiAlN Ternary Metal Nitrides

The following *chapter* is based on the author's paper Suprabha Das, Andriy Durygin, Vadym Drozd, Md Shariful Islam Sozal, Zhe Cheng, Reactive flash sintering of TiZrN and TiAlN ternary metal nitrides, Journal of the European Ceramic Society, Volume 44, Issue 4, 2024, Pages 2037-2051, ISSN 0955-2219, https://doi.org/10.1016/j.jeurceramsoc.2023.11.079.

4.1. Introduction

In the past decade, research on ternary metal nitrides (TMN) has attracted significant interest [11, 166]. They are known to exhibit desirable properties such as high hardness, abrasion resistance, good chemical and thermal stability, high thermal and electrical conductivity (even superconductivity), and oxidation resistance. This makes them promising candidates for hard coatings [9, 167, 168] and high-temperature protection systems against hostile environments [169]. Among TMN, $Ti_{1-x}Zr_xN$ and $Ti_{1-x}Al_xN$ have gained special attention due to their enhanced mechanical properties and thermal stability as compared to the corresponding binary nitrides [170–174]. For example, while TiN and ZrN thin films are known for their high hardness and excellent corrosion resistance [175, 176], alloying them together to form $Ti_xZr_{1-x}N$ (e.g., $x = 0.3$ and 0.5) *solid solution* further improves the hardness (due to the solid-solution hardening effect) and even oxidation resistance (though mechanism not very clear) [177]. Similarly, compared to neat TiN, $Ti_{1-x}Al_xN$ (e.g., $x = 0.5$ or 0.63) thin films are known to exhibit better oxidation resistance by forming an aluminum oxide layer on their surface, which slows oxygen diffusion [178]. $Ti_{1-x}Al_xN$ coatings also show increased hardness over TiN because of an age-hardening phenomenon that comes from phase separation from meta-stable $Ti_{1-x}Al_xN$ solid solution to separate TiN and AlN phases [16] Due to these advantages, $Ti_{1-x}Zr_xN$ as well as $Ti_{1-x}Al_xN$ have been used as high-performance coatings for machining and other applications [180, 181].

Despite attractive properties of $Ti_{1-x}Zr_xN$ and $Ti_{1-x}Al_xN$, most studies on their preparation have concentrated on thin films [10, 171, 177, 179]. There is no study on *bulk* $Ti_xZr_{1-x}N$, while studies on *bulk* $Ti_{1-x}Al_xN$ either require high sintering temperature/prolonged heat treatment time or have contamination issues [74].

Apart from synthesis, the *phase transition* in these TMN materials is another interesting area that remains to be clarified, especially for *bulk ceramics*. Theoretically, researchers have used density functional theory (DFT) method to evaluate the phase equilibrium [10, 182, 183], and both TiN-AlN and TiN-ZrN pseudo-binary systems are shown to have a miscibility gap with a critical temperature of 1837°C and 1606°C, respectively [184, 185]. During equilibrium cooling from the single-phase region or annealing of the metastable phase, $Ti_{1-x}Zr_xN$ and $Ti_{1-x}Al_xN$ uniform solid solutions are expected to go through phase separation (e.g., via spinodal decomposition) into *c*TiN + *c*ZrN and *c*TiN + *c*AlN, respectively (*c* represents cubic phase; *c*AlN is metastable and would subsequently transform to hexagonal or *h*AlN). The phase separation into fine, often nano-sized domains (or phases) with different compositions leads to the aforementioned hardening effect and better mechanical properties for these TMNs. Experimentally, techniques such as *in situ* XRD has been used to investigate the phase transformation in these TMNs; but again, all related studies have been limited to thin films [168, 170, 171]. It is not clear if and how such phase transformations would occur in *bulk* TMN ceramics. In addition, not much is known about the *bulk* TMN *formation* processes, such as how fast they are and if there is any difference from the well-studied thin films.

Recently, flash sintering (FS) has emerged as a new field-assisted sintering technique for various ceramic materials. In FS, an electric field (often DC) is applied to the sample. Current is forced to only go through the sample and it increases drastically in a short time due to the large drop in sample (effective) resistance with increasing temperature, leading to *self-accelerated* heating and rapid densification within minutes or even seconds [6, 137, 139, 186–190]. Flash sintering may also be applied to a mixture of different powders and achieve both fast reaction and densification in one heat treatment [191–193], and an example is the reactive flash sintering (RFS) of $BiFeO_3$ from a Bi_2O_3 and Fe_2O_3 powder mixture [194].

This study aims to explore if RFS could be used for preparing *bulk* TMN for the TiN-ZrN (both phases conducting) and the TiN-AlN (TiN conducting while AlN insulating) systems. In addition, because the flash and the associated reaction would be very quick, *in situ* synchrotron XRD experiments are performed at elevated temperatures during RFS and subsequent cooling for real-time characterization of the phase transitions for the two systems. Finally, properties such as oxidation resistance, hardness, and fracture toughness for the obtained bulk TMNs are evaluated and correlated with the materials' phase composition and microstructure. The similarity and differences in RFS behaviors and related phase transitions are also revealed for the two systems and the directions for future research are pointed out.

4.2. Materials and methods

4.2.1. Raw materials and mechanical mixing

The synthesis of TMNs was carried out by RFS from commercial powders of zirconium nitride (99.5% metals basis excluding Hf, Hf<3%, Alfa Aeser #12138) and titanium nitride (99.5% metal basis, Alfa Aeser #41556). For aluminum nitride, two types of powders were used: one has a particle size of 10 μm (≥98%, Sigma Aldrich #241903, named *micron AlN* below) and was used for most RFS (named *standard RFS* below), while the other was nano powder (<100 nm, Sigma Aldrich #593044, named nano AlN below) and was used for *in situ* synchrotron RSF experiments (named *in situ RFS* below). XRD analysis indicates the commercial TiN powder is single-phase and does not contain significant crystalline impurities, commercial ZrN contains tetragonal ZrO_2 (~4.1 wt.% from Rietveld refinement), micron AlN is hexagonal phase, while nano AlN has both cubic and hexagonal phases, as shown in Figure S1. According to Rietveld refinement, all commercial nitrides have a small (<~5%) nitrogen deficiency. For mechanical milling, *equimolar* TiN-ZrN mixture or TiN-AlN mixture was Spex milled using SPEX Sample prep (8000D-115 Mixer/Mill). A stainless steel jar and ball were used to mill the powders for 5 mins before RFS, targeting the TMN with *nominal* composition of $Ti_{0.5}Zr_{0.5}N$ and $Ti_{0.5}Al_{0.5}N$, respectively.

4.2.2. Flash sintering setup

The flash sintering setup was developed in the lab and has been explained in detail in previous publications [6, 137, 139]. For standard RFS, 90 mg of the Spex-milled equimolar precursor powder mixture was uniaxially cold pressed into a cylindrical pellet at a pressure of ~ 2400 MPa. The diameter of the cold-pressed pellets was 3.1 mm. Next, a cold-pressed pellet was inserted into a hexagonal boron nitride (*h*-BN) tube with two graphite electrodes touching the pellet at the two ends. Then the assembly was inserted into an outer *h*-BN tube confined by a graphite sleeve. The inner graphite electrodes touched the outer graphite electrodes, which also helped prevent the sample from excessive oxidation. Finally, the entire setup was placed in an environment chamber (made of aluminum) purged with flowing argon gas (UHP grade, Airgas). The copper terminals in contact with the outer graphite electrodes had water cooling to maintain their temperature. The Argon purged environment chamber helped extend the lifetime of graphite components by minimizing oxidation and allowing their reuse. A constant DC voltage of 8 V was initially applied by a DC power supply (Hewlett Packard, 6671A, 8 V, 220 A) between the two copper terminals with a constant pressure of 15 MPa applied by a pneumatic cylinder. Figure S2 shows the mechanical drawing and photos of the setup including the environmental chamber used. After standard RFS, the system was cooled to room temperature followed by the removal of the sample. Table 4.1. summarizes sample ID, standard (reaction) flash sintering conditions, the products' phase composition and relative density, as well as the results of thermal oxidation and mechanical tests for different samples. It should be noted that voltage higher than 8 V was not used due to the limit of the power supply, while voltage lower than 8 V led to lower (max) current and power, which would slow down solid solution formation and densification.

4.2.3. Materials characterization

Except for *in situ* RFS, all other materials characterization such as *ex situ* XRD, microstructure analysis by SEM and EDS, as well as oxidation resistance and mechanical properties (hardness and fracture toughness) were all obtained from standard RFS specimens. A Smart Lab SE X-ray diffractometer with Cu-Kα radiation (λ=1.54059 Å for Kα1) was used to collect X-ray diffraction patterns. XRD was taken on crushed powders. The microstructure and elemental distribution of standard (reactive) flash-sintered pellets were analyzed using a scanning electron microscope (SEM JEOL JSM-F100) fitted with energy-dispersive X-Ray spectroscopy (EDS). Thermogravimetric analysis (TGA) and differential scanning calorimetry (DSC) for fractured pieces from standard (reactive) flash-sintered pellets were carried out using a TA instrument SDT Q600 from 25˚C to 1400˚C in air with a 5˚C/min heating rate to evaluate the resistance to thermal oxidation. Some standard (reactive) flash sintered samples were mounted in resin and ground and polished down to 0.1 μm polycrystalline diamond slurry. Then, the polished samples were tested for Vickers hardness and fracture toughness using LECO LM810AT (LECO Corporation). A load of 2000 gf and a diamond tip were used, and the indentation test was performed along the ~3 mm sample diameter to ensure representation and accuracy of the result. Cracks from the indentations were observed using SEM and the measured crack lengths were used to calculate fracture toughness.

As to *in situ* synchrotron RFS experiments, they were carried out to capture changes in materials' phase composition, crystal structure, and lattice constants and provide insights about the underlying physical/chemical processes *during* RFS for both TiN-ZrN and AlN-TiN systems. Specifically, synchrotron angle dispersive XRD experiments (including both *ex situ* and *in situ* ones) were performed at sector 16 of the Advanced Photon Source (APS) in Argonne National Laboratory (ANL). To prepare for the *in situ* synchrotron RFS experiments, the setup was modified to allow for X-ray penetration. As described, an environment chamber that allows the conduction of *in situ* RFS experiments under a controlled atmosphere was used. The size of the chamber was ~ 60 cm × 25 cm × 25 cm and it fitted the space available on the general-purpose table at the beamline 16-ID-B at the APS synchrotron facilities, as shown in Figure 4.1. X-ray transparent high-temperature resistant polymer (Kapton®) film was used as the window material for the environment chamber. In addition, to let the incident X-ray and the diffracted beam pass through the sample, the sample diameter was reduced from ~3 mm in the standard RFS design to ~1.5 mm, while the sample height was ~2 mm (Note: For X-ray penetration, a hole was opened on the side through the graphite outer sleeve and the *h*-BN outer tube as shown in Figure S2(d)). Also, for *in situ* RFS experiments, the powder mixture was directly loaded into the sample assembly and not pre-compacted into a pellet due to the very small sample size. A different DC power supply with a higher voltage limit but a lower current limit (Hewlett Packard, 6031A, 20 V, 120 A) was used for all *in situ* synchrotron RFS experiments, due to expected increase in sample resistance from reduced sample diameter. The wavelength of the monochromatic X-ray synchrotron radiation was 0.4246 Å. The X-ray beam was focused to ~2 μm × 4 μm size. A high-frequency area PILATUS 1M detector providing a minimum acquisition period of 8 ms was used to collect the 2D diffraction patterns. XRD patterns were recorded every second during the *in situ* RFS experiments.

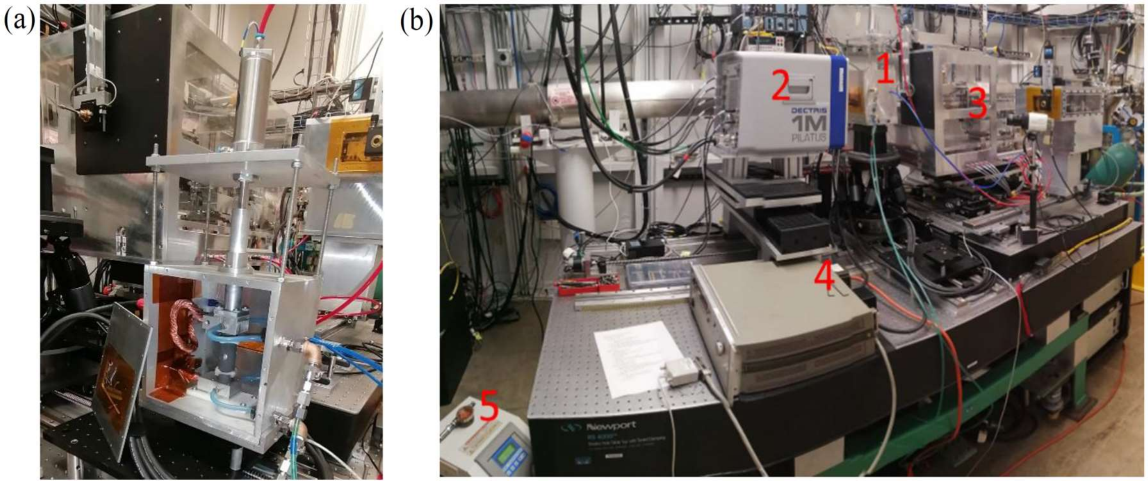

Figure 4. 1. (a) A photo of the setup including the environmental chamber used for in situ synchrotron XRD study of the reactive flash sintering (RFS) process. Note the sample assembly had been installed, pressure was applied, and the front panel was removed to show the inside of the chamber. (b) A photo showing the reactive flash sintering setup installed on the 16ID-B General Purpose Table located at Sector 16 of the Advanced Photo Source (APS) facility in Argonne National Laboratory (ANL) for the in situ synchrotron RFS study: (1) flash sintering setup, (2) 2D X-ray detector, (3) X-ray focusing setup, (4) power supply used in the RFS experiment, (5) water chiller for the chamber.

4.3. Results and discussion

4.3.1. Reactive flash sintering behaviors for TiZrN and TiAlN

Figures 4.2 and 4.3 show the changes in current with time for standard RFS of the samples of std-TZN (from TiN-ZrN mixture targeting $Ti_{0.5}Zr_{0.5}N$) and std-TAN (from TiN-AlN mixture targeting $Ti_{0.5}Al_{0.5}N$), respectively. As stated, for both cases, the initial constant DC voltage applied was 8 V, the applied mechanical pressure was 15 MPa. For std-TZN, since both starting TiN and ZrN are highly conductive (room temperature *bulk* conductivity of ~37000 S/cm [195] for TiN and ~20000 S/cm [196] for ZrN), flash or the rapid increase in current happened instantaneously – within the first second of turning on the DC power source: As shown in Figure 4.2, at 0.58 s, the current was already 134 A, corresponding to a current density *j* of 17.8 A/mm^2 (note: sample diameter ~3.1 mm; same below) and power dissipation of 1069 W. Current increased further to 179 A (23.7 A/mm^2)

at 1 s and 195 A (25.8 A/mm^2) at 2.3 s. Current reached the maximum set value of 200 A at ~23 s, corresponding to j of 26.5 A/mm^2 and the system reached peak power of ~1600 W. After that, the power stabilized near the maximum value under 8 V DC with a gradual drop in current over time to 193 A (25.6 A/mm^2) at 350 s when the power supply was turned off and the entire assembly was allowed to cool to room temperature. (It should be mentioned that we choose *not* to provide the (maximum) *power density* and *electrical field* values here because the exact resistance/power/electrical field distribution in the system is still uncertain at this moment due to the complexity of the system containing the sample, multiple graphite/copper electrodes, as well as the contacts between different parts/materials.)

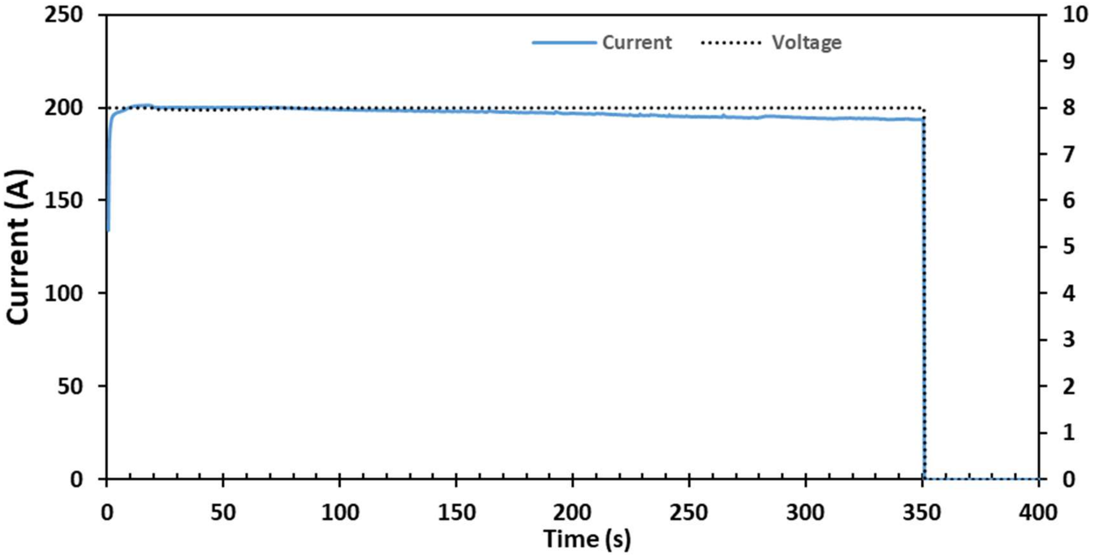

Figure 4. 2. Plot of applied voltage (dotted line) and resulting current (solid line) vs. time for RFS of the std-TZN sample from TiN and ZrN powder mixture (both conducting, 1: 1 molar ratio). Note the maximum current of 200 A corresponds to a current density of 26.5 A/mm^2.

In comparison, for the std-TAN sample, the flash did *not* happen instantly, as shown in Figure 4.3: With the *same* 8 V DC and 15 MPa pressure, the starting TiN-AlN powder mixture appeared much less conductive since AlN is insulating. As a result, the incubation stage became much longer: At 0.54 s, the current was only 0.337 A (0.045 A/mm^2), and the total power was only 2.7 W. Initially, the current increase was slow: only to 4.21 A (0.56 A/mm^2) at 47 s. Then the current suddenly spiked up: within 3 s, it increased dramatically by more than 40 times to 171 A (22.6 A/mm^2) at 50 s, corresponding to the *flash* event. Accordingly, power jumped from 34 W to 1368 W in the same three-second time frame, demonstrating the immense rate of a power surge during RFS for the TAN sample. After this, the current continued to increase, but at a slower rate until reaching the same maximum set value of 200 A (26.5 A/mm^2) and a maximum power of ~1600 W. At that point, the power supply automatically switched to constant current mode and the voltage dropped gradually to 7.47 V at 400 s (power of 1494 W) when the power supply was turned off and the entire assembly was allowed to cool to room temperature. Overall, the RFS experiment for the std-TAN sample included *three distinct stages*: incubation, flash, and post-flash steady state, as in typical flash sintering.

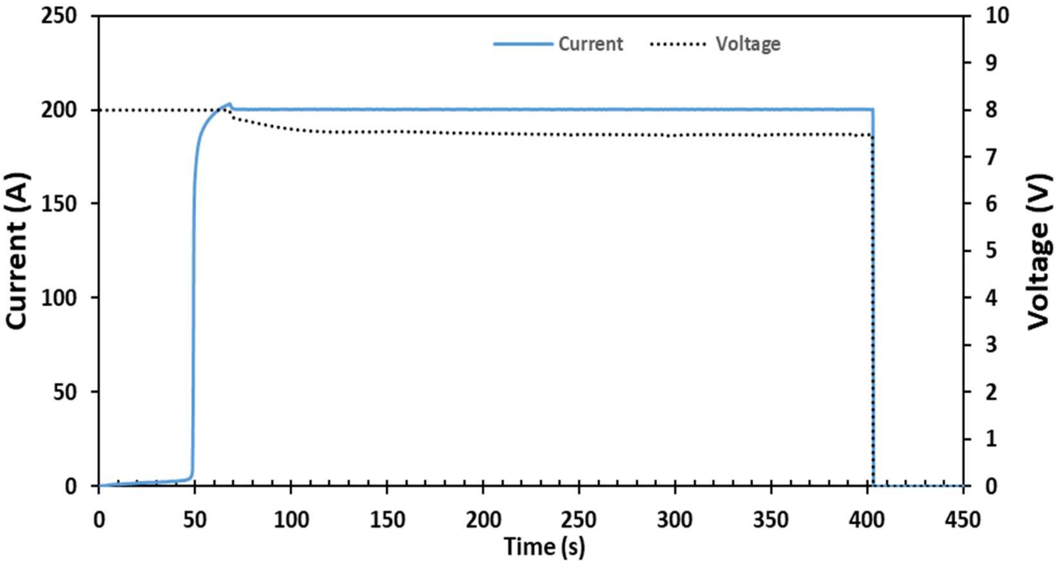

Figure 4. 3. Plot of applied voltage (dotted line) and resulting current (solid line) vs. time for RFS of the std-TAN sample from TiN and AlN powder mixture (TiN conducting, AlN insulating, 1: 1 molar ratio). Note the experiment started in the constant voltage mode and the power supply switched to constant current mode when the current reached the set limit of 200 A (26.5 A/mm^2).

Apart from std-TZN and std-TAN, for comparison purpose, standard flash sintering was also carried out for binary nitrides of TiN and ZrN, *individually*, using the same setup with the same parameters (i.e., initial 8 V DC, 15 MPa pressure, 200 A current limit, ~350 s total time). The resulting current-time plots are shown in Figures S3(a) and (b), respectively. (AlN could *not* be flash sintered using the current setup due to its insulating property, even at elevated temperatures.) Both std-TN (from TiN) and std-ZN (from ZrN) samples behaved similarly to the std-TZN sample, showing instant flash, but the max current was ~193 A (25.6 A/mm^2) - lower than the 200 A limit. As a result, there was *no* switching to the constant current mode.

After standard (reactive) flash sintering, all pellets were extracted from the *h*-BN tube and separated from the graphite electrodes, ground to remove graphite attached to the surface, and characterized using various techniques.

4.3.2. Phase transformation *during* reactive flash sintering of TiZrN and TiAlN

4.3.2.1. Characterization by *ex situ* XRD

Figure 4.4 shows the XRD patterns for the std-TZN sample before and after standard RFS. Before RFS, the 5 min Spex-milled sample was a mixture of TiN and ZrN with a trace of *t*-ZrO_2. After RFS, the sample turned into a single-phase nitride solid solution with no obvious peak splitting. The diffraction pattern matches the same NaCl-type crystal structure as TiN and ZrN with a calculated lattice parameter of 4.3896 ± 0.0009 Å. Based on Vegard's law and assumptions that the lattice parameter for stoichiometric TiN is 4.241 Å (PDF Card: 04-002-1925) and ZrN is 4.585 Å (PDF Card: 04-004-2860), the composition after RFS was estimated as $Ti_{0.57}Zr_{0.43}N$, which was reasonably close to the target composition. Minor impurity phase of t-ZrO_2 (PDF card: 01-081-1546) was detected after RFS, most likely due to the ZrO_2 impurity already present in the commercial ZrN powder, as shown in Figure S1. Graphite (PDF card: 04-041-0362) was also detected in the sample after RFS, which was attributed to contamination from the graphite electrodes attached to sample after high temperature RFS. The XRD result confirmed the presence of a single-phase region at elevated temperature for the TiN-ZrN system [184], while rapid water cooling in current RFS setup from the single-phase region *preserves* the meta-stable single-phase solid solution in *bulk ceramics* to room temperature.

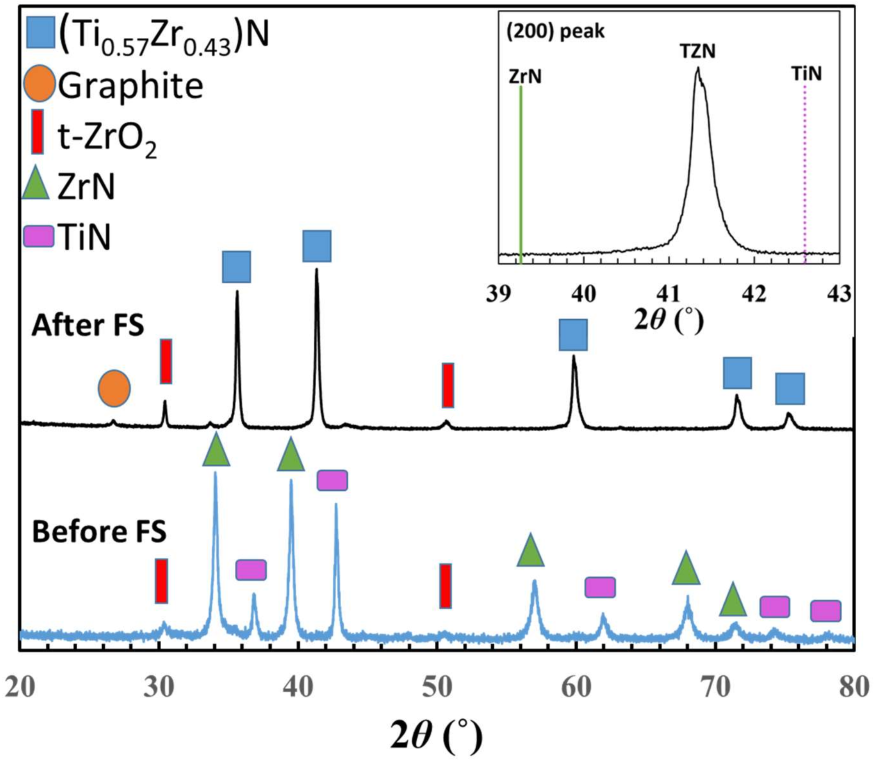

Figure 4. 4. XRD patterns of the std-TZN sample (from TiN-ZrN equimolar mixture targeting $Ti_{0.5}Zr_{0.5}N$) before and after standard RFS. The sample formed a single-phase solid solution with composition of $Ti_{0.57}Zr_{0.43}N$ (as determined by XRD and EDS) after RFS. Impurities such as ZrO_2 and graphite were also present after RFS. The insert is the zoomed-in section showing the (200) diffraction peak. The expected peak positions for pure TiN and ZrN are also marked.

Figure 4.5 shows the XRD patterns for the std-TAN sample before and after standard RFS. Before RFS, the 5 min Spex-milled sample was a mixture of TiN and *h*-AlN. After RFS, unlike TZN, the peaks for TiN remained largely the same, except the peaks shifted slightly to lower angle, especially for the high index planes. Analysis suggested the lattice parameter *expanded* slightly from 4.2442 ± 0.0006 Å for the Spex-milled mixture to 4.2555 ± 0.0003 Å for the RFS sample. In addition, the sample after RFS contained minor impurity of TiO (PDF Card: 04-007-4073), $Ti_{0.9}Al_{0.1}C$ (PDF Card: 04-021-6313), as well as graphite contamination. The appearance of TiO was attributed to the partial oxidation of TiN in low pO_2 atmosphere. The origin for $Ti_{0.9}Al_{0.1}C$ is not clear: It is hypothesized to come from conversion of Al-doped titanium nitride to corresponding carbide during extended heating (up to 400 s in this case) at high temperature (e.g., > ~1600ºC, see later discussion on thermal simulation) in the RFS process, and further study is needed to understand it.

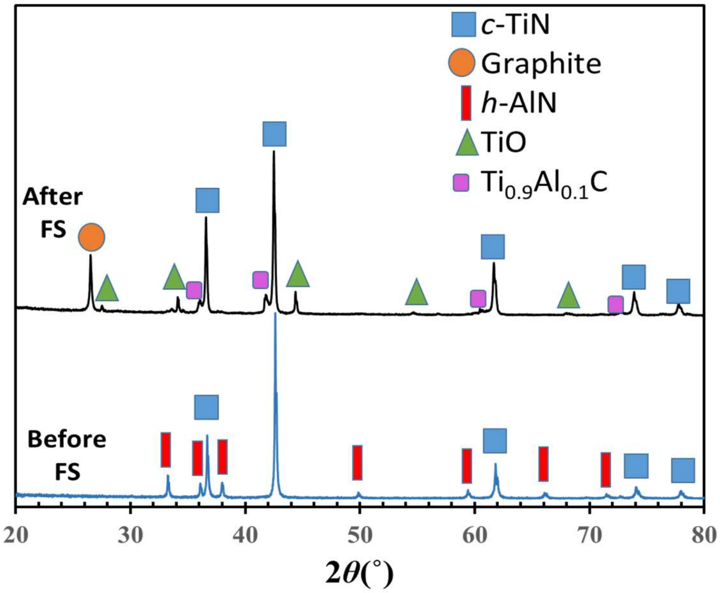

Figure 4. 5. XRD patterns of the std-TAN sample (from TiN-AlN equimolar mixture targeting $Ti_{0.5}Al_{0.5}N$) before and after standard RFS. Note TiN peaks shifted slightly to the left (lower angle) after RFS, while h-AlN seems to have disappeared. Impurities of TiO (likely due to partial oxidation of doped TiN) and $Ti_{0.9}Al_{0.1}C$ (likely due to conversion from nitride to carbide upon extended holding at high temperature) are also present after RFS.

4.3.2.2. Characterization by *in situ* synchrotron X-ray diffraction

Despite the *ex situ* XRD study, several important questions about phase transformation remain, especially for the bulk TiN-AlN system. For example, first, it is not clear if (Ti, Al)N solid solution had ever formed *during* the RFS process. As mentioned, the calculated phase diagram for the *c*TiN - *c*AlN system shows a continuous solid solution with a miscibility gap below a critical temperature of ~1837°C [184]. However, that phase diagram is of limited use since at room temperature, *c*AlN is stable only at high pressure, while *h*AlN is the thermodynamically stable phase under ambient pressure and is used as the starting material (i.e., micron AlN, which is all hexagonal phase, see Figure S1) for standard RFS. Second, due to the limitation of the current flash sintering setup, the actual sample temperature could *not* be measured. (Thermocouples had the challenge of the tip getting melted, while infrared measurement suffered from the large temperature gradient from the center to the outside in the FS sample assembly.) As a result, it was not clear if the sample ever reached or exceeded the critical temperature. Third, even if the critical temperature was reached, whether the sample stayed as separated phases due to slow diffusion/limited reaction or the sample first formed a solid solution and then went through subsequent decomposition back into TiN and other phases is not clear. To answer these questions, at least partly, the phase transformation during RFS was also studied in real time using synchrotron-based *in situ* XRD, and the results are presented below.

- *Electrical characteristics for in situ RFS*

In situ synchrotron study was carried out for RFS of the TiN-ZrN or the TiN-AlN powder mixtures (both at 1: 1 molar ratio) using the setup described earlier. As mentioned, the sample diameter was reduced from 3.1 mm for standard RFS to 1.5 mm to let the incident X-ray and the diffracted beam pass through the sample. Also, the powder mixture was directly loaded into the sample assembly and not pre-compacted into a pellet due to the very small sample size. These two adjustments are expected to make the *in situ* RFS sample more resistive than the standard RFS samples and a higher voltage would be needed to overcome this resistance increase and initiate the flash. Therefore, a different DC power supply with a higher voltage (Hewlett Packard, 6031A, 20 V, 120 A) was used in the *in situ* RFS experiments to overcome the samples' higher resistance compared to the standard RFS samples. In addition, as the voltage to trigger the flash was unknown, the *in situ* sample was subject to a linear DC *voltage ramp* at 0.1 V/s starting from 0 V instead of a constant voltage (i.e., 8 V DC) in standard RFS. It should be mentioned that these changes resulted in some discrepancies, especially in terms of maximum current densities (see below), between *in situ* RFS and standard RFS. Optimization of the processing parameters including for *in situ* synchrotron RFS will be part of future studies.

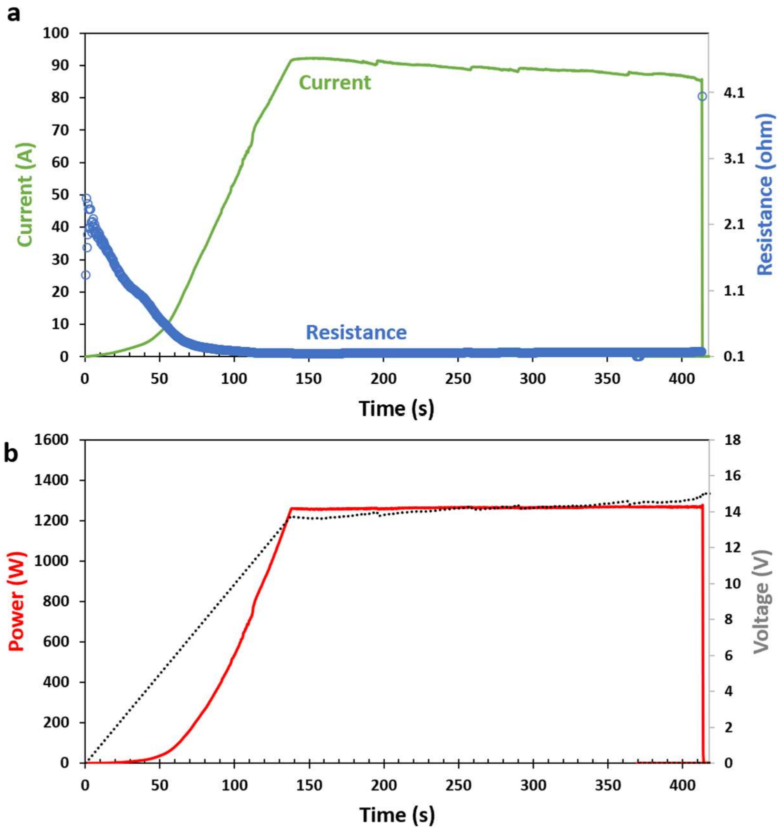

Figure 4. 6. Plots of (a) current and total resistance and (b) voltage and power versus time for the in situ TZN sample (from TiN-ZrN equimolar mixture) with the RFS processing monitored in real time by synchrotron at the APS facility in ANL. The voltage was linearly ramped up from 0 V at a rate of 0.1 V/s, while the power spiked up non-linearly from ~40 s, reaching the max power of ~1.3 kW with a max current of ~92 A (52 A/mm^2) at ~140 s, and then stabilized.

Figures 4.6 and 4.7 show the electrical characteristics (voltage, current, power, and total resistance) versus time plots during the *in situ* RFS experiment, monitored by *in situ* synchrotron, for the TiN-ZrN and the TiN-AlN powder mixtures, respectively. For *in situ* TZN (from TiN-ZrN equimolar mixture, see Figure 4.4.6), as stated, unlike the standard RFS carried out at *constant voltage* of 8 V (Figure 4.2), the linear ramp of the voltage from 0 V at 0.1 V/s did *not* lead to flash instantaneously. Instead, the current increased first slowly as voltage increased. Then from ~45 s at a voltage of ~4.5 V, current started to rise much faster. Total current increased from ~0.03 A at 1 s (0.017 A/mm^2) to 5.7A at ~45 s

(3.2 A/mm^2) and 91.9 A at ~140 s (52 A/mm^2), while system's total resistance dropped from ~2.5 Ω at 1 s to 0.83 Ω at ~45 s and 0.15 Ω at ~140 s (see Figure 4.6(a)).

For *in situ* TAN (from TiN-AlN equimolar mixture, see Figure 4.7), like before (Figure 4.3), there was an incubation stage, but it was longer with the flash occurring at ~123 s at an applied voltage of ~12.3V. The resistance dropped first gradually from ~87 Ω at 26 s (data before 26 s *not* reliable due to very low and *unsteady* current) to ~42 Ω at 100 s, while total current increased from ~ 0.03 A (0.016 A/mm^2) to ~ 0.21 A (0.118 A/mm^2). Then, at ~123 s, the abrupt flash occurred with the resistance dropping by ~100 times in less than two seconds - from 15.7 Ω at 122.8 s, to 0.166 Ω at 124.2 s, while the total current increased from 0.78 A (0.441 A/mm^2) at 122.8 s to 74.43 A (42.14 A/mm^2) at 124.2 s. Afterwards, the resistance was relatively stable with value of 0.17 Ω. Accordingly, total power dissipation jumped from 0 W at the beginning to 0.074 W at ~26 s to 2.4 W at 100 s. Near 123 s, power increased drastically in less than 3 s from 9.5 W at 122.8 s to 921 W at 124.2 s. Power continued to increase a little more to ~1250 W at ~138 s when the power supply reached max current of 91.1 A (~52 A/mm^2) and stabilized afterwards. The longer incubation with higher critical voltage (or electrical field) for *in situ* TAN than the std-TAN (shown in Figure 4.3) is attributed to the fact that the starting AlN powder used for the *in situ* TAN synchrotron RFS experiment had a much *smaller average particle size* (~50 nm) than the 10 μm AlN powder used for standard RFS, with the hope that nano AlN might promote the reaction with TiN. Later at ~170 s, the current & power dropped to essentially zero, accompanied by a large increase in voltage, which was attributed to a mechanical failure of the thin (~1.5 mm diameter) graphite electrodes, and the experiment was stopped.

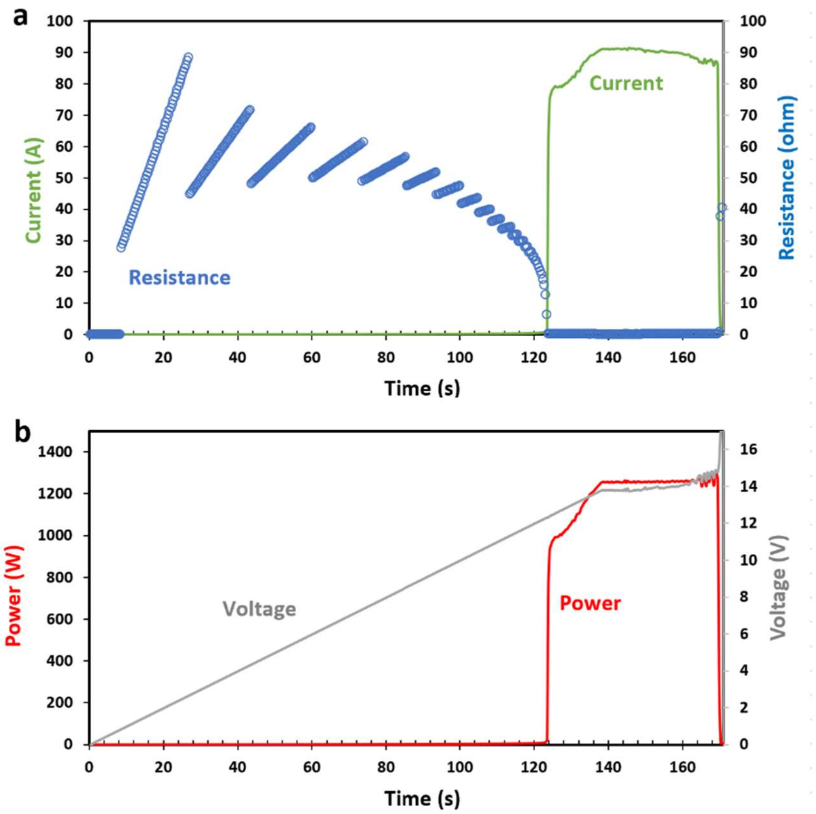

Figure 4. 7. Plot of (a) current and total resistance, (b) voltage and power versus time for the in situ TAN sample (from TiN-AlN equimolar mixture) with the RFS processing monitored in real time by synchrotron at the APS facility in ANL. The voltage was linearly ramped up from 0 V at a rate of 0.1 V/s, while the power displayed incubation before ~123 s, flash at ~123-124 s. After ~125 s, as the voltage continued to ramp up, current kept increasing but slowly, reaching a max power of ~1.3 kW with current of 91.1 A (~52 A/mm^2) at ~138 s. At 170 s, the electrode fractured, and the current dropped to zero, after which the experiment was stopped. It should be mentioned that the zig-zagged shaped data for resistance in (a) before ~120 s were purely an artefact from the power supply due to limitation with electrical control, while the black dash line is for guidance only, showing the behavior of gradual and then sudden drop in resistance with time.

It should be noted that Figure 4.7 includes the nominal total resistance calculated from total current and voltage. The zig-zagged behavior is purely an *artefact* from the power supply used (due to imperfect electrical control) and not the actual resistance of the sample. On the other hand, the overall trend of initially slow drop followed by dramatic drop in resistance shown in Figure 4.7 is consistent with the typical flash behavior. However, in this study the four-probe approach was not used to accurately measure the actual sample resistance due to complications that the sample was small and was enclosed in the multi-layer sample assembly. Further experiment as well as simulation will be carried out in future to enhance our understanding of the real resistance change in sample during RFS.

- *In situ synchrotron for RFS of TZN*

Figures 4.8(a) and (b) show 2D X-ray scans of the sample assembly containing the TiN-ZrN equimolar mixture before and after *in situ* RFS, respectively. It shows the sample (in dark blue due to low X-ray penetration) shrunk ~46% in thickness after RFS. In addition, selected integrated 1D diffraction patterns collected at representative time are plotted in Figures 4.8(c) and (d). At the very beginning, similar to conventional XRD in Figure 4.4, diffraction peaks for both TiN and ZrN were observed. In addition, about halfway between pure TiN and ZrN (111) peaks, there was a minor bump, labelled as (TiZr)N-1, at 9.59°. It is attributed to the solid solution between TiN and ZrN, most likely formed via mechanical alloying due to the short, but *intensive* Spex milling. From the beginning to ~150 s, as the voltage ramped up linearly, peaks for TiN and ZrN shifted gradually to lower angle due to thermal expansion. At 150 s, there was one minor peak labelled as (TiZr)N-2 and one bump labelled as (TiZr)N-3 between the (111) peaks for TiN and ZrN: (TiZr)N-2 represents a (Ti, Zr)N solid solution that is rich in Zr, while TiZr)N-3 represents a (Ti, Zr)N solid solution that is rich in Ti. From ~202 s, the peaks for TiN and ZrN largely disappeared, while the peaks for (TiZr)N-2 and (TiZr)N-3 became much stronger. The two remaining peaks gradually merged (see patterns from ~240 to ~332 s) to form a single phase solid solution, labelled as (TiZr)N-4, close to the target composition of $(Ti_{0.5}Zr_{0.5})N$ (see Figure 4.8(d) for detail). After cooling to room temperature, the solid solution experienced separation again into two phases: one Zr rich at lower angle and the other Ti rich at higher angle. It is noted that these peaks are shifted slightly to lower angle (representing slightly larger lattice parameter) compared with TiN and ZrN, probably due to partial replacement of nitrogen by carbon after ~410 s holding.

Figure 4.8(e) shows the change of lattice parameters of TiN, ZrN, and (Ti, Zr)N solid solution with time during *in situ* RFS. The first four strongest diffraction peaks ((111), (002), (220), (311)) were used for lattice parameter calculation. For both TiN and ZrN, consistent with expectation, their lattice parameters increased with time as the sample heated up. Using the literature average coefficient of thermal expansion (CTE) for ZrN of 7.8×10^{-6}/K [197], that the lattice parameter for ZrN expanded from 4.585 Å at ~0 s to 4.636 Å at 150 s would give an estimated temperature of ~1500°C for the sample at 150 s. Similarly, using average CTE of 9.35×10^{-6}/K for TiN [198], that the lattice parameter for TiN expands from 4.241 Å at ~0 s to 4.304 Å at 150 s would give an estimated temperature of ~1600°C. For (Ti, Zr)N, it is noted that the lattice parameter for only the final single phase solid solution after ~332 s was shown. This was due to the uncertain and changing composition for the multiple solid solutions (2 or more, see Figures 4.8(c) and (d)) that exist between ~150 and 332 s and the significantly reduced peak intensity. The reason for the continued lattice expansion for (Ti, Zr)N solid solution after ~332 s is not clear. It might be due to continued thermal expansion or partial replacement of nitrogen by carbon in the sample upon extended heating and further study is needed to verify this.

In theory, *in situ* synchrotron XRD should enable a decent measurement of the actual temperature during RFS. Unfortunately, in this study, precise temperature determination could *not* be achieved from experimental data. The above temperatures estimation from TiN and ZrN lattice parameters (~1500-1600°C at ~150 s) is *very rough* due to the lack of accurate CTE values over the *entire* temperature range. In addition, the nature and concentration for defects within the material, which may also influence lattice parameter, is unclear. Preliminary COMSOL simulations of temperature for both the standard RFS and *in situ* RFS had also been carried out, as shown in Figure S4. They show the expected trend such as the rise and drop in temperature under different configurations, but the exact values are of limited use due to the various assumptions made in the absence of reliable data about actual physical properties (e.g., electrical resistivity, thermal conductivity, emissivity) for the various materials/components and their junctions encountered in such a complex system. It should be mentioned that, previously, researchers have successfully performed accurate temperature measurement *during* flash sintering based on lattice parameters using *in situ* synchrotron. Those studies used the energy dispersive diffraction (EDD) technique and a small diffraction volume within the specimen could be selected and analyzed. In addition, platinum was also inserted into the specimen as a reference [199–204]. Further studies will be needed to check if and how similar techniques could be adopted in the current configuration for precise temperature measurement.

Nevertheless, the combination of standard *ex situ* XRD and the *in situ* synchrotron studies suggest that the formation of (Ti, Zr)N solution from TiN and ZrN at elevated temperature is an energetically favorable process that follows the phase diagram [184]. Note that phase separation was observed for the *in situ* TZN sample from the *in situ* synchrotron RFS experiment (see the two separate peaks at ~9-10 ° in Figure 4.8(c) RT after cooling), but a uniform solid solution was preserved in the std-TZN sample (Figure 4.4). Such a discrepancy is hypothesized to be related to the *cooling rate*: in the *in situ* synchrotron experiment, the sample might have reached higher temperature and cooled slower than the standard RFS experiment, which would allow adequate time for diffusion and phase separation of the (Ti, Zr)N solid solution into an equilibrium mixture of a Ti-rich and a Zr-rich phases. Further study is needed to verify this.

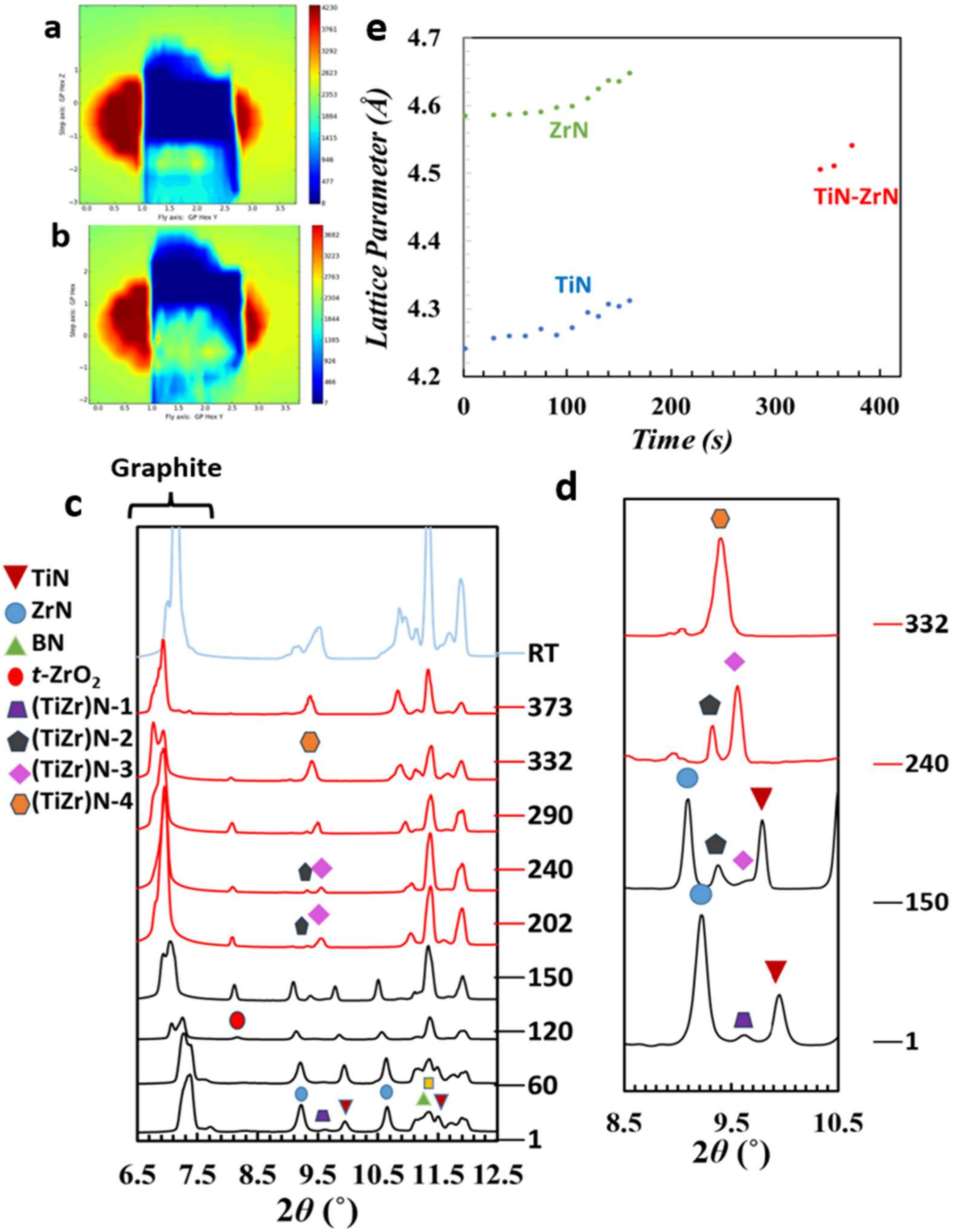

Figure 4. 8. (a and b) 2D X-ray scans of the flash sintering cell assembly loaded with TiN-ZrN equimolar mixture before (a) and after (b) in situ RFS. (c) Selected integrated 1D in situ synchrotron XRD patterns of the TiN-ZrN mixture during RFS. The numbers on the right show time in seconds after the beginning of the experiment. (TiZr)N-1 represents the solid solution formed in Spex milling; (TiZr)N-2 and (TiZr)N-3 correspond to solid solutions formed during the heating stage of the RFS; (TiZr)N-4 corresponds to the final single phase nitride solid solution. (d) Zoomed-in sections for selected patterns at different time showing gradual changes in the (111) peak for TiN, ZrN, and related (Ti, Zr)N solid solutions in the 2θ range of 8.5-10.5 degrees. Note the gradual disappearance of individual TiN and ZrN peaks and the appearance and merging of peaks for (Ti, Zr)N solid solutions. (e) Change in lattice parameter of the parent TiN and ZrN as well as the final single phase (Ti, Zr)N product with time during in situ RFS.

- *In situ synchrotron for RFS of TAN*

For the TiN-AlN system, Figures 4.9(a) and (b) show representative 2D X-ray scans collected before and after *in situ* RFS, while Figure 4.9(c) shows selected integrated 1D diffraction patterns collected at different times. Before ~120 s, the XRD patterns contain the peaks for *c*TiN, *h*AlN, as well as *c*AlN (from the nano AlN used for *in situ* RFS), and they largely remain the same due to negligible power dissipation in the incubation stage. Then, within a few seconds of the flash event (~120-125 s), a new set of peaks appeared to the left (lower angle) of TiN peaks.

The reason for the appearance of these new peaks is *not* clear. One possibility is non-uniform temperature distribution. But the difference in 2θ, e.g., 9.88˚ vs. 9.69˚ at 125 s, would mean a temperature difference of ~2100°C (again assuming CTE for TiN is 9.35×10^{-6}/K), which is too large to be practical within the 1.5 mm diameter sample.

Another possibility is synchrotron X-ray radiation hit the sample at different physical locations. However, it is also not convincing due to the *small focus* (~2×4 μm^2) of the synchrotron radiation compared with the mm-scale sample dimension.

A third possibility is the new peaks were from a new phase of Al-doped TiN. From unit cell volume point of view, this is *not* inconceivable because under ambient pressure, the most stable crystal structure for *h*AlN has a unit cell volume 40.878 Å^3 or 20.44 Å^3 per AlN formula at *room temperature*, while *c*TiN has a unit cell volume of 76.773 Å^3 or 19.20 Å^3 per TiN formula. Therefore, as a *first approximation*, for the pattern collected at 125 s, the peak at 9.88° would correspond to lattice parameter of 4.270 Å, while the peak at 9.69° would correspond to lattice parameter of 4.353 Å. The shift in 2θ of ~0.19° (from 9.88° to 9.69°) would correspond to a lattice parameter difference of 0.083 Å or ~1.9% increase from TiN, which is small compared with the lattice parameter difference in the TiN-ZrN system (i.e., 4.241 Å for TiN vs. 4.585 Å for ZrN, or 8.1% difference). In addition, as stated, for the synchrotron study, the starting AlN power did contain the metastable *c*AlN, which might make it easier for doping of Al into TiN.

However, it should be noted that the above third explanation appears to be *contradictory* to the literature showing *c*AlN as well as *c*$Ti_{1-x}Al_xN$ having lattice parameters *smaller* than TiN at *room temperature* [74, 179, 205]. Whether the contradiction could be explained by the temperature difference, i.e., room temperature for literature versus high temperature in the current *in situ* RFS study, remains to be studied.

Nevertheless, after the flash, as time progressed (see 150 s), the original TiN peaks gradually weakened and merged into the adjacent peak at lower angle (likely for Al-doped TiN), and the merged peak shifted to even lower angle, indicating continued lattice thermal expansion. When the system suddenly lost power at ~170 s (due to electrode mechanical failure), the Al-doped TiN peaks shifted back to higher angle (see 173 s vs. 150 s), representing lattice contraction due to cooling as well as possible phase separation (i.e., separation of Al nitride phase from the main TiN phase). After finally cooling to room temperature, the peaks were still to the left (or lower angle) of the TiN peak (e.g., (111) peak at 9.86° after RFS versus 9.92° before), probably representing residual Al still remain in the cubic TiN lattice.

Figure 4.9(d) shows the change of lattice volume for *c*TiN and *h*AlN with time during *in situ* RFS. (Lattice volume instead of lattice parameter used here since *h*AlN is not cubic) Consistent with Figures 4.3, 4.7, and 4.9(a-c), during the incubation (first ~120 s) *before* the flash, there was essentially no change in lattice volume for either *c*TiN or *h*AlN. After the flash, lattice volume for TiAlN, likely Al-doped TiN, displayed a sudden increase compared with pure *c*TiN, which was followed by a slow, continued increase, possibly due to thermal expansion. Upon sudden cooling (likely due to electrode failure) after ~170 s, the Al-doped TiN lattice parameter dropped due to shrinkage as well as possibly separation of *h*AlN.

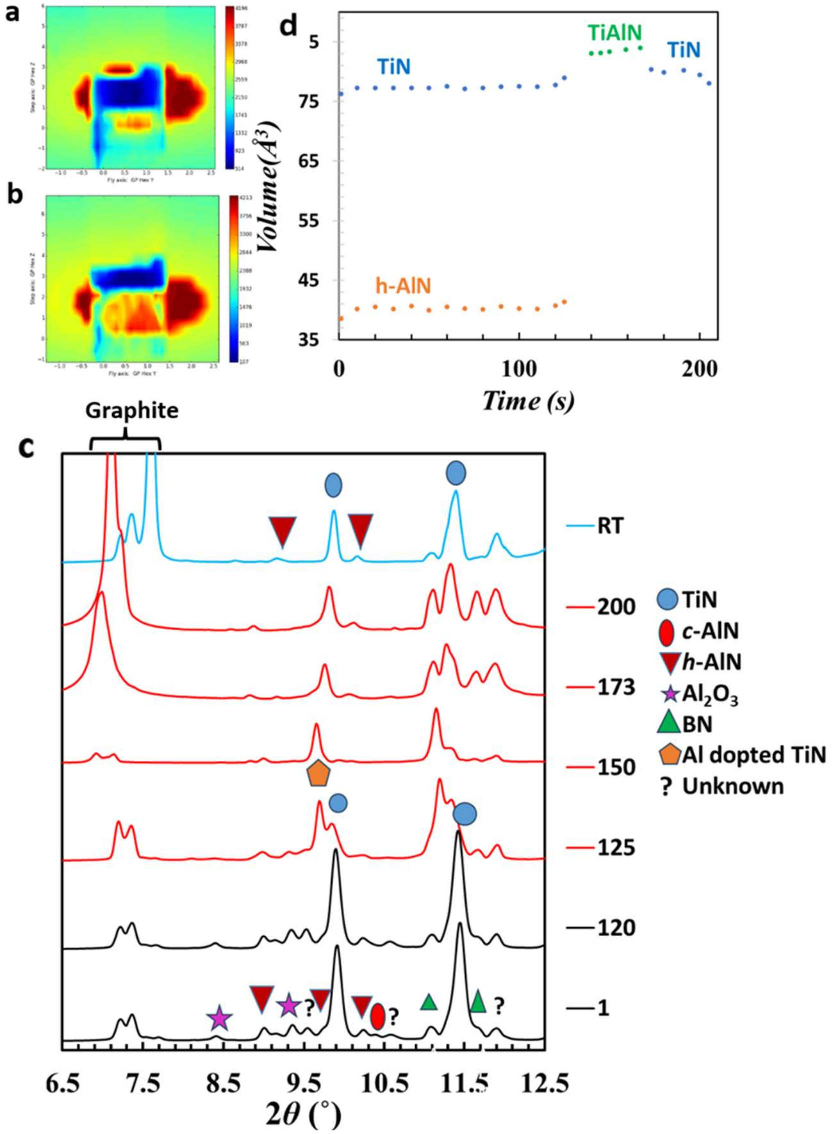

Figure 4. 9.(a and b) 2D X-ray scans of flash sintering cell assembly loaded with TiN-AlN equimolar mixture before (a) and after (b) in situ RFS. (c) Selected integrated 1D in situ synchrotron XRD patterns of the TiN-AlN mixture during in situ RFS in the 2θ range of 6.5 and 12.5 degrees. The numbers on the right show time in seconds after the beginning of the experiment. Note the appearance of peaks to the left of TiN from ~125 s, which are attributed to Al doped TiN. (d) Change in unit cell volume of TiN, *h*AlN, and TiAlN solid solution with time during RFS.

4.3.3. Microstructure of TiZrN and TiAlN from reaction flash sintering

Figures 4.10(a) and (b) show the SEM images for the fractured surface of an std-TZN sample. The relative density of the sample is ~94.0 % from dimension and weight, and the SEM images show the sample was indeed relatively dense with few pores. EDS showed that the Ti : Zr atom ratio in the reactive flash sintered pellet was 1 : 0.753 or 0.57 : 0.43, which was remarkably close to the ratio of 1 : 0.754 calculated by Vegard's' law from XRD-derived lattice parameters. The metal-to-nitrogen atom ratio could not be obtained reliably, due to instrument limitation of the EDS system. Nevertheless, the line scan image in Figure S5 shows the presence of all 3 elements, while EDS elemental mapping shows uniform distribution of Ti, Zr, and N, as in Figure 4.10(c).

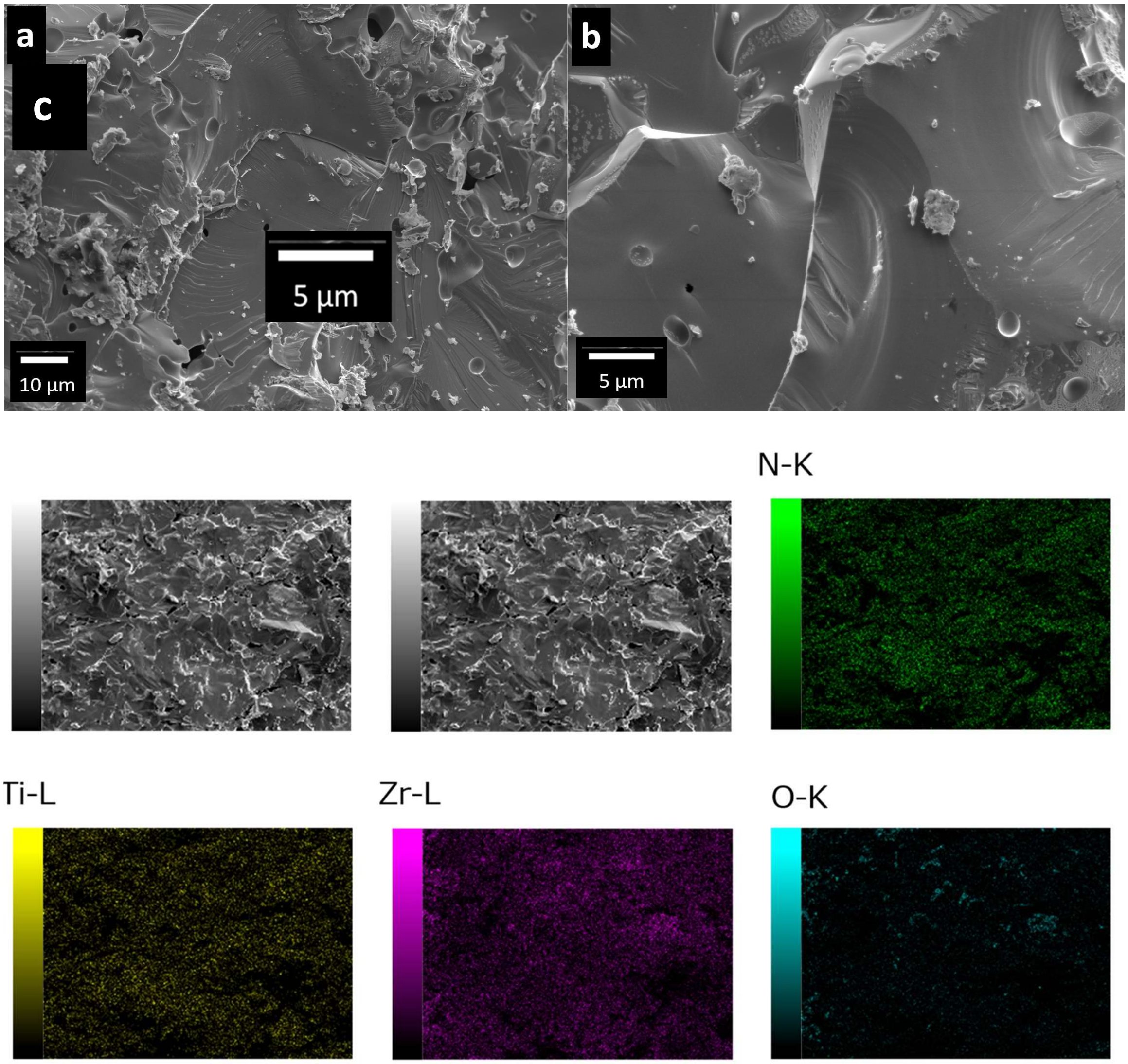

Figure 4. 10. (a and b) SEM images for a fractured surface of an std-TZN sample from standard RFS, (c) EDS elemental maps of the sample showing the uniform distribution of Ti, Zr, and N.

Figures 4.11(a) and (b) show the SEM images for the fractured surface of an std-TAN sample. Almost no pores are seen, which is consistent with a measured relative density of ~99.6%. EDS analysis shows that the Ti : Al atom ratio after RFS is 1: 1.002, which agrees with the starting equimolar TiN-AlN mixture. Figure 4.11(c) and Figure S6 show EDS mapping and line scan for the sample, respectively, which suggest relative uniform distribution of Ti and N, while Al was sometimes associated with presence of oxygen. This is explained as amorphous Al_2O_3 that might have formed during the cooling stage of RFS.

In comparison, Figures S7 and S8 show the SEM images of standard flash-sintered TiN (named std-TN) and ZrN (named std-ZN), respectively. After flash sintering, porosity for std-TN appeared higher than std-TZN, while std-ZrN was quite dense.

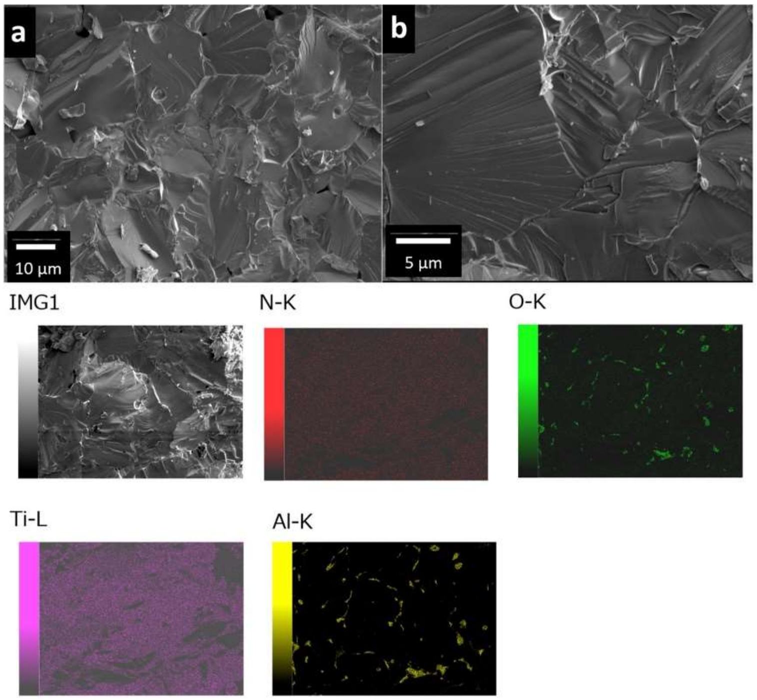

Figure 4. 11. (a-b) SEM images for the fractured surface of an std-TAN sample from standard RFS. (c) EDS elemental maps of the sample showing uniform distribution of Ti and N and the association of Al and O.

4.3.4. Properties of reactive flash sintered TiZrN and TiAlN samples

4.3.4.1. Oxidation resistance

As stated, the thermal oxidation resistance of std-TZN and std-TAN samples from standard RFS was evaluated by TGA-DSC from room temperature up to 1400˚C in the air with a heating rate of 5˚C/min and compared with similarly flash sintered TiN and ZrN. (Again, AlN was not flash sintered due to high resistivity). Figure 4.12 shows the TGA plot for fractured pieces of all four samples in air. For std-TZN, there was little weight gain before ~600˚C. The onset temperature for rapid oxidation was ~650˚C, while the corresponding exothermic peak was at 707˚C (see DSC curve in Figure S9). After that, there was a gradual weight gain till ~850˚C, followed by an even slower weight gain till ~1250˚C, and finally slight weight loss afterward. The weight gain upon oxidation was due to the formation of oxides from the nitride (solid solution), while the weight loss was attributed to the loss of lattice nitrogen from the sample. The total weight gain for the std-TZN sample is ~20.5%, matching reasonably with the theoretical weight gain of 21.5% for the complete oxidation reaction of

$$2Ti_{0.5}Zr_{0.5}N + 2O_2 \rightarrow TiO_2 + ZrO_2 + N_2 \qquad (1)$$

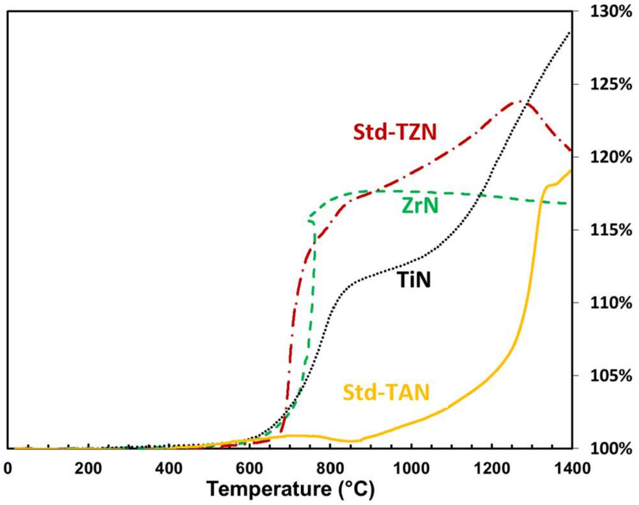

Figure 4. 12. Comparison of TGA plots for std-TZN and std-TAN samples from standard RFS with flash sintered binary nitrides of TiN and ZrN in air up to 1400 ˚C.

That the oxidation behavior for std-TZN is remarkably close to binary nitrides of TiN and ZrN without much delay indicates simply forming a random solid solution would *not* significantly improve the oxidation resistance for nitrides.

In comparison, the std-TAN sample from standard RFS showed significantly better oxidation resistance: There was little weight gain till at least ~850˚C. Rapid oxidation, as indicated by changing slope in the TGA plot was at ~1250ºC, while the exothermic peak occurred at a much higher temperature of ~1325˚C (see Figure S10). Despite the absence of a uniform solid solution, oxidation onset for TAN was delayed by at least ~200˚C compared to TiN. This is consistent with earlier studies on TiAlN thin films that form a protective Al_2O_3 oxide layer upon oxidation.

4.3.4.2. Mechanical properties

Mechanical properties such as Vickers micro-hardness were measured by indentation method for both the ternary metal nitrides from standard RFS and binary nitrides from standard flash sintering, and the results are also summarized in Table 4.1. Vickers hardness for the std-TZN sample was 10.5 ±1.7 GPa, despite its high relative density. Such a value is lower than that flash sintered ZrN giving a hardness value of 14.2±0.9 GPa, which is comparable to literature [6]. Hardness for flash-sintered TiN was rather low at 8.0±1.5 GPa, probably due to high porosity, since literature shows TiN hardness in the range ~18-25 GPa [6, 206]. The exact reason for the *absence* of solid solution hardening effect for bulk std-TZN sample from standard RFS is not clear: It might be related to nitrogen loss in high-temperature sintering, leading to more metallic behavior and lower hardness. In comparison, reactive flash sintered std-TAN gave a higher hardness of 17.8±1.2 GPa, possibly benefiting from phase separation of the high temperature (Ti, Al)N solid solution into fine, phase separated regions.

It should also be mentioned that the measured hardness for std-TZN and std-TAN were lower than reported values for TiZrN thin films (~17-24 GPa) [207] and TiAlN thin films (25-35 GPa) [66, 208]. This is probably due to the much larger grain size (> ~20 μm) for the samples after standard RFS comparing with submicron or even nano grained thin films.

Finally, fracture toughness K_{1c} was obtained following the method by Anstis and co-workers [209] from the formula $K_{1c} = 0.016 \left(\frac{E}{H}\right)^{0.5} \left(\frac{P}{c^{1.5}}\right)$ in units of MPa·m$^{1/2}$, where E is the elastic modulus (GPa), H is the hardness (GPa), P is the indentation load (N), and c is the crack length (m) (See supplemental Table S1 and S2 for E, H, P, and c values used). The measured K_{1c} values for standard (reactive) flash-sintered ternary (or binary) metal nitrides are listed in Table 4.1. K_{1c} for standard flash-sintered TiN and ZrN were 4.6±0.6 MPa·m$^{1/2}$ and 2.2±0.8 MPa·m$^{1/2}$, respectively, which are comparable to the literature [157, 210]. For std-TZN, K_{1c} was 5.1±2.0 MPa·m$^{1/2}$, while for std-TAN, it was 4.4±1.0 MPa·m$^{1/2}$.

4.4. Conclusions

Reactive flash sintering (RFS) of TiZrN and TiAlN using binary nitrides (i.e., TiN, ZrN, and AlN) as starting powders had been demonstrated for the first time. During standard RFS of TiZrN under constant voltage, the flash occurred instantaneously due to the high conductivity of both TiN and ZrN. Upon fast cooling, a bulk, single-phase (Ti, Zr)N solid solution was obtained, suggesting the formation of a uniform solid solution at elevated temperature. In comparison, for standard RFS of TiAlN, there was an obvious incubation before the flash due to the high resistivity of AlN in the starting powder mixture, but the flash was quick and dramatic. Upon cooling, unlike TiZrN, there was no obvious indication of (Ti, Al)N solid solution formation.

Preliminary *in situ* synchrotron experiments had also been carried out at the APS facility in ANL to monitor RFS in real-time. It captured the gradual formation of (Ti, Zr)N solution during *in situ* RFS, which, upon cooling, decomposed into two separate phases, all consistent with both the phase diagram and *ex situ* study. For the TiN-AlN system, *in situ* RFS seemed to suggest the formation of a single phase cubic (Ti, Al)N solid solution with lattice parameter *larger* than TiN formed at elevated temperature, and it decomposed very quickly back to *c*TiN and other minor, possibly amorphous, phases when heating was suddenly lost.

As to materials characterization, TiZrN and TiAlN from standard RFS were highly dense with relative density of ~94.0 % and ~99.6% respectively. Because TiZrN formed a single-phase solid solution after standard RFS, the distribution of Ti and Zr elements was uniform. For TiAlN, Ti and N were uniformly distributed while the association of Al with oxygen was observed. TGA-DSC revealed the onset oxidation temperature for TiZrN was comparable to TiN and ZrN, while it was higher by ~200°C for TiAlN. This indicates the formation of single-phase solid solution alone does *not* offer significant improvement in oxidation resistance, while the formation of Al_2O_3, even as separate phase, would benefit. Mechanical properties such as hardness and fracture toughness for both samples were also measured. It is noted that unlike thin films, bulk TiZrN did not show improved hardness over binary nitrides, which is hypothesized to be due to nitrogen loss upon high-temperature sintering, leading to more metallic behavior and lower hardness. The hardness for TiAlN was higher, presumably due to strengthening by phase separation from the solid solution. Overall, hardness for bulk ternary nitride from RFS was lower than reported for thin films, possibly due to their much larger (> ~20 μm) grain size, while fracture toughness for the ternary nitrides were comparable to parent binary nitrides.

Finally, it should be mentioned that much of the study was preliminary. For example, there had not been optimization of standard RFS, which might limit the performance of the obtained materials. Both *in situ* RFS experiment with real time synchrotron monitoring and simulation should also be improved based on the lessons learned, which would help verify the observations concerning phase transformation and determine the temperature more accurately. Further studies relating fine-scale microstructure analysis with mechanical properties is also needed to fully understand the effects of composition and the RFS parameters on materials properties for such bulk ternary metal nitrides.

Table 4. 1. Summary of standard RFS experiments including sample ID, the precursors used and their molar ratio, maximum current reached (all with initial 8 V DC), total time, products' final phase(s), relative density (from sample weight and dimension),properties such as oxidation onset temperature, fracture toughness, and Vickers hardness. For comparison purpose, the results for standard flash sintering of binary nitrides of TiN and ZrN, respectively, are also listed.

Sample ID	**Precursors**	**Molar Ratio**	**Max Current**	**Total Time**	**Major Phase(s)**	**Minor Phase(s)**	**Relative Density**	**Oxidation Onset Temp (˚C)**	**Total Weight Gain**	**Fracture Toughness (MPa·m$^{1/2}$)**	**Vickers Hardness (GPa)**
std-TN	TiN	-	193 A	350 s	*c*-TiN	-	86.7%	600	28.5%	4.6±0.6	8.0±1.5
std-ZN	ZrN	-	193 A	350 s	*c*-ZrN	*t*-ZrO_2	97.7%	625	16.8%	2.2±0.8	14.2±0.9
std-TZN	TiN+ZrN	1 : 1	200 A	350 s	*c*-$(Ti_{0.57}Zr_{0.43})N$	*t*-ZrO_2	94.0%[b]	650	20.5%	5.1±2.0	10.5±1.7
std-TAN	TiN+AlN[a]	1 : 1	200 A	400 s	*c*-TiN	TiO, $Ti_{0.9}Al_{0.1}C$	99.6%[c]	850	19.0%	4.4±1.0	17.8±1.2

[a] Micron AlN

[b] Theoretical density from PDF card: 04-015-1412 for $(Ti_{0.57}Zr_{0.43})N$

[c] Theoretical density of 4.27 g/cm^3 from Rule of Mixture for *c*TiN (PDF 04-002-1925) + *h*AlN (PDF 00-025-1133) equal molar mixture

4.5. Supplementary

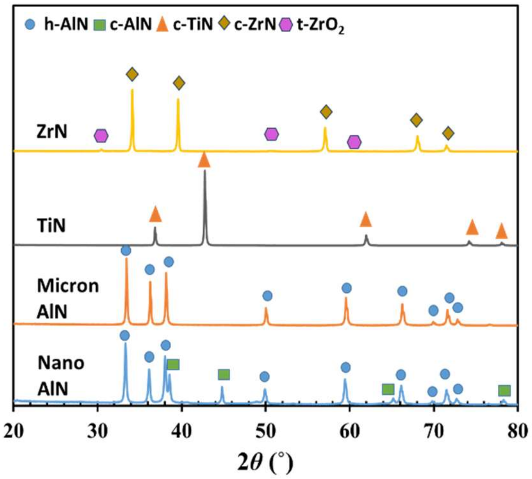

Figure S1 X-ray diffraction patterns of starting commercial binary nitride powders of ZrN, TiN, micron AlN, and nano AlN.

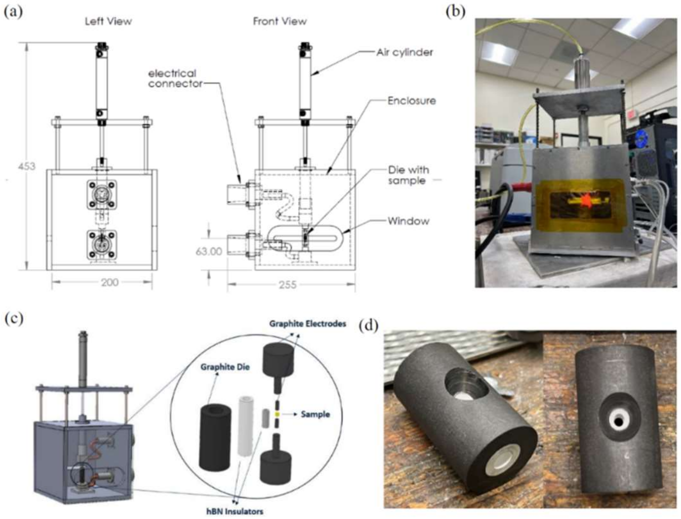

Figure S2 (a and b) Engineering drawing (a) and photo (b) of the newly designed *environmental chamber* for the (reaction) flash sintering process (including for the *in situ* synchrotron XRD study). (c and d) Schematics (c) and photos (d) showing the *sample assembly* that was used for *in situ* synchrotron RFS experiments. Note that, compared with the standard RFS sample assembly design (see [211]), side holes were opened through both the *h*-BN outer tube and the graphite outer sleeve to facilitate XRD penetration, while Kapton film was used to seal both sides of the environmental chamber to reduce air exposure while maintaining X-ray transparency.

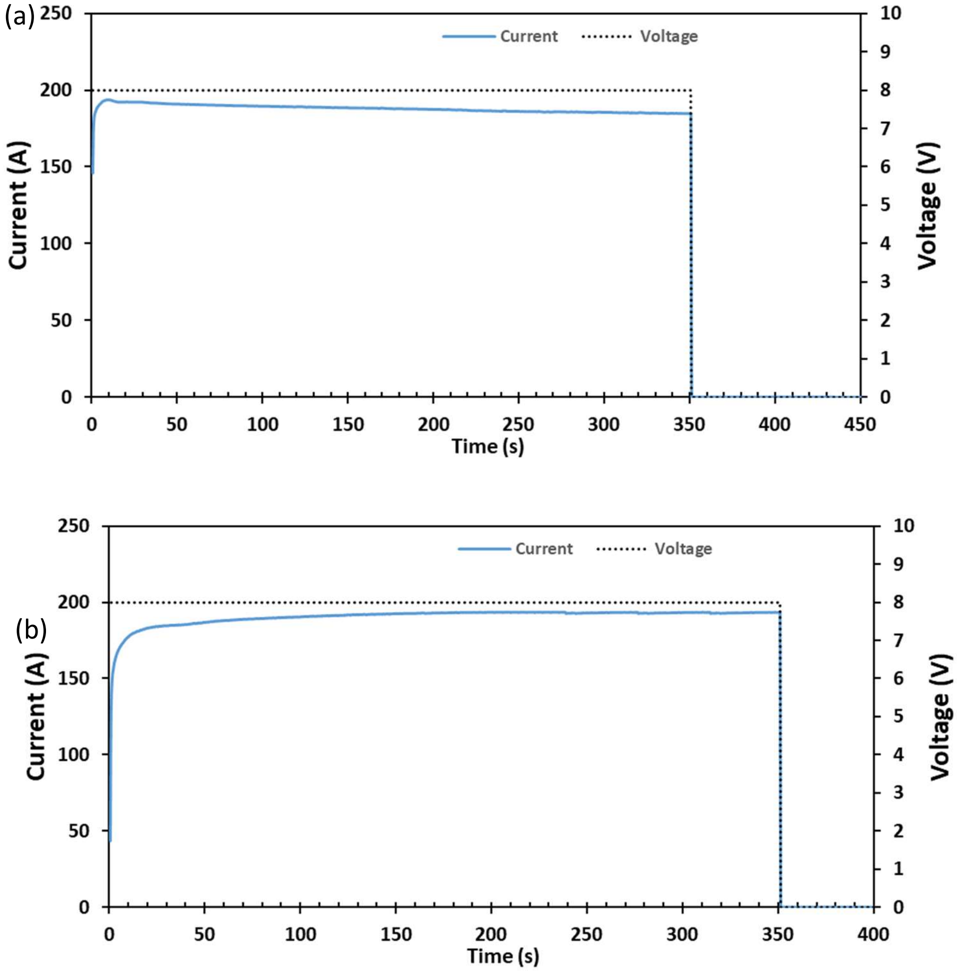

Figure S3 Plots of applied voltage and resulting current vs. time for standard flash sintering of the (a) std-TN (from TiN powder) sample and (b) the std-ZN (from ZrN powder) sample, respectively. Note in both cases, the power supply remained in the constant voltage mode and did *not* switch to constant current mode since the maximum current was 193 A (25.6 A/mm^2) - lower than the 200 A limit set before the experiment.

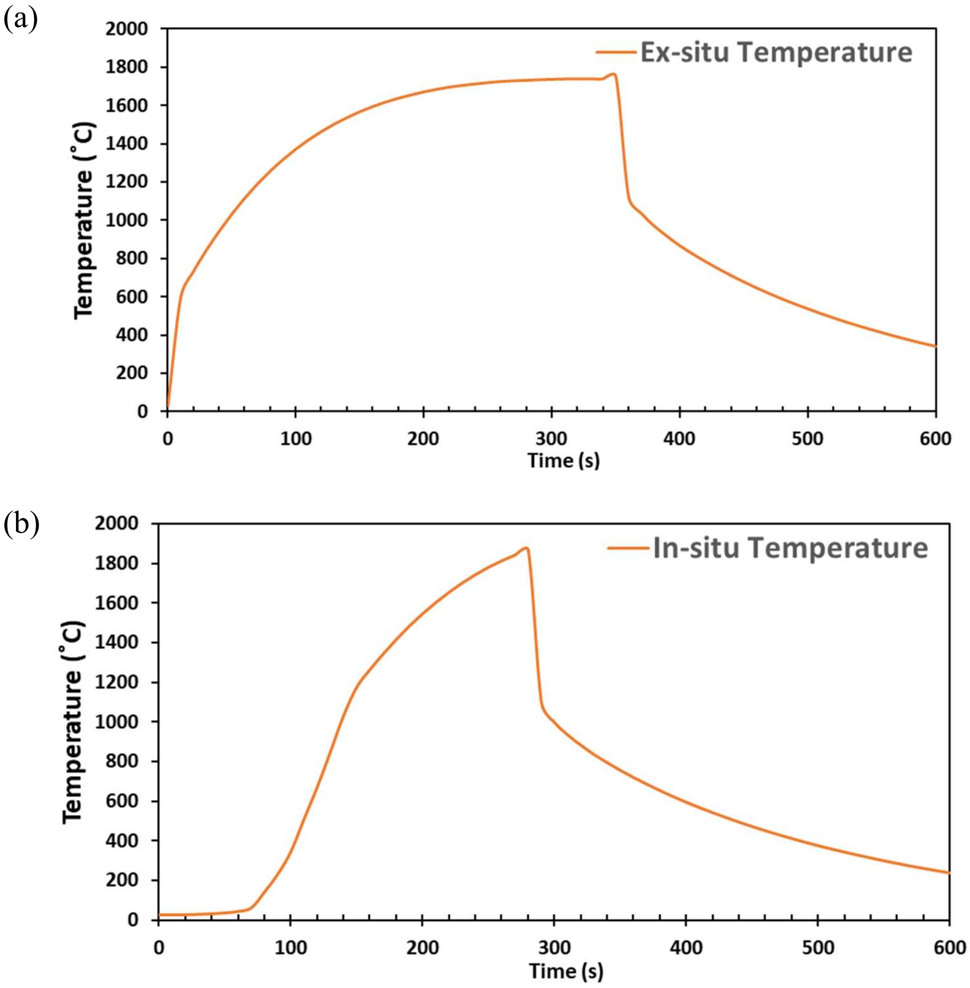

Figure S4 Plots of maximum sample temperature (at the sample center) vs. time from preliminary COMSOL® simulation for (a) standard *ex situ* RFS (3.1 mm diameter, constant 8 V DC) and (b) *in situ* RFS (1.5 mm diameter, ramping DC from 0 V at 0.1 V/s) for the TiN-ZrN system. Note although the trends appear reasonable, the exact temperature values are of very limited use due to the absence of reliable physical data for the various materials/components/contacts in the systems.

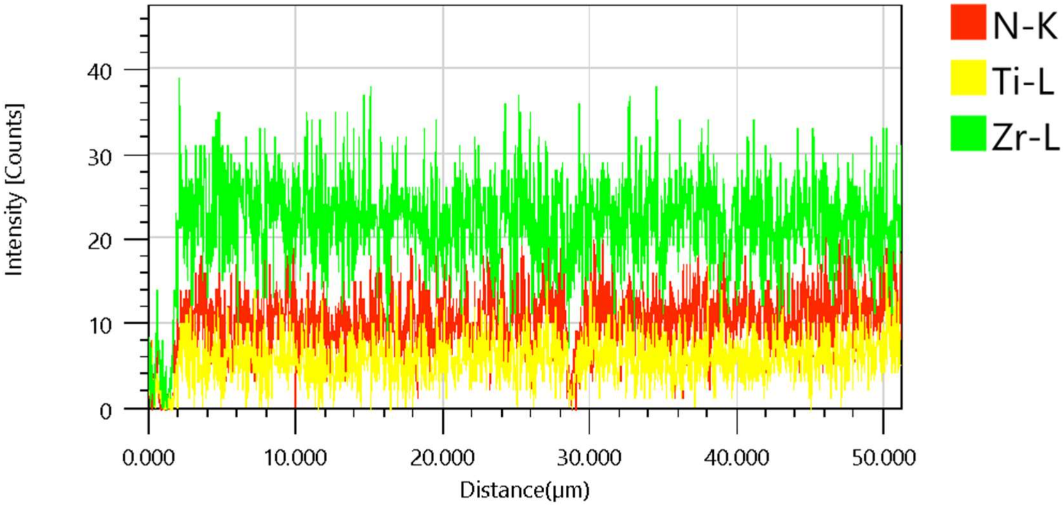

Figure S5 EDS line scan spectra of an std-TZN sample from standard RFS showing the uniform distribution of Ti, Zr, and N.

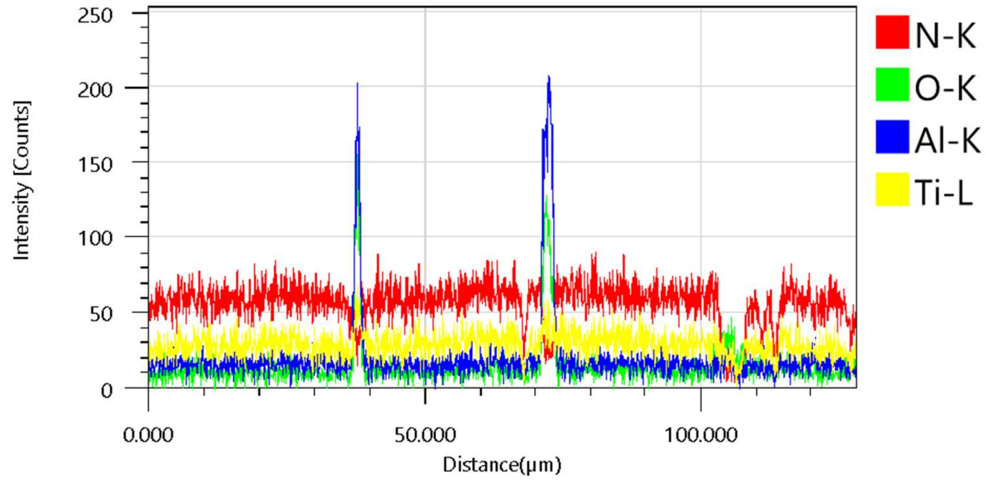

Figure S6 EDS line scan spectra of an std-TAN sample from standard RFS showing relative uniform distribution of Ti, Al, N as well as the occasional association of Al with O, representing local aluminum oxide impurity.

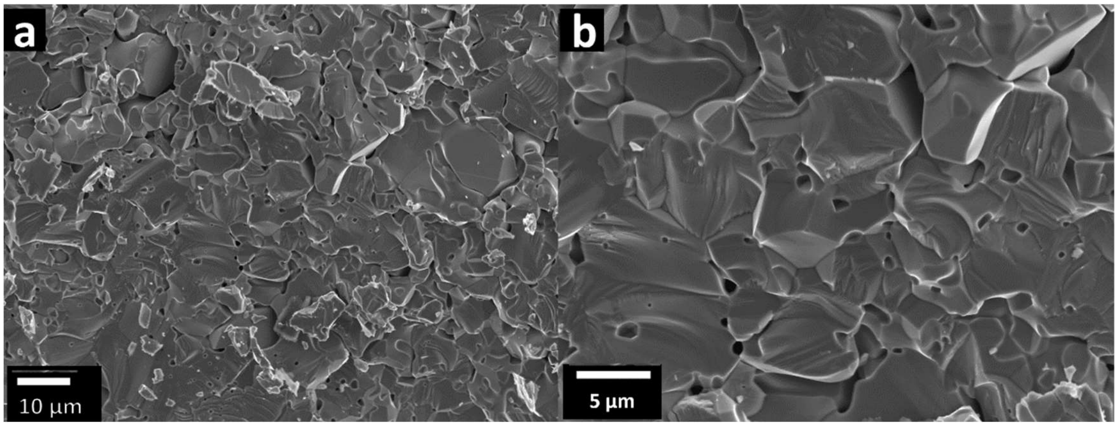

Figure S7 (a-b) SEM images for the fractured surface of an std-TN sample from standard flash sintering of TiN.

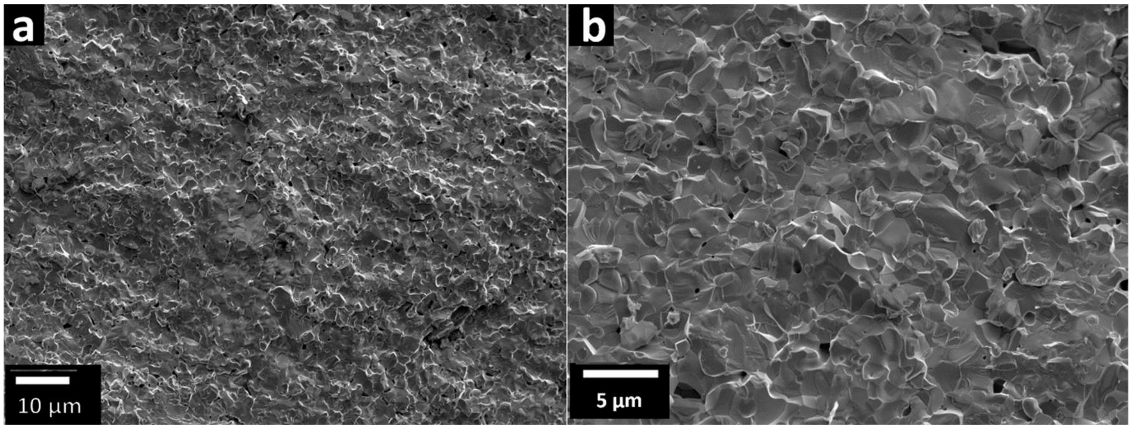

Figure S8 (a-b) SEM images the fractured surface an std-ZN sample from standard flash sintering of ZrN .

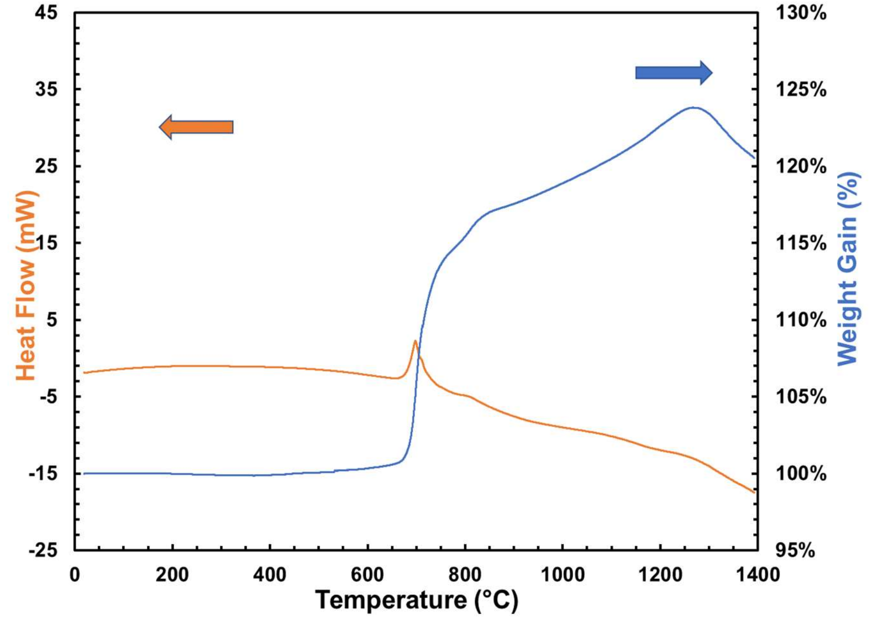

Figure S9 TGA-DSC plots of the std-TZN sample (TiN-ZrN equimolar mixture, standard RFS) in air up to 1400˚C.

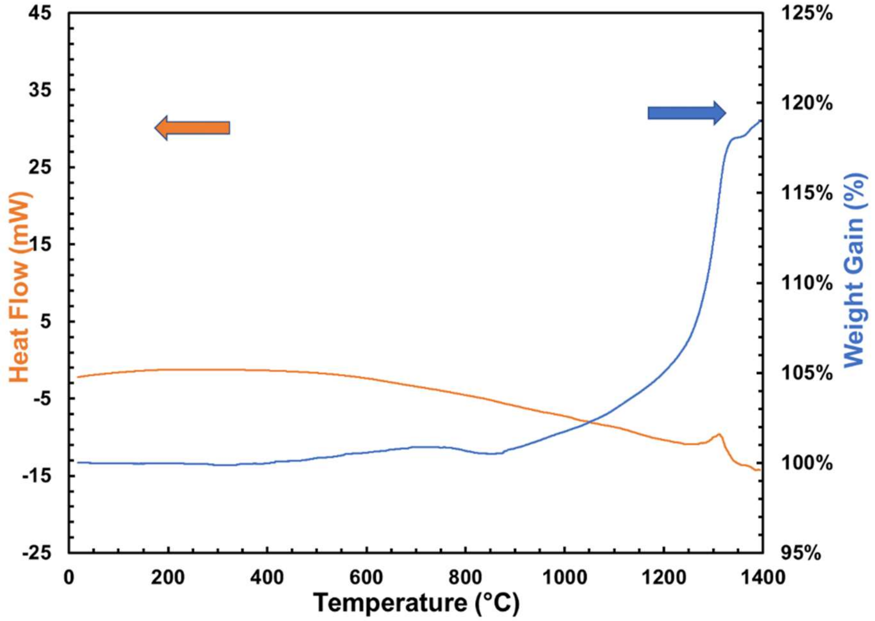

Figure S10 TGA& DSC plots of the std-TAN sample (TiN-AlN equimolar mixture, standard RFS) in air up to 1400˚C

Table S1 Values of elastic modulus E (GPa), hardness H (GPa), indentation load P (N), crack length c (m), and fracture toughness K_{1c} (MPa·m$^{1/2}$) for the std-TZN sample from standard RFS.

c (μm)	P (N)	E [a] (GPa)	H (GPa)	K_{1C} (MPa·m$^{1/2}$)
74.83	19.7	441.6	10.5	3.15
38.96				8.39
47.21				6.29
70.74				3.43
38.12				8.67
73.10				3.26
62.23				4.15
57.11				4.72
64.30				3.95

[a] E for *c*-TiN [212]and *c*-ZrN [213] from literature; E for TiZrN calculated from Rule of Mixture for equimolar mixture of *c*-TiN + *c*-ZrN

Table S2 Values of elastic modulus E (GPa), hardness H (GPa), indentation load P (N), crack length c (m), and fracture toughness K_{1c} (MPa·m$^{1/2}$) for the std-TAN sample from standard RFS.

c (μm)	P (N)	E^{b} (GPa)	H (GPa)	K_{1C} (MPa·m$^{1/2}$)
31.17	9.8	387.5	17.8	4.19
36.09				3.36
31.04				4.22
28.72				4.74
35.80				3.41
26.37				5.39
28.79				4.72
28.62				4.77
28.00				4.93
25.60				5.64
30.17				4.40
38.56				3.05
28.95				4.69
39.98				2.88
25.09				5.81
24.64				5.97
39.88				2.90

[b] E for *c*-TiN [212] and *h*-AlN [214] from literature; E for TiAlN calculated from Rule of Mixture for equimolar mixture of *c*-TiN + *h*-AlN

Chapter V: Reactive flash sintering and characterization of bulk high entropy nitrides

5.1. Introduction

In the past decade, research on high-entropy materials has sparked considerable interest and made significant progress. The concept of mixing multiple elements to create a cocktail of properties originated from high-entropy or multi-principle element *alloys* in 2004.[215216] Those alloys usually consist of five or more elements, and their configuration entropies when forming random solid solutions are >1.5R (where R is the gas constant). This unique combination led to many new stable alloys with enhanced mechanical properties and other desirable characteristics (e.g., superconductivity) [217–219].

The discovery of high-entropy effects in alloys inspired the development in other materials, especially ceramics [75–81]. High-entropy ceramics are ceramics that contain four or more metallic elements occupying the same *cation* site randomly. They may also have one or two nonmetal elements occupying the same anion site. Over the years, the range of high-entropy ceramics has expanded to include borides, carbides, nitrides, oxides, sulfides, and silicides [82–86].

Among high entropy ceramics, high entropy nitrides (HENs) are unique due to the nature of their bonding: not as ionic as oxides, but not as covalent as carbides or borides. The study on HENs actually started as early as 2004 on thin films such as (AlCrTaTiZr)N prepared by techniques such as reactive DC sputtering [220, 221]. The disorder in the cation sublattice of HENs leads to entropy stabilization, which allows the formation of single-phase solid solutions, often with an FCC crystal structure, while limiting intermetallics or binary nitrides formation. Such HENs, similar to high entropy alloys, [222] offer properties such as improved hardness and strength, due to severe lattice distortion [223]. In addition, that

HENs contain multi-principle elements means the composition space is quite large, which may result in properties beyond what is commonly expected and enable new applications beyond surface coatings for high temperature and environmental protection and diffusion barriers for the semiconductor industry [76, 82, 84, 91, 224, 225].

Up till recently, HENs have predominantly been synthesized as *thin films* using techniques such as plasma vapor deposition, vacuum arc deposition, and magnetron sputtering [95–98]. Various techniques, including modified mechanochemical synthesis [24], milling and combustion synthesis [91], soft urea method [106], and ammonia nitridation [107], have also been adopted to synthesize single-phase solid solution HENs *powders*. The first reports on *bulk* HEN came in 2018: Wen et al. used 6 h ball milling of binary nitrides followed by hot pressing at 1600 or 1800°C and 30 MPa for 60 min in vacuum to synthesize bulk $(Hf_{0.2}Nb_{0.2}Ta_{0.2}Ti_{0.2}Zr_{0.2})N$ [225]. Meanwhile, Dioppo et al. used spark plasma sintering (SPS) to synthesize (HfNbTaTiZr)N [92] at 2200°C for 1 h under 50 MPa [92]. Although the processes are effective, they still take hours long and consumes significant energy. Therefore, there is the need for novel facile synthesis of HEN, especially of new compositions.

The current research aims to demonstrate fast synthesis of bulk high entropy nitrides using a reactive flash sintering (RFS) approach. A range of HEN with nominal compositions such as $(Al_{0.2}Nb_{0.2}Ta_{0.2}Ti_{0.2}Zr_{0.2})N$, $(Al_{0.17}Nb_{0.17}Ta_{0.17}Ti_{0.32}Zr_{0.17})N$, $(Al_{0.20}Nb_{0.20}Ta_{0.20}Ti_{0.40})N$ and $(Al_{0.20}Nb_{0.20}Ti_{0.40}Zr_{0.20})N$ have been studied. The phase formation and evolution for RFS of these HEN were characterized through *ex situ* XRD and, for selected composition, *in situ* synchrotron during RFS. Microstructural and microchemical analysis was conducted using various techniques. Additionally, properties such as oxidation resistance, hardness and fracture toughness, high-pressure mechanical properties, and superconductivity for these bulk HENs are characterized. The relationship between the composition, microstructure, and properties of the HEN systems and the directions for future research are discussed.

5.2. Experimental Procedure

5.2.1. Raw materials and mechanical mixing

Commercial binary metal nitride powders were used for RFS of high entropy nitrides. The binary nitrides include aluminum nitride (nano powder <100 nm, Sigma Aldrich #593044), niobium nitride (Alfa Aeser #12146), tantalum nitride (99.5% metal basis, Alfa Aeser #13093), titanium nitride (99.5% metal basis, Alfa Aeser #41556), and zirconium nitride (99.5% metals basis excluding Hf, Hf<3%, Alfa Aeser #12138). XRD of commercial powders were performed to check for crystalline impurities. Commercial AlN contains h-AlN (86.3 wt.%) as well as aluminum metal impurity (13.7 wt.%); NbN and TiN are both cubic single-phase with no noticeable impurities; TaN contains hexagonal ε-TaN ($P\bar{6}2m$, 59.9 wt%) as well as δ-TaN ($P\bar{6}2m$, 40.1 wt.%), while ZrN contains ~4.1 wt.% of tetragonal ZrO_2 impurity (from Rietveld refinement).

The commercial powders were mixed according to designed compositions. Both equimolar and some slight Ti-rich compositions (for cost considerations) have been explored, targeting *nominal* compositions such as $(Al_{0.2}Nb_{0.2}Ta_{0.2}Ti_{0.2}Zr_{0.2})N$, $(Al_{0.17}Nb_{0.17}Ta_{0.17}Ti_{0.32}Zr_{0.17})N$, $(Al_{0.20}Nb_{0.20}Ta_{0.20}Ti_{0.40})N$, and $(Al_{0.20}Nb_{0.20}Ti_{0.40}Zr_{0.20})N$. The nitride powder mixtures (typically 1 g for each batch) were Spex-milled using SPEX Sample prep (8000D-115 Mixer/Mill) in a stainless-steel (SS) jar in air with a single SS ball for 5 mins before RFS to reduce particle size and ensure uniformity. XRD of the Spex-milled powder showed no contamination from the stainless-steel container.

5.2.2. Reactive flash sintering set-up

The setup for reactive flash sintering has been described previously [6, 211, 226, 227]. Typically, approximately 90 mg of precursor powder mixture is dry pressed at ~2400 MPa into a cylindrical pellet with ~3.1 mm diameter and ~1.5 mm thickness. A pellet is then inserted into a hexagonal boron nitride (*h*-BN) tube with two graphite electrodes contacting the two ends. To minimize sample oxidation and enable reuse of the graphite components, the entire sample assembly is placed inside a custom-built aluminum environmental chamber purged with argon gas (UHP grade, Airgas). RFS was carried out using a DC power supply (Hewlett Packard, 6671A, 8 V, 220 A). Pneumatic cylinder applied a pressure of ~15 MPa to maintain electrical contact. Water cooling is adopted to maintain the temperature for the copper terminals in contact with the graphite outer electrodes. After RFS, the system cools to ambient temperature and the sample is removed from the *h*-BN tube and separated from the graphite electrodes. The sample is ground to remove graphite residue attached to the surface, before being subjected to different analytical techniques for further characterization. The RFS parameters and final products' compositions for various samples are summarized in Table 5.1.

5.2.3. Materials characterization

X-ray diffraction patterns were obtained on powders ground from the RFS pellets using a Smart Lab SE X-ray diffractometer with Cu-Kα radiation (λ = 1.54059 Å for $K_{\alpha 1}$). To examine the microstructure and elemental distribution of the RFS pellets, a scanning electron microscope (SEM, JEOL JSM-F100) fitted with energy-dispersive X-ray spectroscopy (EDS) was used. High-angle annular dark-field (HAADF) scanning transmission electron microscopy (STEM) and EDS elementary mapping images were recorded using a Hitachi HD2700 aberration-corrected STEM machine. Oxidation resistance for bulk RFS samples were evaluated by thermogravimetric analysis-differential scanning calorimetry (TGA-DSC) using a TA Instrument SDT Q600 on fragments of RFS pellets between ~25 and 1400°C in flowing air with a heating rate of 5°C/min.

For mechanical properties, the RFS pellets were mounted in resin, ground, and polished down to 0.1 μm polycrystalline diamond slurry. Vickers hardness and fracture toughness of the samples were measured using LECO LM810AT (LECO Corporation). A diamond tip with a 2000 gf (19.8 N) load was used to make indentations on the surface along a 3.1 mm diameter to ensure accurate and representative results. Fracture toughness was determined by following the ASTM approved method by Anstis and co-workers from the formula $K_{1c} = 0.016\,(\frac{E}{H})^{0.5}(\frac{P}{c^{1.5}})$ in units of MPa·m$^{1/2}$, where E is the elastic modulus (GPa), H is the hardness (GPa), P is the indentation load (N) and c is the average crack length (m) originated from indentation measured using SEM.

Apart from conventional characterizations, synchrotron based XRD was utilized in this study to better comprehend the changes in composition, crystal structure, and lattice constants of the phases that took place *during* RFS to synthesize high entropy nitrides. The synchrotron angle-dispersive XRD tests were conducted at sector 16-ID-B, HPCAT, of the Advanced Photon Source (APS) in Argonne National Laboratory (ANL). The experiments involved both *in situ* and *ex situ* characterization, and their specifics are provided below. To accommodate the *in situ* synchrotron XRD measurements, similar to previous study [227], adjustments were made to the flash sintering sample assembly to allow for X-ray penetration. The environmental chamber was placed on the general-purpose table of beamline 16-ID-B at the APS synchrotron facilities as shown in our previous study [227]. The openings for the aluminum RFS environment chamber were sealed with X-ray transparent high-temperature resistant polymer (Kapton®) film. The sample diameter was decreased from 3.1 mm in the standard RFS design to 1.5 mm (samples height ~2 mm) to allow the incident X-ray and the diffracted beam to pass through the sample. All *in situ* synchrotron RFS tests employed a separate DC power source (Hewlett Packard, 6031A, 20 V, 120 A). Monochromatic X-ray synchrotron radiation with a wavelength λ = 0.424590Å was used, and the X-ray focus area was 2 μm x 4 μm. To gather the 2D diffraction pattern, a high-frequency area PILATUS 1M detector with a minimum acquire period of 8 ms was used. XRD patterns were captured every second during the *in situ* synchrotron investigation of RFS for HEN targeting $(Al_{0.17}Nb_{0.17}Ta_{0.17}Ti_{0.32}Zr_{0.17})N$.

High-pressure angle dispersive XRD studies were also carried out using the same synchrotron radiation. Symmetrical diamond anvil cells (DAC) with diamond anvils of a culet size of 300 μm were used to generate pressure. The sample was loaded into a 70 μm hole in a stainless-steel gasket (TS302) pre-indented to a thickness of 50 μm, along with a small ruby chip at the center of the sample chamber. Pressures were calculated using the ruby (R1) fluorescence method. Silicone oil (Sigma–Aldrich) with a viscosity of 1000 cP was used as the pressure-transmitting medium. The pressure was increased incrementally at room temperature up to 35.6 GPa, and XRD patterns from the sample were collected at every step during compression. The collected 2D diffraction images were integrated using Dioptas software.

Finally, magnetic property was conducted using a Superconducting Quantum Interference Device (SQUID, Quantum Design), while electrical transport properties were measured using a four-probe method in a Physical Property Measurement System (PPMS, Quantum Design), down to 2 K, as achieved by liquid helium.

5.3. Results and discussions:

5.3.1. RFS of HENs

Figure 5.1 illustrates the changes in current over time during RFS of HEN $(Al_{0.17}Nb_{0.17}Ta_{0.17}Ti_{0.32}Zr_{0.17})N$. As stated, a constant 8 V DC and 15 MPa were applied, and the entire RFS experiment lasted for 350 s. Except for AlN (near insulating with conductivity of ~ 5×10^{-12} S/cm at room temperature [214]), all other starting binary nitrides in the mixture were conducting, with room temperature conductivity of ~17,000 S/cm for NbN [228], ~ 8000 S/cm for TaN [228], ~ 37000 S/cm for TiN [195], and ~ 20000 S/cm for ZrN [196]. As soon as 8 V DC was applied, the flash occurred immediately: at 0.57 s, the current was already ~ 25 A, corresponding to a current density j of 3.26 A/mm^2 and power dissipation of 196 W. The current further increased to 140 A (18.53 A/mm^2) at 1 s and 170 A (22.51 A/mm^2) at 3 s. Subsequently, the current continued to increase at a slower rate until reaching its maximum value of 191 A at ~350 s, corresponding to j of 25.26 A/mm^2 and a system peak power of 1525 W. Finally, the power supply was turned off, and the entire setup was allowed to cool to room temperature.

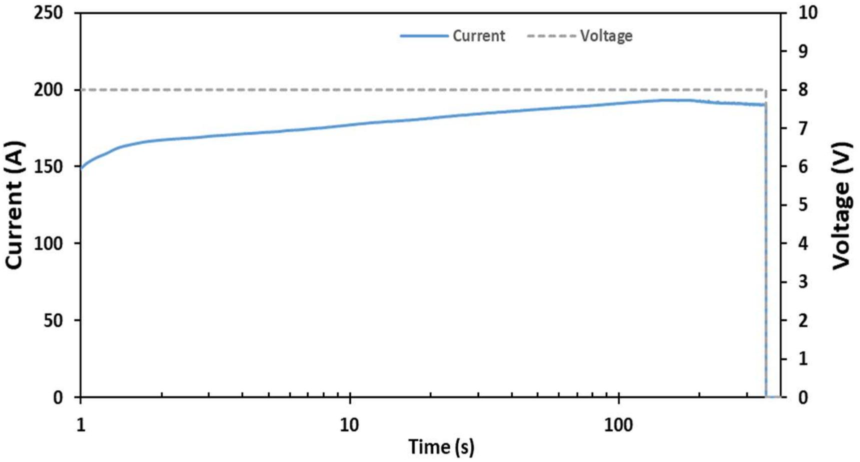

Figure 5. 1. Plot of applied voltage (dotted line) and resulting current (solid line) vs. time for reactive flash sintering of HEN with nominal composition of $(Al_{0.17}Nb_{0.17}Ta_{0.17}Ti_{0.32}Zr_{0.17})N$ from non-equimolar binary nitride powder mixture.

In addition to $(Al_{0.17}Nb_{0.17}Ta_{0.17}Ti_{0.32}Zr_{0.17})N$, RFS was also performed on other high entropy compositions such as $(Al_{0.20}Nb_{0.20}Ta_{0.20}Ti_{0.40})N$ and $(Al_{0.20}Nb_{0.20}Ti_{0.40}Zr_{0.20})N$ using the same parameters and the resulting current-time plots are shown in supplemental Figure S1. For $(Al_{0.20}Nb_{0.20}Ta_{0.20}Ti_{0.40})N$ and $(Al_{0.20}Nb_{0.20}Ti_{0.40}Zr_{0.20})N$, the maximum current was lower at 147 A (19.4 A/mm^2) and 135 A (17.8 A/mm^2), respectively, which are significantly *lower* than for $(Al_{0.17}Nb_{0.17}Ta_{0.17}Ti_{0.32}Zr_{0.17})N$. The lower current might be related to presence of higher concentration of insulating AlN (20 at.% or 25 vol.% in the Ti-rich, 4-metal HEN versus the 17 at.% or 19 vol.% for the Ti-rich 5-metal HEN).

In addition to HENs, four of the starting conductive binary nitrides, NbN, TaN, TiN and ZrN, were also flash sintered under the same conditions (i.e., initial 8 V DC, 15 MPa pressure, 350 s total time). For AlN, due to its insulating property, it could *not* be flash sintered even after pre-heating (up to ~200 ºC). The flash sintering behavior observed for NbN, TaN, TiN, and ZrN is similar to that for $(Al_{0.17}Nb_{0.17}Ta_{0.17}Ti_{0.32}Zr_{0.17})N$, (see Figure S2).

5.3.2. Solid-solution formation during RFS of HEN

5.3.2.1. Characterization by *ex situ* XRD

Figures 5.2. depicts the XRD patterns of the HEN sample with nominal composition of $(Al_{0.17}Nb_{0.17}Ta_{0.17}Ti_{0.32}Zr_{0.17})N$ before and after RFS. Before RFS, the Spex-milled sample consisted of a mixture of *c*-AlN, *c*-NbN, *h*-TaN (ε phase), *c*-TiN, and *c*-ZrN, with trace amounts of *t*-ZrO_2 impurities. Following RFS, the sample transformed into a *near-single-phase* nitride solid solution, exhibiting no distinct peak splitting. The diffraction pattern corresponded to a cubic, NaCl-type crystal structure, with a calculated lattice parameter of 4.364 ± 0.0005 Å. The insert in Figure 5.2. displays the positions of HEN peak (111) as well as binary nitrides of AlN (PDF Card: 00-046-1200), NbN (PDF Card: 04-004-2895), TaN (PDF Card: 00-039-1485), TiN (PDF Card:04-002-1925) and ZrN (PDF Card: 04-004-2860). After RFS, minor impurities of *t*-ZrO_2 (PDF card: 00-081-1546), *o*-TiO_2 (PDF card: 00-049-1433), and *c*-(Ta, Nb)(C, N) (PDF card: 04-001-4538) were also detected, with some such as *t*-ZrO_2 presumably coming from impurities existing in the commercial nitride powders. The sample after RFS also revealed the presence of graphite (PDF card: 04-014-0362), which is attributed to contamination from residual of the graphite electrodes utilized. The XRD result confirmed the presence of a single-phase region at elevated temperature for the $(Al_{0.17}Nb_{0.17}Ta_{0.17}Ti_{0.32}Zr_{0.17})N$ system, while rapid cooling in the current RFS setup preserves the bulk single-phase solid solution to room temperature.

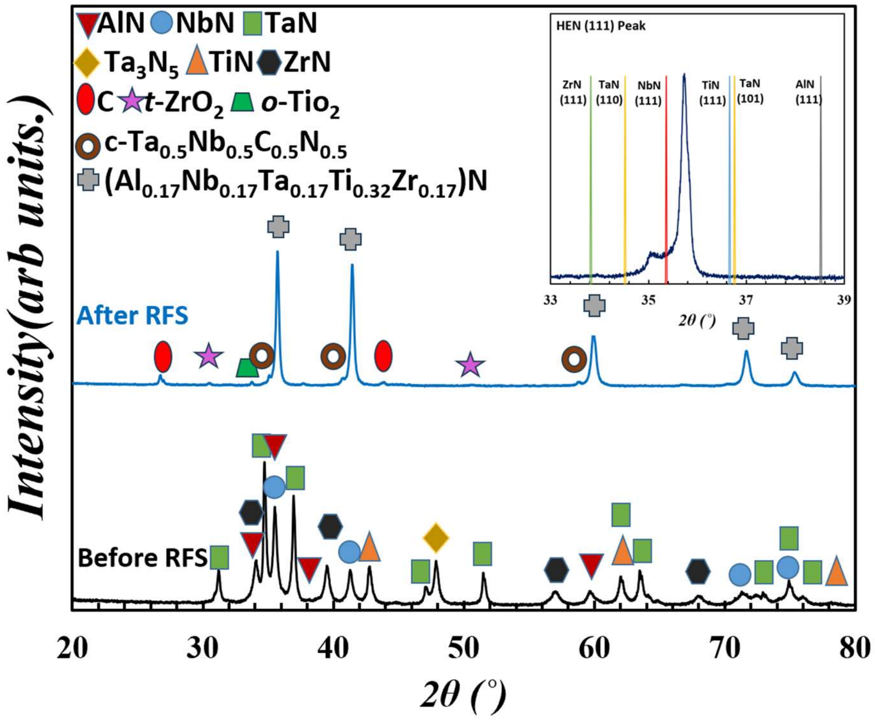

Figure 5. 2. XRD patterns of the (Al0.17Nb0.17Ta0.17Ti0.32Zr0.17)N sample before and after standard RFS. The sample transformed from a mixture of binary nitrides to a cubic, NaCl structured solid solution with minor impurities after RFS. The insert is the zoomed-in section showing the (111) diffraction peak, and the expected positions for (111) peaks of pure *h*-AlN, *c*-NbN, *h*-TaN, *c*-TiN and *c*-ZrN are also marked.

Similarly, supplementary Figures S3 and S4 display the XRD patterns of $(Al_{0.20}Nb_{0.20}Ta_{0.20}Ti_{0.40})N$ and $(Al_{0.20}Nb_{0.20}Ti_{0.40}Zr_{0.20})N$ samples before and after RFS. Both, like $(Al_{0.17}Nb_{0.17}Ta_{0.17}Ti_{0.32}Zr_{0.17})N$, form a near-single-phase NaCl-structured solid solution after RFS. For $(Al_{0.20}Nb_{0.20}Ta_{0.20}Ti_{0.40})N$, the lattice parameter for the HEN phase is 4.329 ± 0.0002 Å, while the minor impurities are *o*-TiO_2 and *c*-$(Ta_{0.5}Nb_{0.5})(C_{0.5}N_{0.5})$. For $(Al_{0.20}Nb_{0.20}Ti_{0.40}Zr_{0.20})N$, the lattice parameter was 4.381 ± 0.001 Å, while the minor impurities are *t*-ZrO_2, *o*-TiO_2, *c*-$Al_3(O_3N)$ (PDF card: 01-077-9858), and *o*-Al_2O_3 (PDF card: 04-012-6907). Graphite contamination was also present in both samples after RFS.

5.3.2.2. Characterization by *in situ* synchrotron XRD

Along with *ex situ* XRD, *in situ* synchrotron X-ray diffraction (XRD) was also performed during RFS for HEN of $(Al_{0.17}Nb_{0.17}Ta_{0.17}Ti_{0.32}Zr_{0.17})N$ at APS, and the results are presented in this section. To the best of the authors' knowledge, this is the first ever real-time study of phase transformation and solid solution formation for high entropy nitrides during *in situ* RFS.

- *Electrical characteristics of in situ RFS*

The experimental setup for *in situ* RFS that enables real time synchrotron study has been described before (see experimental and previous report [227]). Notably, the sample diameter was only 1.5 mm for better penetration of incident and diffracted X-ray. Instead of starting from pre-compacted green pellets, loose powder mixture was directly loaded into the sample assembly. The DC voltage was ramped up linearly from 0 V at 0.2 V/s and the current limit was set at 90 A.

The electrical characteristics, including voltage, current, total power, and total resistance, versus time during the *in situ* RFS experiment for $(Al_{0.17}Nb_{0.17}Ta_{0.17}Ti_{0.32}Zr_{0.17})N$ are depicted in Figure 5.3. In this case, contrary to standard RFS under constant 8 V DC, there was an obvious incubation stage: As the voltage linearly increased from 0 V at 0 s to 8 V at 40 s, current increased slowly from 0 A to 1.05 A. Between 40 and 55 s, voltage increased from 8 to 11 V, while current increase accelerated slightly from 1.05 A (0.59 A/mm^2) to 3.15 A (1.78 A/mm^2). Then, the flash occurred: Within ~5 s, current increased by more than almost 20 times to ~58 A (33.8 A/mm^2) at 60 s while the applied DC voltage only increased by 1 V (or 9.1%) to 12 V. Afterwards, as voltage increased further, current continued to increase, reaching 85.44 A with 14.82 V at 75 s. Finally, the power was turned off at 258 s.

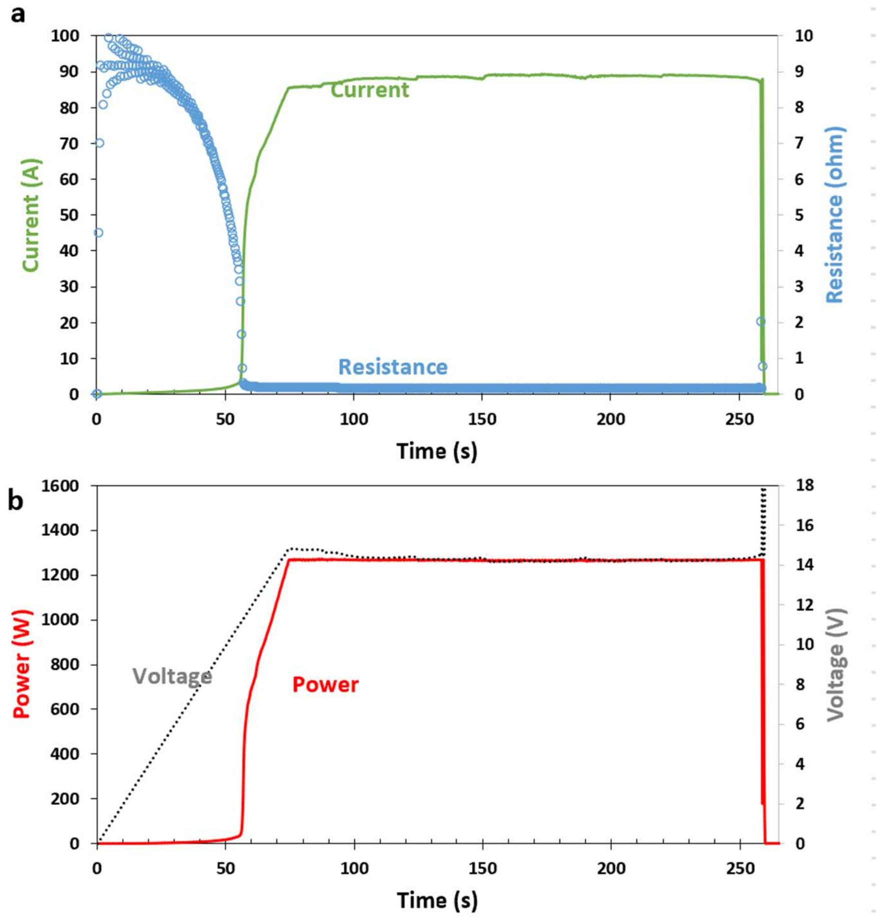

Figure 5. 3. Plots of (a) voltage and power versus time and (b) current and total resistance versus time for the in situ RFS of $(Al_{0.17}Nb_{0.17}Ta_{0.17}Ti_{0.32}Zr_{0.17})N$ sample monitored in real time by synchrotron at the APS facility in ANL. The voltage was linearly ramped up from 0 V at a rate of 0.2 V/s up to 14.7 V, while the power spiked up non-linearly from ~55 s, reaching the max power of ~1.3 kW with a max current of ~85 A (48 A/mm^2) at ~80 s, and then stabilized.

- *In situ synchrotron for RFS of HEN*

Figure 5.4 shows selected integrated 1D diffraction patterns in the 2θ range of 10 to 13^o collected at different time during the *in situ* RFS experiment of HEN $(Al_{0.17}Nb_{0.17}Ta_{0.17}Ti_{0.32}Zr_{0.17})N$. At the very beginning such as 1 s with 0.2 V DC and a low current of 0.03 A (0.017 A/mm^2), similar to conventional XRD in Figure 5.2, diffraction peaks for *h*-AlN, *c*-NbN, *h*-TaN, *c*-TiN and *c*-ZrN are observed. As 30 s (6 V, 0.72 A or 0.41 A/mm^2), the pattern appears similar, with the (200) peaks for binary nitride such as ZrN (10.64 °) and TiN (11.33 °) stay at roughly the same position as before, but the relative intensity becomes weaker. Meanwhile, there was a new shoulder arises at 11.27 ° between the peak of *c*-NbN and *c*-TiN, possibly due to a new solid solution with composition between the binary nitrides. There is another major peak at 11.9 °, which is attributed to *h*-BN. Then, as stated, the flash occurred between ~55-60 s and the corresponding XRD at 58 s shows a strong peak at 11.37 °, which is attributed to major HEN single phase solid solution. Meanwhile, the peaks for NbN, TaN, TiN, and ZrN became much weaker. At ~75 s, the peaks for AlN, NbN, TaN, TiN, and ZrN all largely disappeared, while the peak for HEN became sharper and stronger. The experiment lasted 258 s. After cooling to room temperature (RT), the major HEN peak is still dominating.

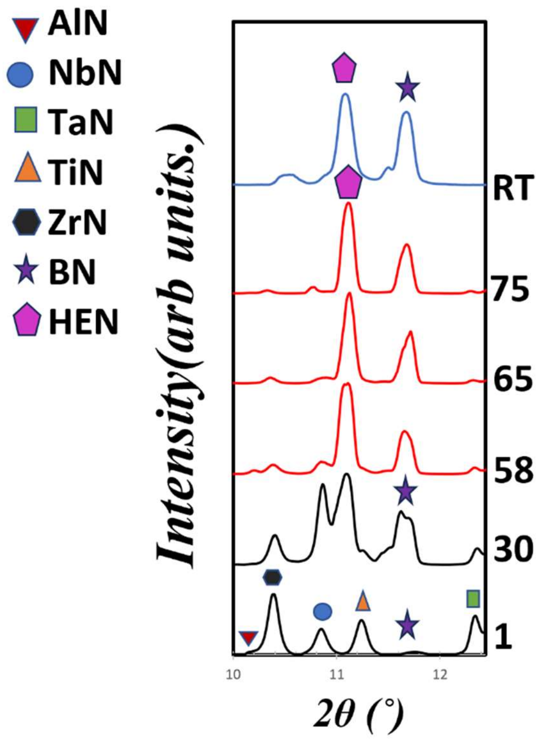

Figure 5. 4. Selected integrated 1D insitu synchrotron XRD patterns of the $(Al_{0.17}Nb_{0.17}Ta_{0.17}Ti_{0.32}Zr_{0.17})N$ during RFS (note the synchrotron radiation has wavelength of 0.4246 Å). The numbers on the right show time in seconds after the beginning of the experiment.

Both *ex situ* XRD and *in situ* synchrotron studies suggest that the formation of $(Al_{0.17}Nb_{0.17}Ta_{0.17}Ti_{0.32}Zr_{0.17})N$ solid solution from binary nitrides of AlN, NbN, TaN, TiN and ZrN at elevated temperature is an energetically favorable process. Moreover, the uniform solid solution is stable and is preserved at room temperature.

5.3.3. Microstructure analysis

Figures 5.5 (a) and (b) show SEM images of the fractured surfaces of $(Al_{0.17}Nb_{0.17}Ta_{0.17}Ti_{0.32}Zr_{0.17})N$ high entropy nitride synthesized by reactive flash sintering. The sample is dense with low porosity, which is consistent with the sample's relative density of ~96.2% determined from dimension and weight (sample too small for reliable Archimedes measurement). The fractured surface displays closely spaced layered structures, which resembling numerous slip lines, and it was reproduced over multiple samples. Such a layered structure is akin to those in certain hexagonal carbides and nitrides with layered structures such as $M_{n+1}AX_n$ phases [229]. The exact reason for the layered structure in HEN is unclear, but it is postulated to differ from that for MAX phases due to the differences in crystal structure: cubic for the HENs in this study versus hexagonal layered structure in MAX phases. Figure 5.5 (c) and (d) displays the SEM images of the cross-section of fractured surface for RFS $(Al_{0.20}Nb_{0.20}Ta_{0.20}Ti_{0.40})N$ and $(Al_{0.20}Nb_{0.20}Ti_{0.40}Zr_{0.20})N$, respectively. Comparing to $(Al_{0.17}Nb_{0.17}Ta_{0.17}Ti_{0.32}Zr_{0.17})N$, both HEN samples appear to have slightly more pores after RFS, but the layered structure was again observed.

SEM for flash-sintered (similar voltage/pressure as HENs) parent binary nitrides (e.g., NbN, TaN, TiN, and ZrN) are given in supplemental Figure S5. The porosity was slightly higher than that of the HENs, indicating less densification. The layered structure observed in HENs was not found in any of the binary nitrides, suggesting that the layered structure observed might be due to the composition and, possibly, the high entropy effect.

EDS analysis indicates that the atom ratio of Al : Nb : Ta : Ti : Zr in the reactive flash sintered pellet was 0.41 : 0.47 : 0.45 : 1 : 0.47 (corresponding to a stoichiometry of $(Al_{0.15}Nb_{0.17}Ta_{0.16}Ti_{0.36}Zr_{0.17})N$), which was reasonably close to the starting nominal ratio of 0.53 : 0.53 : 0.53 : 1 : 0.53. The metal-to-nitrogen atom ratio could not be reliably obtained due to the limitations of the EDS instrument. Nonetheless, the EDS mapping results in Figure 5.6 reveals uniform distribution for all metal elements, except for Al, which seems to have association with oxygen, presumably from amorphous Al_2O_3 that might be present in the starting powder or formed during RFS.

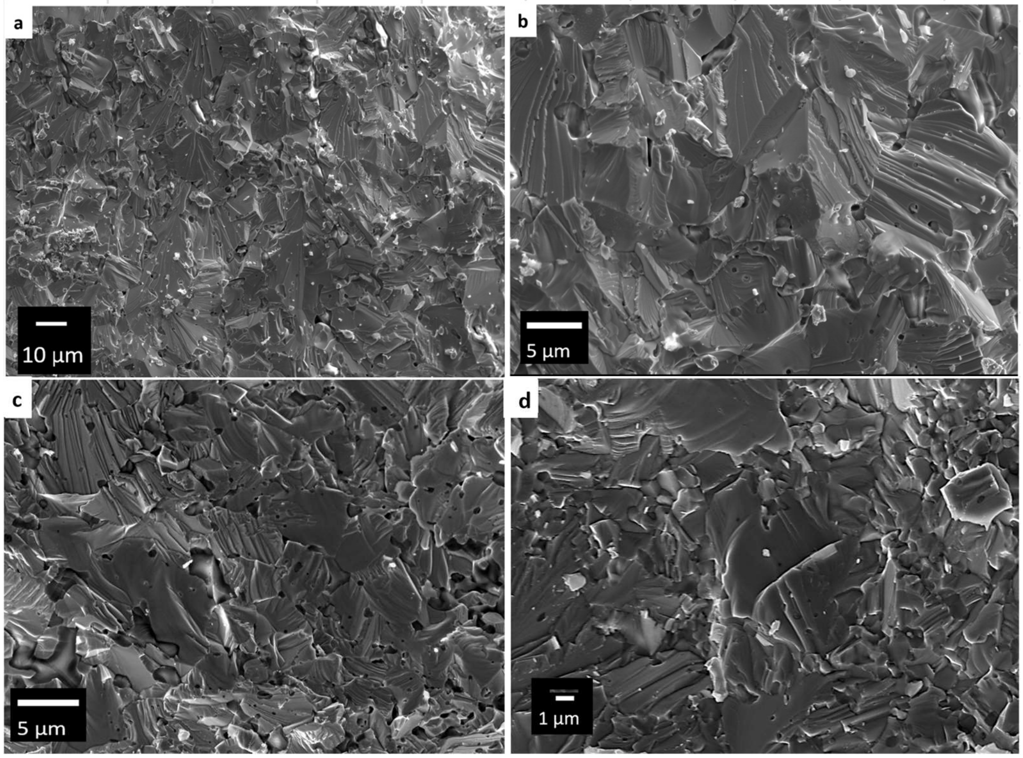

Figure 5. 5. SEM images of a fractured surface of reactive flash sintered (a and b) $(Al_{0.17}Nb_{0.17}Ta_{0.17}Ti_{0.32}Zr_{0.17})N$, (c) $(Al_{0.20}Nb_{0.20}Ta_{0.20}Ti_{0.40})N$ and (d) $(Al_{0.20}Nb_{0.20}Ti_{0.40}Zr_{0.20})N$.

Figure 5.7a depicts the HAADF STEM images of $(Al_{0.17}Nb_{0.17}Ta_{0.17}Ti_{0.32}Zr_{0.17})N$, indicating that the synthesized HEN is indeed a uniform random solid solution. Additionally, Figure 5.7b shows the STEM EDS elemental mapping results, revealing that the distributions of all six elements are very homogeneous (i.e., no clustering or segregation) even at the nanometer scale.

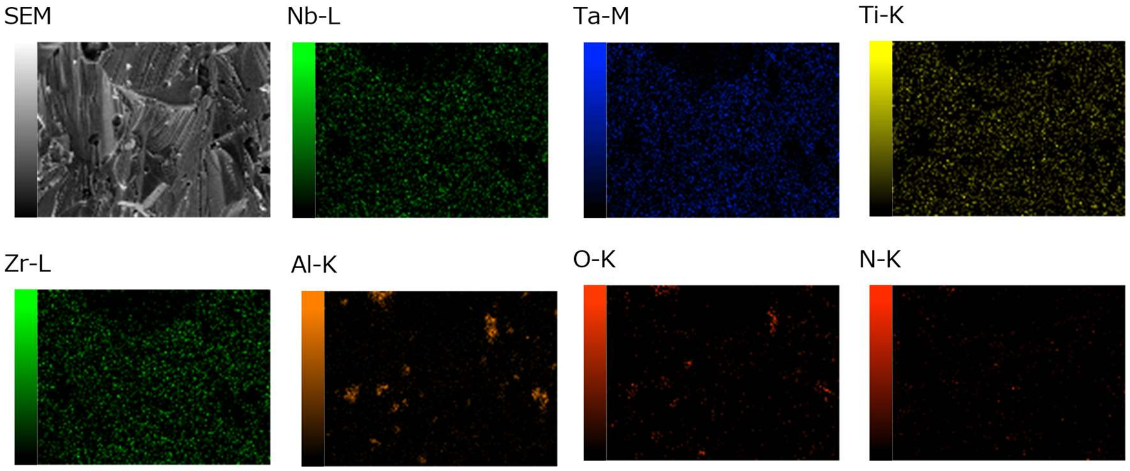

Figure 5. 6. EDS area map of reactive flash sintered $(Al_{0.17}Nb_{0.17}Ta_{0.17}Ti_{0.32}Zr_{0.17})N$ showing the uniform distribution of Al, Nb, Ta, Ti, Zr, and N.

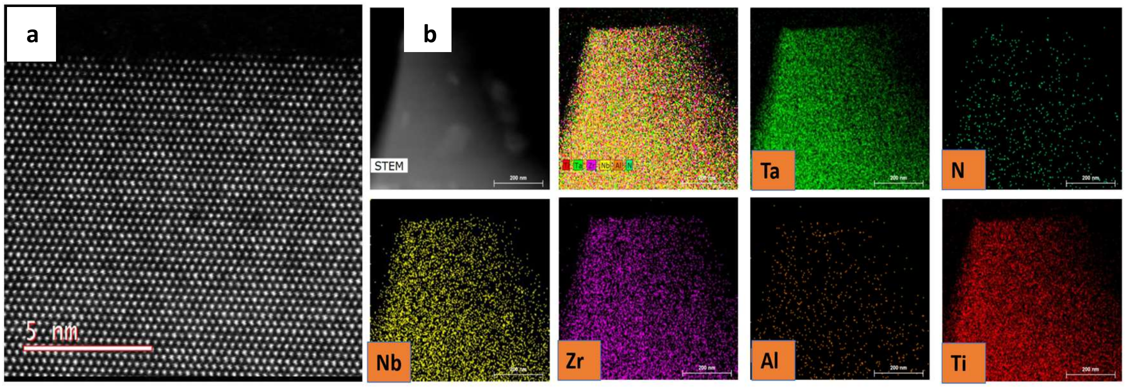

Figure 5. 7. HAADF STEM images of reactive flash sintered $(Al_{0.17}Nb_{0.17}Ta_{0.17}Ti_{0.32}Zr_{0.17})N$.

5.3.4. Oxidation resistance

Figure 5.8 gives TGA plots for fractured pieces of three HENs from RFS as well as flash sintered binary nitrides. $(Al_{0.17}Nb_{0.17}Ta_{0.17}Ti_{0.32}Zr_{0.17})N$ shows very little weight gain (< ~1 wt.%) before ~600°C, and the onset temperature for rapid oxidation is ~750°C. After that, there is steady weight gain till ~1050°C, followed by a more rapid weight gain till ~1275°C, after which there was no more changes. The weight gain is attributed to the conversion of HEN into oxides: For the nominal composition of $(Al_{0.17}Nb_{0.17}Ta_{0.17}Ti_{0.32}Zr_{0.17})N$, the theoretical weight gain, assuming all products of stable binary oxides (Al_2O_3, Nb_2O_5, Ta_2O_5, TiO_2, ZrO_2), would be 20.15%; if the stoichiometry is closer to the EDS-determined value of $(Al_{0.15}Nb_{0.17}Ta_{0.16}Ti_{0.36}Zr_{0.17})N$, the weight gain would be 20.68%. These values match well with the measured weight gain of 20.6%. Compared to binary nitrides of NbN, TaN, TiN, and ZrN, the onset of oxidation for $(Al_{0.17}Nb_{0.17}Ta_{0.17}Ti_{0.32}Zr_{0.17})N$ HEN shows a delay of ~200-300°C. The origin for such an improvement in oxidation resistance is not clear. It might be due to the formation of a high entropy random solid solution. It might also come from the *amorphous* Al_2O_3 layer, which restricts the inward diffusion of O_2. A third possibility is that Ta doping might help enhance oxidation resistance by generating Ta^{5+} ions that reduce the concentration of oxygen vacancies in oxide shells [230]. This is supported by the observation that Ta-containing $(Al_{0.20}Nb_{0.20}Ta_{0.20}Ti_{0.40})N$ also shows good resistance to oxidation in the air until ~600°C, while $(Al_{0.20}Nb_{0.20}Ti_{0.40}Zr_{0.20})N$ shows almost no difference in oxidation resistance compared to various binary nitrides (e.g., NbN and ZrN). Further studies are needed to understand the improvement in oxidation resistance and the relationship to the HEN metal stoichiometry.

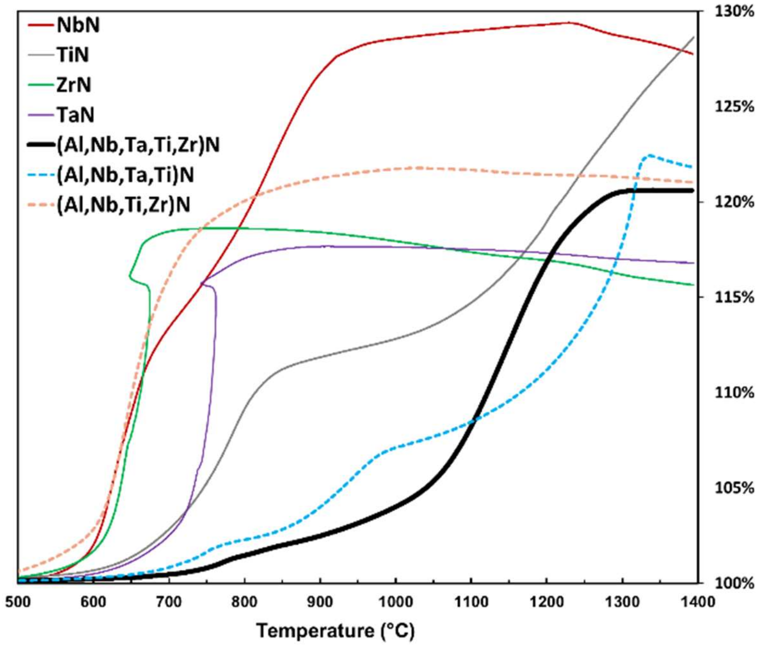

Figure 5. 8. Comparison of TGA plots for binary nitrides of NbN, TaN, TiN and ZrN versus bulk high entropy nitrides of $(Al_{0.17}Nb_{0.17}Ta_{0.17}Ti_{0.32}Zr_{0.17})N$, $(Al_{0.2}Nb_{0.2}Ta_{0.2}Ti_{0.4})N$, and $(Al_{0.2}Nb_{0.2}Ti_{0.4}Zr_{0.1})N$ for bulk subsequent reactive flash sintering

5.3.5. Mechanical properties and behaviors at high pressure

The Vickers hardness for both the (reactive) flash sintered HENs and binary nitrides were evaluated by the indentation method, and the results are summarized in Table 5.2. HEN $(Al_{0.17}Nb_{0.17}Ta_{0.17}Ti_{0.32}Zr_{0.17})N$ demonstrates a Vickers hardness of 16.31±1.61 GPa, which is comparable to that of NbN (15.74±0.61 GPa), TaN (12.48±0.4 GPa), and ZrN (14.2±0.9 GPa), all sintered in a similar fashion. Flash sintered TiN exhibits low hardness at 8±1.47 GPa, likely due to high porosity (see Figure S5 (c)), since reported TiN hardness is typically ~18-25 GPa [6, 206]. HENs of $(Al_{0.20}Nb_{0.20}Ta_{0.20}Ti_{0.40})N$ and $(Al_{0.20}Nb_{0.20}Ti_{0.40}Zr_{0.20})N$, which also form near single-phase solid solutions, exhibit even higher hardness values of 18.1 ± 0.41 GPa and 19.07 ± 0.62 GPa, respectively.

Fracture toughness for HEN as well as flash sintered NbN, TaN, TiN, and ZrN binary nitrides measured in this study as well as literature reported values are also summarized in

Table 5.2. For $(Al_{0.17}Nb_{0.17}Ta_{0.17}Ti_{0.32}Zr_{0.17})N$, K_{1c} was 7.81 ± 1.37 $MPa{\cdot}m^{1/2}$, which is much higher compared to all binary nitrides. $(Al_{0.20}Nb_{0.20}Ti_{0.40}Zr_{0.20})N$ gives a similar K_{1c} value of 7.89 ± 2.88 MPa $m^{1/2}$, while $(Al_{0.20}Nb_{0.20}Ta_{0.20}Ti_{0.40})N$ shows the highest K_{1c} of 9.17 ± 2.31 $MPa{\cdot}m^{1/2}$, almost 2-4 times of its constituent binary nitrides and the estimated values from rule of mixture (ROM).

As stated, apart from mechanical properties at ambient condition, the responses of HEN under high pressure have also been measured using diamond anvil cell technique. It has long been known that nitrides might go through phase transformation under pressure, even at room temperature. For example, hexagonal wurtzite-type AlN transforms to cubic phase (NaCl) under a pressure of 14 GPa at room temperature [231], which is accompanied by large (~20%) volume contraction. Upon pressure release, the rock salt structure persists at atmospheric pressure. For TiN, an isostructural phase transition at ~7 GPa has been reported [232], while Raman spectroscopy suggests such a transition can be attributed to N vacancy filling by Ti [233].

In this study, for HEN $(Al_{0.17}Nb_{0.17}Ta_{0.17}Ti_{0.32}Zr_{0.17})N$ powder, no phase transition was observed till 35.6 GPa, as seen in Figure 5.9. The crystal structure remains cubic rock salt as observed from collected diffraction patterns at different pressures. The bulk modulus B obtained from the P-V data is 285 GPa, which is comparable comparing with the rule of mixture value from the binary nitrides.

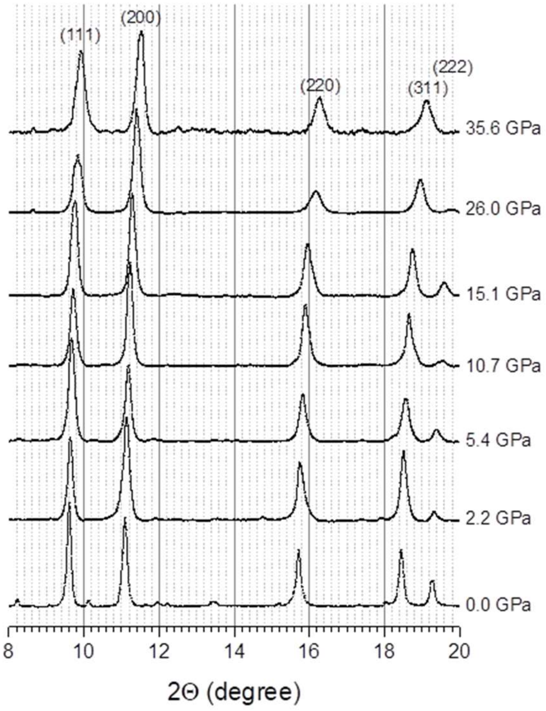

Figure 5. 9. Selected powder synchrotron (λ=0.424590Å) XRD patterns of $(Al_{0.17}Nb_{0.17}Ta_{0.17}Ti_{0.32}Zr_{0.17})N$ high entropy nitride collected at different pressures in diamond anvil cell.

5.3.6. DFT calculations

DFT is used to calculate the mechanical properties of all binary nitrides including AlN, NbN, TaN, TiN, ZrN, and the near equiatomic $(Al_{0.17}Nb_{0.17}Ta_{0.17}Ti_{0.32}Zr_{0.17})N$ HEN. In HEN, three different configurations were used to get statistical average. In all systems, the crystal structure is assumed to be rock salt, even though in reality some do not have the rock salt as the most stable structure (e.g., AlN). Note after relaxation, HEN lattice is severely distorted. To calculate the fracture toughness, a purely brittle fracture is assumed. This means that the fracture creates two perfect surfaces and there are no plastic deformation or phase transformation during fracture. So the calculated fracture toughness can be considered as a minimum possible value. Based on this assumption, the fracture toughness for a [$h\ k\ l$] crystallographic orientation is calculated based on the corresponding surface energy (γ_{hkl}) and Young's modulus (E_{hkl}):

$$K_{1c}^{hkl} = \sqrt{4\,\gamma_{hk}\ E_{hkl}}$$

For simplicity, only properties along the [100], [110], and [111] directions are calculated. The DFT-calculated fracture toughness and other mechanical properties are given in the Table 5.2. Based on this simple brittle fracture model, the theoretical HEN's fracture toughness would be similar to the rule of mixture (ROM) of its binary nitrides. Therefore, from the bond-breaking viewpoint, the intrinsic fracture toughness is would not be too different for HEN.

Nevertheless, the experimentally observed enhancement in fracture toughness (or better resistance to crack propagation) for HEN over binary nitrides is interesting. It might be related to some microstructure feature in the HEN phase from RFS. In fact, the improved fracture toughness appears to be associated with the *layered structure* and closely spaced slip lines (see Figures 5.5) that remnant fracture of MAX phases, despite the difference in crystal structure. Such high fracture toughness (~7-9 $\mathrm{MPa\cdot m^{1/2}}$) and layered cross-section are *not* observed for binary nitrides (e.g., NbN, TaN, ZrN), or ternary nitrides (e.g., $Ti_{0.5}Zr_{0.5}N$ [227]), or even quaternary nitrides such as $(Nb_{1/3}Ta_{1/3}Ti_{1/3})N$ [211], all prepared by (reactive) flash sintering under similar conditions (DC voltage, pressure, and max current density, and processing time). Whether there is any layered "super-structure" (e.g., the HEN phase separates into different regions (e.g., Ti-Zr rich region versus Nb-Ta rich region as in corresponding high entropy alloys [234]) is not clear at the moment due to instrument limitation. The enhancement of fracture toughness might also be due to the ductile phase toughening. Further studies on fine-scale microstructure using higher precision microscopy with EDS, as well as verification of the mechanical properties using alternative methods (e.g., three-point bending), are needed to confirm the observations and fully understand the relationship between bulk HEN properties (especially fracture toughness) and its dependence on composition and processing.

5.3.7. Superconductivity

Finally, low temperature electro-magnetic properties for HEN had also been measured. Prior studies have demonstrated that high entropy phenomenon does *not* hinder the presence of superconductivity. For example, the high entropy alloy of $Ta_{34}Nb_{33}Hf_8Zr_{14}Ti_{11}$ demonstrates superconductivity with a critical temperature of 7.3 K [235]. By rule of mixture, the calculated T_c is 4.71 K for the HEA. Temperature dependent magnetization and resistivity measurements on our HEN sample had been carried out for $(Al_{0.17}Nb_{0.17}Ta_{0.17}Ti_{0.32}Zr_{0.17})N$ HEN to find out if it also exhibits superconductivity. Experiments showed the HEN is indeed a superconductor. The onset superconducting transition temperature probed in resistivity is ~ 7 K, as shown in Figure 5.10(a). Superconducting diamagnetism was also observed below 5 K (Figure 5.10(b)). Since magnetization is a *bulk* measurement, while resistivity measurement is not, it is common that the transition temperature probed in magnetization is less than that in resistivity. Moreover, we also measured magnetic field dependence of magnetization and observed small magnetic hysteresis (see Figure 5.10(c)), indicating that $(Al_{0.17}Nb_{0.17}Ta_{0.17}Ti_{0.32}Zr_{0.17})N$ is a type-II superconductor. The lower critical field H_{c1} measured from the magnetization measurements is ~ 20 Oe (see insert in Figure 5.11(c)). The upper critical field H_{c2} was found to be ~ 2.7 T, from the field dependent measurements of resistivity (Figure 5.10(d)).

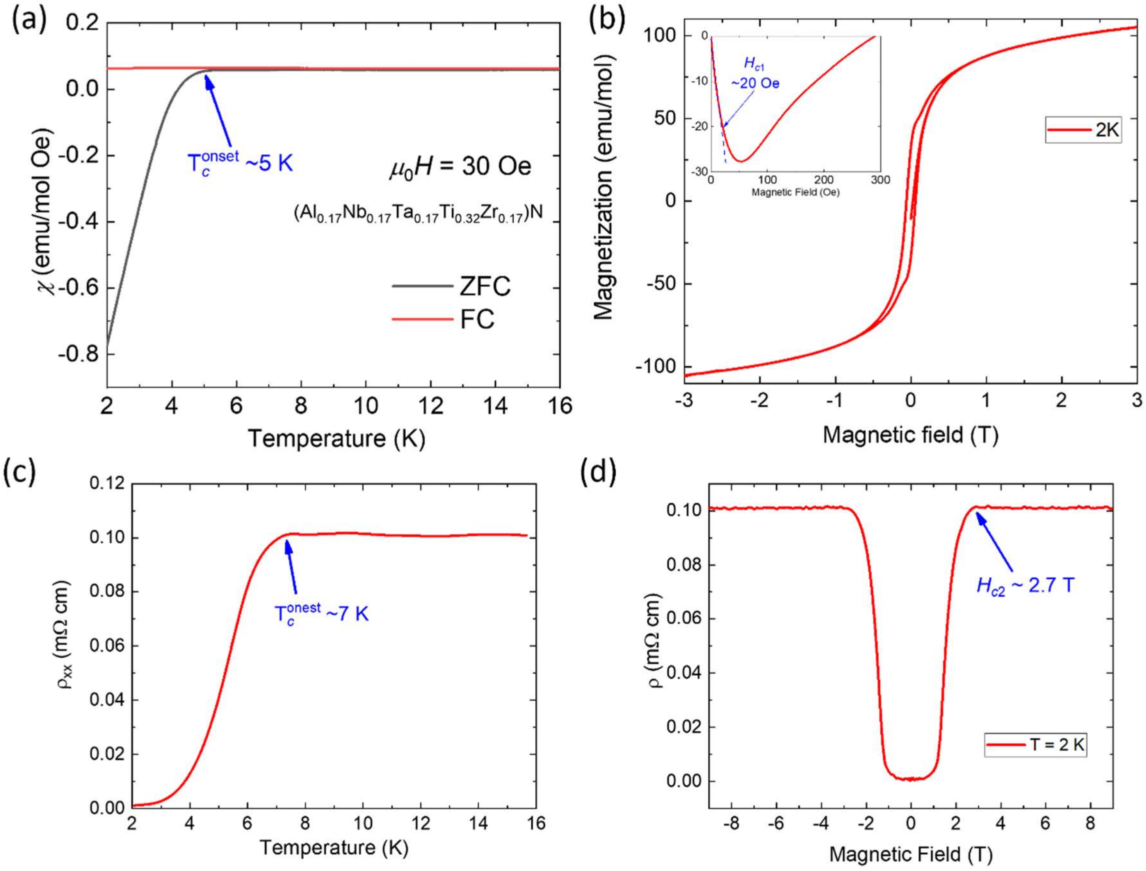

Figure 5. 10. (a) Temperature dependence of magnetic susceptibility at magnetic field B = 30 Oe for HEN sample, (b) Field-dependent magnetization M(H) at 2 K for HEN sample, the inset shows the enlargement of the lower field data. (c) Temperature dependence of longitudinal resistivity ρ_{xx}, (d) Field-dependent magnetoresistance at 2K.

It is interesting to note that while one parent compound - AlN is a large-gap insulator (6.2 eV), the inclusion of Al in HEN $(Al_{0.17}Nb_{0.17}Ta_{0.17}Ti_{0.32}Zr_{0.17})N$ does not completely suppress superconducting pairing. The expected T_c from ROM for the four superconducting parent compounds (ZrN, $T_c = 9.05$ K)[236]; NbN, $T_c = 17.5$ K[237] and TaN, $T_c = 10.2$ K[238]; TiN, $T_c = 6$ K[239]) is ~11 K (based on ROM), 4 K higher than what is observed in our HEN sample ($T_c = 7$ K). This implies that Al does effect superconductivity to some extent, but it does not completely destroy the superconductivity.

Our observations of superconductivity in the $(Al_{0.17}Nb_{0.17}Ta_{0.17}Ti_{0.32}Zr_{0.17})N$ system helps in expanding the diversity of the superconducting HEN family and provides insights into the superconducting mechanism in high-entropy nitrides.

5.4. Conclusions

This research demonstrates, for the first time, reactive flash sintering (RFS) of bulk high entropy nitrides such as $(Al_{0.17}Nb_{0.17}Ta_{0.17}Ti_{0.32}Zr_{0.17})N$, $(Al_{0.20}Nb_{0.20}Ta_{0.20}Ti_{0.40})N$ and $(Al_{0.20}Nb_{0.20}Ti_{0.40}Zr_{0.20})N$ using commercial binary nitrides. Near single phase HEN solid solutions are formed at high temperature during RFS, as evidenced by both *ex situ* XRD and *in situ* synchrotron study, and they were preserved upon cooling to room temperature, suggesting thermodynamic stability of the HEN phases. SEM revealed dense microstructure for the HENs, while HAADF STEM showed atomic scale structure. EDS from both SEM and STEM confirmed elemental uniformity with no noticeable segregation.

Some of the HEN properties are close to expectation. For example, the onset of oxidation temperature and hardness are largely in line with individual binary nitrides. Its bulk modulus hasan average of 290±40 GPa. HEN such as $(Al_{0.17}Nb_{0.17}Ta_{0.17}Ti_{0.32}Zr_{0.17})N$ does not show phase transition up to 35.6 GPa and the crystal structure remains cubic rock salt, like NbN, TiN and ZrN. HEN like $(Al_{0.17}Nb_{0.17}Ta_{0.17}Ti_{0.32}Zr_{0.17})N$ also displays type-II superconductivity with critical temperature T_c of ~7 K, slightly lower than average Tc for binary nitrides.

On the other hand, measured fracture toughness from indentation appears unique as it deviates significantly from the average: the measured values by indentation are about two to four times of the starting binary nitrides. The higher toughness might be associated with finely spaced layered structures in the fractured surface, similar to those for hexagonal

MAX-phase carbides and nitrides, despite HEN's cubic structure. Such phenomena are not observed for other nitrides including binary (e.g., NbN), ternary (e.g., $Ti_{0.5}Zr_{0.5}N$), and quaternary (e.g., $(Nb_{1/3}Ta_{1/3}Ti_{1/3})N$), all prepared by (reactive) flash sintering under similar conditions. Future studies will be focusing on revealing the underlying relationship between HEN microstructure and fracture toughness using both experiments (e.g., three-point bending strength and toughness measurements) using larger samples as well as computational modeling at different scales to fully understand the effects of composition and processing on the properties of such HENs and if and how high entropy effect is playing a role in the observed properties.

Table 5. 1. Summary of the (reaction) flash sintering experiments in this study. The experimental conditions include precursor and molar ratio, initial DC voltage, maximum current reached, and total time, as well as products' final phase composition and properties

Sample ID	Precursors	Molar Ratio	Initial DC Voltage	Max Current	Total Time	Major Phase(s)	Minor Phase(s)	Oxidation Onset Temp (˚C)	Total Weight Gain
NbN	NbN	-	8 V	168 A	350 s	*c*-NbN	-	576	27.2%
TaN	TaN	-	8 V	166 A	350 s	*h*-TaN	-	644	16.8%
TiN	TiN	-	8 V	193 A	350 s	*c*-TiN	-	630	28.5%
ZrN	ZrN	-	8 V	193 A	350 s	*c*-ZrN	*t*-ZrO_2	567	15.6%
HEN 1	AlN+NbN+TaN+TiN+ZrN	0.53 : 0.53 : 0.53 : 1 : 0.53	8 V	191 A	350 s	$(Al_{0.17}Nb_{0.17}Ta_{0.17}Ti_{0.32}Zr_{0.17})N$	*t*-ZrO_2, *o*-TiO_2, *c*-$Ta_{0.5}Nb_{0.5}C_{0.5}N_{0.5}$	775	20.6%
HEN 2	AlN+NbN+TaN+TiN	0.5:0.5:0.5:1	8 V	147 A	350 s	$(Al_{0.20}Nb_{0.20}Ta_{0.20}Ti_{0.40})N$	*o*-TiO_2, *c*-$Ta_{0.5}Nb_{0.5}C_{0.5}N_{0.5}$	717	21.5%
HEN 3	AlN+NbN+TiN+ZrN	0.5:0.5:1:0.5	8 V	135 A	350 s	$(Al_{0.20}Nb_{0.20}Ti_{0.40}Zr_{0.20})N$	*t*-ZrO_2, *o*-TiO_2, *o*-Al_2O_3, *c*-$Al_3(O_3N)$	531	21.0%

Table 5. 2. Literature, computation, and experimental data on mechanical properties of binary and high entropy nitrides.

Composition	**E_{DFT} (GPa)**	**B_{DFT} (GPa)**	**G_{DFT} (GPa)**	**H_v (DFT) (GPa)**	**H_v (Lit.) (GPa)**	**H_v (exp.) (GPa)**	**K_{1c}^{100} (DFT) (MPa·m$^{1/2}$)**	**K_{1c}^{110} (DFT) (MPa·m$^{1/2}$)**	**K_{1c}^{111} (DFT) (MPa·m$^{1/2}$)**	**K_{1c} (Lit.) (MPa·m$^{1/2}$)**	**K_{1c} (exp.) (MPa·m$^{1/2}$)**
c-AlN	539	253	236	42	17.7 [255]	-	1.32	2.55	4.12	3.98 [256]	-
c-NbN	375	309	144	12.1	17 [257]	15.74±0.61	1.38	1.41	1.31	3.2 [258]	2.45±0.71
c-TaN	393	346	150	11.1	20.9 [259]	12.48±0.4	1.40	1.21	1.02	3.3 [258]	3.73±1.56
c-TiN	460	293	186	21.9	14.9 [260]	8.0±1.5	1.61	2.13	2.37	2.7 [261]	2.3±0.89
c-ZrN	391	250	158	19.6	16.6 [6]	14.2±0.9	1.65	1.89	1.85	4.25 [262]	4.6±0.6
$(Al_{0.17}Nb_{0.17}Ta_{0.17}Ti_{0.32}Zr_{0.17})N$ - value by rule of mixture	432 ±68	290 ±40	175 ±38	21.3 ±12.4			1.47 ± 0.15	1.84 ± 0.54	2.13 ± 1.22		
$(Al_{0.17}Nb_{0.17}Ta_{0.17}Ti_{0.32}Zr_{0.17})N$	**380**	**272**	**150**	**15.7**	**-**	**16.31±1.61**	**1.60**	**1.74**	**1.64**	**-**	**7.81 ± 1.37**
$(Al_{0.20}Nb_{0.20}Ta_{0.20}Ti_{0.40})N$	-	-	-	-	-	18.1 ± 0.41	-	-	-	-	**7.89 ± 2.88**
$(Al_{0.20}Nb_{0.20}Ti_{0.40}Zr_{0.20})N$	-	-	-	-	-	19.07 ± 0.62	-	-	-	-	**9.17 ± 2.31**

5.5. Supplementary

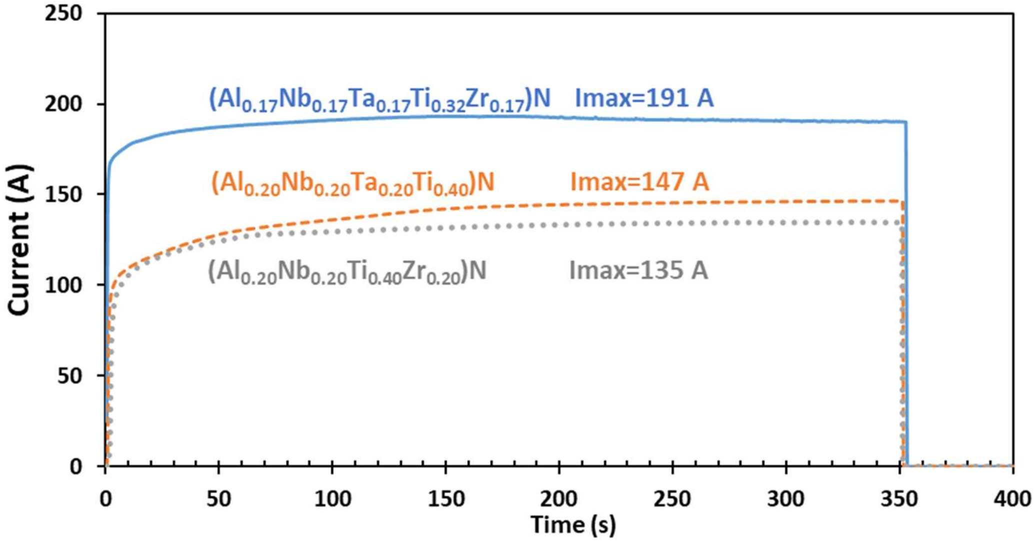

Figure S1 Plot of resulting current vs. time for reactive flash sintering of $(Al_{0.17}Nb_{0.17}Ta_{0.17}Ti_{0.32}Zr_{0.17})N$ (solid line), $(Al_{0.20}Nb_{0.20}Ta_{0.20}Ti_{0.40})N$ (dashed line) and $(Al_{0.20}Nb_{0.20}Ti_{0.40}Zr_{0.20})N$ (dotted line) from non-equimolar binary nitride powder mixture.

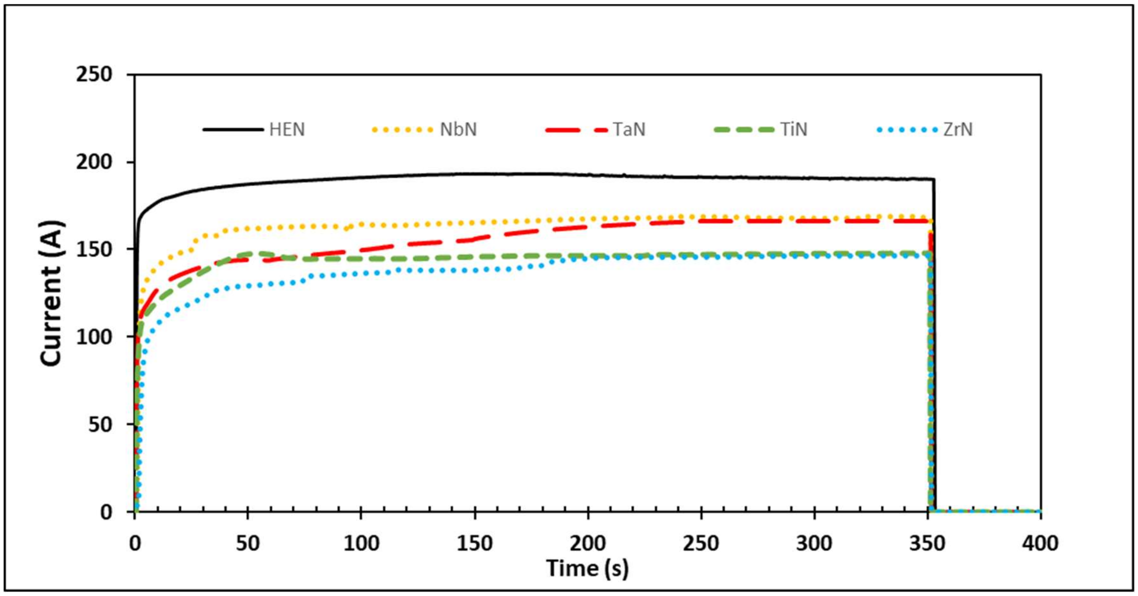

Figure S2 Plot of resulting current vs. time for reaction flash sintering of $(Al_{0.17}Nb_{0.17}Ta_{0.17}Ti_{0.32}Zr_{0.17})N$ (solid line) and binary nitrides NbN, TaN, TiN and ZrN.

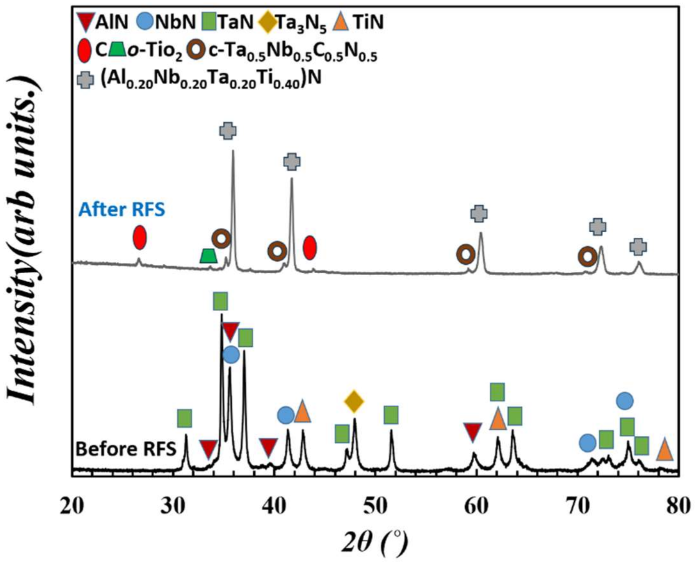

Figure S3 XRD patterns of $(Al_{0.20}Nb_{0.20}Ta_{0.20}Ti_{0.40})N$ mixture (a) before and (b) after reactive flash sintering. Note that the sample changes from a mixture of binary nitrides to $(Al_{0.20}Nb_{0.20}Ta_{0.20}Ti_{0.40})N$ single-phase solid solution.

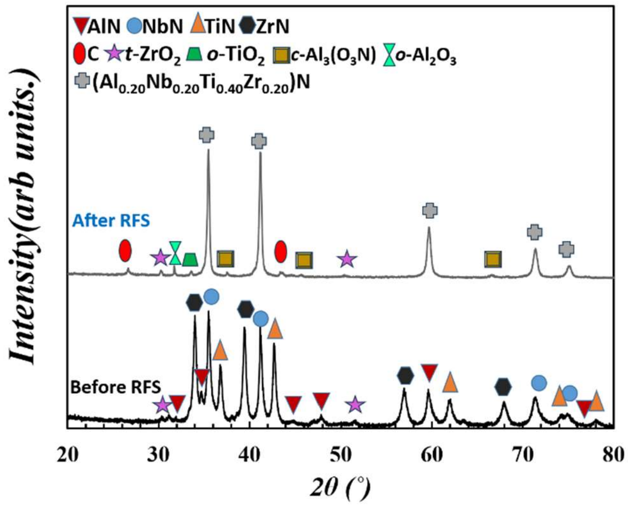

Figure S4 XRD patterns of $(Al_{0.20}Nb_{0.20}Ti_{0.40}Zr_{0.20})N$ mixture (a) before and (b) after reactive flash sintering. Note that the sample changes from a mixture of binary nitrides to $(Al_{0.20}Nb_{0.20}Ti_{0.40}Zr_{0.20})N$ single-phase solid solution.

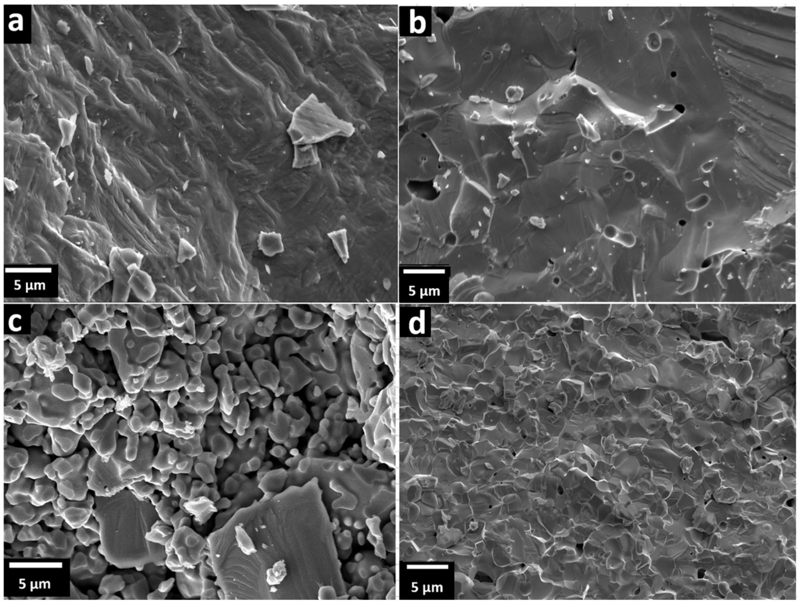

Figure S5 SEM images of the fractured surface of (a)NbN, (b)TaN, (c) TiN, and (d) ZrN sample from flash sintering.

Table S1 Values of elastic modulus E (GPa), hardness H (GPa), indentation load P (N), crack length c (m), and fracture toughness K_{1c} (MPa·m$^{1/2}$) for the $(Al_{0.17}Nb_{0.17}Ta_{0.17}Ti_{0.32}Zr_{0.17})N$ sample from standard RFS.

c (µm)	P (N)	E [a] (GPa)	H (GPa)	K_{1C} (MPa·m$^{1/2}$)
36.1	19.7	449	16.3	7627018
38.47				6933177
27.1				11726317
41.47				6194618
35.43				7844384
30.69				9730166
40				6539215
35.62				7781704
38.31				6976657
39.35				6701908
31.88				9190478
34.09				8311417
37.37				7241540
36.92				7374338
37.39				7235730
35.48				7827808
37.62				7169476
37.83				7109860
39.57				6646094
32.24				9036974
28.81				10697953
36.61				7468201
40.95				6312984

[a] E for AlN[214], NbN[248], TaN[249], TiN[198] and ZrN[250] from literature; E for $(Al_{0.17}Nb_{0.17}Ta_{0.17}Ti_{0.32}Zr_{0.17})N$ calculated from Rule of Mixture.

Table S2 Values of elastic modulus E (GPa), hardness H (GPa), indentation load P (N), crack length c (m), and fracture toughness K_{1c} (MPa·m$^{1/2}$) for the $(Al_{0.17}Nb_{0.17}Ta_{0.17}Ti_{0.32}Zr_{0.17})N$ sample from standard RFS.

c (μm)	P (N)	E^{b} (GPa)	H (GPa)	K_{1C} (MPa·m$^{1/2}$)
40.69	19.7	434.44	18.1	5949498
37.15				6819831
33.59				7932258
40.95				5892926
32.97				8157055
35.19				7397465
40.15				6069927
38.07				6574118
26.24				11488573
43.25				5429160
52.88				4015824
38.11				6563771
38.78				6394405
33.94				7809875
38.72				6409273
36.21				7087108
44.7				5167144
26.1				11581133
46.05				4941598
37.53				6716515
33.38				8007230
39.42				6239315
29.5				9637820
37.92				6613165
41.48				5780344
25.98				11661465
17.48				21130009
25.88				11729120
37.64				6687094
36.8				6917356
33.65				7911052
31.68				8660322
37.93				6610549
31.49				8738821
35.72				7233436
37.23				6797861
33.19				8076086

28.86				9960183
30.09				9355749
30.64				9104973
31.78				8619478
31.95				8550776
37.35				6765126

[b] E for AlN[214], NbN[248], TaN[249], and TiN[198] from literature; E for $(Al_{0.20}Nb_{0.20}Ta_{0.20}Ti_{0.40})N$ calculated from Rule of Mixture.

Table S3 Values of elastic modulus *E* (GPa), hardness *H* (GPa), indentation load *P* (N), crack length *c* (m), and fracture toughness K_{1c} (MPa·$m^{1/2}$) for the $(Al_{0.17}Nb_{0.17}Ta_{0.17}Ti_{0.32}Zr_{0.17})N$ sample from standard RFS.

c (μm)	*P* (N)	E^c (GPa)	*H* (GPa)	K_{1C} (MPa·$m^{1/2}$)
33.81	19.7	415	19.07	7479407
29.76				9057024
40.54				5696516
24.01				12498177
22.25				14010057
31.03				8506722
26.03				11071938
24.76				11934630
23				13330399
27.84				10009931
27.21				10359579
23.7				12744195
36.21				6748265
33.24				7672615
33.91				7446346
30.76				8618971
28.45				9689726
38.32				6198644
30.68				8652705
31.49				8321008
28.53				9648999
33.15				7703882
33.09				7724845
49.54				4216974
27.07				10440049
23.81				12655981
27.6				10140778
34.16				7364752
33.53				7573290
30.66				8661172
32.06				8100086

[c] E for AlN^{214}, NbN^{248}, TiN^{198} and ZrN^{250} from literature; E for $(Al_{0.20}Nb_{0.20}Ti_{0.40}Zr_{0.20})N$ calculated from Rule of Mixture.

Chapter VI. Summary and Future Work

6.1. Synthesis and flash sintering of zirconium nitride powder

The following *summary* is from the abstract for the author's paper Das S, Dubois D, Sozal MSI, Emirov Y, Jafarizadeh B, Wang C, et al. Synthesis and flash sintering of zirconium nitride powder. J Am Ceram Soc. 2022; 105: 3925–3936. https://doi.org/10.1111/jace.18421.

"Zirconium nitride (ZrN) is a transition metal nitride of great interest due to its excellent physical and chemical properties. This study aims to synthesize ZrN fine powders by a facile and low-cost urea route that avoids the use of any solvent. ZrCl4 and urea mixtures were heat-treated at up to 1600˚C in nitrogen gas. The products were characterized by X-ray diffraction, scanning electron microscopy, transmission electron microscopy, energy-dispersive X-ray spectroscopy, and thermogravimetric analysis. The effects of different processing parameters such as metal to urea molar ratio, heat treatment temperature, and dwelling time on the product phase and stoichiometry were studied to understand the synthesis method. In addition, synthesized ZrN powder was consolidated into near fully dense single-phase bulk ceramic with a homemade flash sintering setup. A constant DC electrical field of ∼80 V/cm and pressure of ∼14 MPa at room temperature triggered flash sintering without pre-heating, and the entire process finished in 200 s. The composition, microstructure, density, hardness, and oxidation properties of the sintered pellet were also characterized."

As to *future work*, subsequent studies should investigate ZrN properties in detail with an emphasis on elucidating the influence of defects, in particular vacancies in the nitrogen sub-lattice, on the materials' overall behavior and characteristics.

Furthermore, a thorough investigation into the material's oxidation process is required. Analyzing the complex processes and mechanisms of oxidation will shed light on the stability, and possible uses of the material.

6.2. Reactive Flash Sintering of TiZrN and TiAlN Ternary Metal Nitrides

The following *summary* is from the abstract for the author's paper Suprabha Das, Andriy Durygin, Vadym Drozd, Md Shariful Islam Sozal, Zhe Cheng, Reactive flash sintering of TiZrN and TiAlN ternary metal nitrides, Journal of the European Ceramic Society, Volume 44, Issue 4, 2024, Pages 2037-2051, ISSN 0955-2219, https://doi.org/10.1016/j.jeurceramsoc.2023.11.079.

"This study demonstrated the reactive flash sintering (RFS) for two powder mixtures: TiN-ZrN (both conducting) and AlN-TiN (TiN conducting but AlN insulating), targeting ternary metal nitrides (TMN) of $Ti_{0.5}Zr_{0.5}N$ and $Ti_{0.5}$Al.5N, respectively. A constant volage and pressure (e.g., 8 V DC, ~15 MPa) at room temperature triggered the flash (current density up to 27 A/mm2) without pre-heating, and the entire RFS process finished in a few minutes. For TiZrN, the flash was instantaneous whereas for TiAlN, there was a long incubation before the flash followed by a quick and dramatic flash. Both conventional ex situ XRD and in situ synchrotron study had been carried out. They showed a uniform $Ti_{0.57}Zr_{0.43}N$ solution formed in RFS and persisted upon cooling, while (Ti, Al) N solid solution formed at high temperature was not stable and likely went through a very quick phase separation in the cooling process. The final products from RFS had been characterized using SEM/EDS for microstructure. Both TiZrN and TiAlN were dense. Distribution of Ti, Zr, and N was uniform for TiZrN; for TiAlN, Ti and N distribution was uniform, while association of Al with oxygen was observed. TGA-DSC revealed the onset oxidation temperature for TiZrN was comparable to TiN and ZrN, while it was higher by ~200 °C for TiAlN, likely due to the formation of Al_2O_3. In terms of mechanical properties such as hardness or fracture toughness, forming a single-phase solid solution (like TiZrN) does not offer obvious benefits. while large grain size from RFS seemed to be unfavorable. Future optimization of RFS condition and in-depth study by both experiments and simulation are needed to fully understand the composition-processing-structure-property relationships for such TMN from the reactive flash sintering process."

As to *future work*, the synthesis of ternary nitrides by the standard RFS needs to be optimized for better process efficiency and material properties. The temperature during RFS should be precisely measured in real-time to help improve understanding of the phase transformation process. In addition, further research on fine-scale microstructure characterization and its relationship to mechanical properties is also necessary to gain a more thorough understanding of the impacts of starting composition and RFS parameters.

6.3. Reactive flash sintering and characterization of bulk high entropy nitrides

The following *summary* is adapted with minor changes from the abstract for the author's conference presentation "reactive flash sintering and characterization of bulk high entropy nitrides" presented at MS&T, Ohio, 2023.

" High entropy nitrides (HEN) are single-phase nitrides with 5 or more metal elements at the cation site. Mixing of multiple elements at the cation sublattice increases the configuration entropy of the system and might offer enhanced physical or chemical properties compared to their constituent binary nitrides. This study synthesizes bulk HEN by reaction flash sintering (RFS) method. Commercial binary metal nitride powders were mixed and consolidated into single-phase HEN such as $(Al_{0.17}Nb_{0.17}Ta_{0.17}Ti_{0.32}Zr_{0.17})N$ using a homemade setup. A constant DC electrical field of ~40 V/cm and pressure of ~15 MPa at room temperature triggered RFS without pre-heating, and the entire process finished in ~350 s. Both *ex situ* XRD and *in situ* synchrotron studies are carried out to track the phase evolution during RFS and subsequent cooling. The microstructure, as well as properties such as oxidation resistance, mechanical properties and superconductivity are characterized by methods such as SEM/EDS, TGA, and indentation. The relationship between composition, microstructure and properties are discussed."

As to future work, verification of the mechanical properties especially fracture toughness is needed for the high entropy nitride phases. In addition, detailed microstructure and microchemical characterization and modelling at different scales are needed to understand the relationship between composition, structure and resulting material properties.

.

REFERENCES

1. Yin Y, Hang L, Zhang S, Bui XL. Thermal oxidation properties of titanium nitride and titanium-aluminum nitride materials - A perspective for high temperature air-stable solar selective absorber applications. *Thin Solid Films*. 2007;515(5):2829–2832. https://doi.org/10.1016/j.tsf.2006.03.042

2. Qamar A, Eisner SR, Senesky DG, Rais-Zadeh M. Ultra-High-Q Gallium Nitride SAW Resonators for Applications with Extreme Temperature Swings. *J Microelectromechanical Syst*. 2020;29(5):900–905. https://doi.org/10.1109/JMEMS.2020.2999040

3. Liu Z, Gong Y, Zhou W, *et al.* Ultrathin higherature oxidation-resistant coatings of hexagonal boron nitride. *Nat Commun*. 2013;4(May):1–8. https://doi.org/10.1038/ncomms3541

4. Jacobson N, Farmer S, Moore A, Sayir H. High-Temperature Oxidation of Boron Nitride: I, Monolithic Boron Nitride. *J Am Ceram Soc*. 1999;82(2):393–398. https://doi.org/10.1111/j.1551-2916.1999.tb20075.x

5. Demirskyi D, Vasylkiv O, Yoshimi K. Allotropic strengthening and in situ phase transformations during ultra-high-temperature flexure of bulk tantalum nitride. *Mater Sci Eng A*. 2021;826(June):141954. https://doi.org/10.1016/j.msea.2021.141954

6. Das S, Dubois D, Sozal MSI, *et al.* Synthesis and flash sintering of zirconium nitride powder. *J Am Ceram Soc*. 2022;105(6):3925–3936. https://doi.org/10.1111/jace.18421

7. Bellosi A, Monteverde F. Ultra-high temperature ceramics: Microstructure control and properties improvement related to materials design and processing procedures. *Eur Sp Agency, (Special Publ ESA SP*. 2006;(631).

8. DISALVO FJ, CLARKE SJ. ChemInform Abstract: Ternary Nitrides: A Rapidly Growing Class of New Materials. *ChemInform*. 2010;27(50):no-no. https://doi.org/10.1002/chin.199650314

9. Djemia P, Benhamida M, Bouamama K, Belliard L, Faurie D, Abadias G. Structural and elastic properties of ternary metal nitrides TixTa1-xN alloys: First-principles calculations versus experiments. *Surf Coatings Technol*. 2013;215:199–208. https://doi.org/10.1016/j.surfcoat.2012.09.059

10. Matenoglou GM, Koutsokeras LE, Lekka CE, *et al.* Structure, stability and bonding of ternary transition metal nitrides. *Surf Coatings Technol*. 2009;204(6–7):911–914. https://doi.org/10.1016/j.surfcoat.2009.06.032

11. Tareen AK, Priyanga GS, Behara S, Thomas T, Yang M. Mixed ternary transition metal nitrides: A comprehensive review of synthesis, electronic structure, and properties of engineering relevance. *Prog Solid State Chem*. 2019;53(November 2018):1–26. https://doi.org/10.1016/j.progsolidstchem.2018.11.001

12. Vennos DA, Badding ME, DiSalvo FJ. Synthesis, Structure, and Properties of a New Ternary Metal Nitride, Ca3CrN3. *Inorg Chem*. 1990;29(20):4059–4062. https://doi.org/10.1021/ic00345a030

13. Pukari M, Takano M. Sintering and characterization of ZrN and (Dy,Zr)N as surrogate materials for fast reactor nitride fuel. *J Nucl Mater*. 2014;444(1–3):7–13. https://doi.org/10.1016/j.jnucmat.2013.09.001

14. Fokin VN, Fokina EE, Tarasov BP. Hydride and ammonia dispersion of metals. *Russ J Inorg Chem*. 2010;55(10):1536–1540. https://doi.org/10.1134/S0036023610100074

15. Konuma M, Matsumoto O. NITRIDING OF ZIRCONIUM IN A RADIO FREQUENCY DISCHARGE. *J Less Common Met*. 1977;55:97–102. https://doi.org/https://doi.org/10.1016/0022-5088(77)90265-X

16. Calka A. Formation of titanium and zirconium nitrides by mechanical alloying. *Appl Phys Lett*. 1991;59(13):1568–1569. https://doi.org/10.1063/1.106285

17. El-Eskandarany MS, Ashour AH. Mechanically induced gas-solid reaction for the synthesis of nanocrystalline ZrN powders and their subsequent consolidations. *J Alloys Compd*. 2000;313(1–2):224–234. https://doi.org/10.1016/S0925-8388(00)01175-0

18. Sun Y, Yao B, He Q, Su F, Wang HZ. Synthesis and formation mechanism of cubic ZrN nanopowders by mechanochemical reaction of ZrCl4 and Li3N. *J Alloys Compd*. 2009;479(1–2):599–602. https://doi.org/10.1016/j.jallcom.2008.12.149

19. Puclin T, Kaczmarek WA. Formation of zirconium nitride via mechanochemical processing. *J Mater Sci Lett*. 1996;15(20):1799–1800. https://doi.org/10.1007/BF00275346

20. Wu ZY, Chen Z, Wang L, *et al.* Solid-state synthesis of zirconium nitride and hafnium nitride powders. *J Ceram Soc Japan*. 2021;129(3):200–203. https://doi.org/10.2109/jcersj2.20177

21. Chen Y, Deng C, Yu C, Ding J, Zhu H. Molten-salt nitridation synthesis of cubic ZrN nanopowders at low temperature via magnesium thermal reduction. *Ceram Int*. 2018;44(7):8710–8715. https://doi.org/10.1016/j.ceramint.2018.02.019

22. Fu B, Gao L. Synthesis of nanocrystalline zirconium nitride powders by reduction-nitridation of zirconium oxide. *J Am Ceram Soc*. 2004;87(4):696–698. https://doi.org/10.1111/j.1551-2916.2004.00696.x

23. Yin L, Jones MI. Synthesis of ZrN powders by aluminum-reduction nitridation of ZrO2 powders with CaCO3 additive. *Ceram Int*. 2017;43(3):3183–3189. https://doi.org/10.1016/j.ceramint.2016.11.140

24. Jin T, Sang X, Unocic RR, *et al.* Mechanochemical-Assisted Synthesis of High-Entropy Metal Nitride via a Soft Urea Strategy. *Adv Mater*. 2018;30(23):1–5. https://doi.org/10.1002/adma.201707512

25. Gu Y, Guo F, Qian Y, Zheng H, Yang Z. A benzene-thermal synthesis of powdered cubic zirconium nitride. *Mater Lett*. 2003;57(11):1679–1682. https://doi.org/10.1016/S0167-577X(02)01051-0

26. Wu X, Liu G, Li J, Yang Z, Li J. Combustion synthesis of ZrN and AlN using Si3N4 and BN as solid nitrogen sources. *Ceram Int*. 2018;44(10):11914–11917. https://doi.org/10.1016/j.ceramint.2018.03.200

27. Malikova E, Pautova J, Gromov A, Monogarov K, Larionov K, Teipel U. On the mechanism of zirconium nitride formation by zirconium, zirconia and yttria burning in air. *J Solid State Chem*. 2015;230:199–208. https://doi.org/10.1016/j.jssc.2015.07.007

28. Tsuchida T, Kawaguchi M, Kodaira K. Synthesis of ZrC and ZrN in air from mechanically activated Zr-C powder mixtures. *Solid State Ionics*. 1997;101–103(PART 1):149–154. https://doi.org/10.1016/s0167-2738(97)00332-9

29. Hector AL, Henshaw G, Komarov A V., Parkin IP. Nitrides from solid state metathesis reactions: Synthesis and mechanistics. *J Mater Process Technol*. 1998;300(3–4):103–107. https://doi.org/10.1016/s0924-0136(97)00405-6

30. Zhao S, Ma J, Xu R, *et al.* Synthesis and Characterization of Zirconium Nitride Nanopowders by Internal Gelation and Carbothermic Nitridation. *Sci Rep*. 2019;9(1):1–9. https://doi.org/10.1038/s41598-019-55450-x

31. Naim Katea S, Westin G. Carbothermal nitridation of solution synthesised ZrO2–carbon nanocomposites; phase-development from precursor to nitride. *Ceram Int*. 2021;47(8):10828–10847. https://doi.org/10.1016/j.ceramint.2020.12.200

32. Hiroshi YAMAMURA SE and TM. Factors Affecting the Formation Nitridation Rate of ZrN by the Carbothermal Method. *J Ceram Soc Japan*. 1998;653:650–653.

33. Harrison R, Rapaud O, Pradeilles N, Maître A, Lee WE. On the fabrication of ZrCxNy from ZrO2 via two-step carbothermic reduction-nitridation. *J Eur Ceram Soc*. 2015;35(5):1413–1421. https://doi.org/10.1016/j.jeurceramsoc.2014.11.005

34. Yugeswaran S, Ananthapadmanabhan P V., Kumaresan L, *et al.* Synthesis of zirconium nitride from zircon sand by transferred arc plasma assisted carbothermal reduction and nitridation process. *Ceram Int*. 2018;44(12):14789–14796. https://doi.org/10.1016/j.ceramint.2018.05.109

35. Giordano C, Antonietti M. Synthesis of crystalline metal nitride and metal carbide nanostructures by sol-gel chemistry. *Nano Today*. 2011;6(4):366–380. https://doi.org/10.1016/j.nantod.2011.06.002

36. Brancho JJ, Proctor AD, Panuganti S, Bartlett BM. Urea-glass preparation of titanium niobium nitrides and subsequent oxidation to photoactive titanium niobium oxynitrides. *Dalt Trans*. 2017;46(36):12081–12087. https://doi.org/10.1039/c7dt03077k

37. Qu F, Yuan Y, Yang M. Programmed Synthesis of Sn3N4 Nanoparticles via a Soft Chemistry Approach with Urea: Application for Ethanol Vapor Sensing. *Chem Mater*. 2017;29(3):969–974. https://doi.org/10.1021/acs.chemmater.6b03435

38. Gao Q, Giordano C, Antonietti M. Controlled synthesis of tantalum oxynitride and nitride nanoparticles. *Small*. 2011;7(23):3334–3340. https://doi.org/10.1002/smll.201101207

39. Giordano C, Corbiere T. A step forward in metal nitride and carbide synthesis: From pure nanopowders to nanocomposites. *Colloid Polym Sci*. 2013;291(6):1297–1311. https://doi.org/10.1007/s00396-012-2865-x

40. Giordano C, Erpen C, Yao W, Antonietti M. Synthesis of Mo and W carbide and nitride nanoparticles via a simple “urea glass” route. *Nano Lett*. 2008;8(12):4659–4663. https://doi.org/10.1021/nl8018593

41. Giordano C, Erpen C, Yao W, Milke B, Antonietti M. Metal nitride and metal carbide nanoparticles by a soft urea pathway. *Chem Mater*. 2009;21(21):5136–5144. https://doi.org/10.1021/cm9018953

42. Yuan Y, Wang J, Adimi S, *et al.* Zirconium nitride catalysts surpass platinum for oxygen reduction. *Nat Mater*. 2020;19(3):282–286. https://doi.org/10.1038/s41563-019-0535-9

43. Joseph A, Thomas T. Synthesis of zirconium oxynitride via ammonia-free soft urea method for an asymmetric supercapacitor with high power density. *J Alloys Compd*. 2024;971(October 2023):172714. https://doi.org/10.1016/j.jallcom.2023.172714

44. Ma XF, Kang Z, Huang X, Zhang GJ. Synthesis of ZrN nanopowder via soft urea pathway. *Wuji Cailiao Xuebao/Journal Inorg Mater*. 2015;30(1):77–80. https://doi.org/10.15541/jim20140259

45. Pshenichnaya O V, Kuzenkova MA, Kislyi PS. The sintering of zirconium nitride in vacuum and in nitrogen. *Sov Powder Metall Met Ceram*. 1975;14(12):986–989. https://doi.org/10.1007/BF00807873

46. Pshenichnaya O V, Kuzenkova MA, Kislyi PS. Effect of powder particle size on the sintering of zirconium nitride. *Sov Powder Metall Met Ceram*. 1979;18(12):882–887. https://doi.org/10.1007/BF00815647

47. Petrykina RY, Shvedova LK. Hot pressing of transition metal nitrides and their properties. *Sov Powder Metall Met Ceram*. 1972;11(4):276–279. https://doi.org/10.1007/BF00800342

48. Lee G, Olevsky EA, Manière C, *et al.* Effect of electric current on densification behavior of conductive ceramic powders consolidated by spark plasma sintering. *Acta Mater*. 2018;144:524–533. https://doi.org/https://doi.org/10.1016/j.actamat.2017.11.010

49. Tang Y, Zhang G-J, Xue J-X, Wang X-G, Xu C-M, Huang X. Densification and mechanical properties of hot-pressed ZrN ceramics doped with Zr or Ti. *J Eur Ceram Soc*. 2013;33(7):1363–1371. https://doi.org/https://doi.org/10.1016/j.jeurceramsoc.2012.12.013

50. Park S, Han I, Lee H, Huh S, Park W. Microstructural evolution and grain morphology of ZrN pellets. *Met Mater Int*. 2009;15(2):187–192. https://doi.org/10.1007/s12540-009-0187-4

51. Lee G, Yurlova MS, Giuntini D, *et al.* Densification of zirconium nitride by spark plasma sintering and high voltage electric discharge consolidation: A comparative analysis. *Ceram Int*. 2015;41(10, Part B):14973–14987. https://doi.org/https://doi.org/10.1016/j.ceramint.2015.08.042

52. Adachi J, Kurosaki K, Uno M, Yamanaka S. Thermal and electrical properties of zirconium nitride. *J Alloys Compd*. 2005;399(1–2):242–244. https://doi.org/10.1016/j.jallcom.2005.03.005

53. Adachi J, Kurosaki K, Uno M, Yamanaka S. Porosity influence on the mechanical properties of polycrystalline zirconium nitride ceramics. *J Nucl Mater*. 2006;358(2–3):106–110. https://doi.org/10.1016/j.jnucmat.2006.07.002

54. Adachi J, Kurosaki K, Uno M, Yamanaka S. Porosity influence on the mechanical properties of polycrystalline zirconium nitride ceramics. *J Nucl Mater*. 2006;358(2):106–110. https://doi.org/https://doi.org/10.1016/j.jnucmat.2006.07.002

55. Chernyavskii AS. Synthesis of Ceramics Based on Titanium, Zirconium, and Hafnium Nitrides. *Inorg Mater*. 2019;55(13):1303–1327. https://doi.org/10.1134/S0020168519130016

56. Lin Y-W, Lu C-W, Yu G-P, Huang J-H. Structure and Properties of Nanocrystalline $(TiZr)_xN_{1-x}$ Thin Films Deposited by DC Unbalanced Magnetron Sputtering. *J Nanomater*. 2016;2016:2982184. https://doi.org/10.1155/2016/2982184

57. Lin Y-W, Huang J-H, Cheng W-J, Yu G-P. Effect of Ti interlayer on mechanical properties of TiZrN coatings on D2 steel. *Surf Coatings Technol*. 2018;350:745–754. https://doi.org/https://doi.org/10.1016/j.surfcoat.2018.04.077

58. Chinsakolthanakorn S, Buranawong A, Witit-anun N, Chaiyakun S, Limsuwan P. Characterization of Nanostructured TiZrN Thin Films Deposited by Reactive DC Magnetron Co-sputtering. *Procedia Eng*. 2012;32:571–576. https://doi.org/https://doi.org/10.1016/j.proeng.2012.01.1310

59. Lin Y-W, Huang J-H, Yu G-P. Effect of nitrogen flow rate on properties of nanostructured TiZrN thin films produced by radio frequency magnetron sputtering. *Thin Solid Films*. 2010;518(24):7308–7311. https://doi.org/https://doi.org/10.1016/j.tsf.2010.04.099

60. Milošev I, Strehblow H-H, Navinšek B. Oxidation of ternary TiZrN hard coatings studied by XPS. *Surf Interface Anal*. 1998;26(4):242–248. https://doi.org/https://doi.org/10.1002/(SICI)1096-9918(199804)26:4<242::AID-SIA367>3.0.CO;2-Y

61. Musil J, Štěpánek I, Musil J, *et al.* Properties of TiN, ZrN and ZrTiN coatings prepared by cathodic arc evaporation. *Mater Sci Eng A*. 1993;163(2):211–214. https://doi.org/https://doi.org/10.1016/0921-5093(93)90792-D

62. Du GY, Ba DC, Tan Z, Sun W, Liu K, Han QK. Vibration damping performance of ZrTiN coating deposited by arc ion plating on TC4 Titanium alloy. *Surf Coatings Technol*. 2013;229:172–175. https://doi.org/https://doi.org/10.1016/j.surfcoat.2012.05.140

63. Jang HW, Lee H-J, Ha J-Y, Kim K-H, Kwon T-Y. Surface characteristics and osteoblast cell response on TiN- and TiAlN-coated Ti implant. *Biomed Eng Lett*. 2011;1(2):99–107. https://doi.org/10.1007/s13534-011-0015-x

64. Prengel HG, Santhanam AT, Penich RM, Jindal PC, Wendt KH. Advanced PVD-TiAlN coatings on carbide and cermet cutting tools. *Surf Coatings Technol*. 1997;94–95:597–602. https://doi.org/https://doi.org/10.1016/S0257-8972(97)00503-3

65. Zhang K, Deng J, Guo XH, Sun L, Lei S. Study on the adhesion and tribological behavior of PVD TiAlN coatings with a multi-scale textured substrate surface. *Int J Refract Met \& Hard Mater*. 2018;72:292–305.

66. Santana AE, Karimi A, Derflinger VH, Schütze A. Thermal treatment effects on microstructure and mechanical properties of TiAlN thin films. *Tribol Lett*. 2004;17(4):689–696. https://doi.org/10.1007/s11249-004-8074-0

67. Staia MH, D'Alessandria M, Quinto DT, Roudet F, Marsal Astort M. High-temperature tribological characterization of commercial TiAlN coatings. *J Phys Condens Matter*. 2006;18(32). https://doi.org/10.1088/0953-8984/18/32/S04

68. Heim D, Hochreiter R. TiAlN and TiAlCN deposition in an industrial PaCVD-plant. *Surf Coatings Technol*. 1998;98(1–3):1553–1556. https://doi.org/10.1016/S0257-8972(97)00303-4

69. Fernandes L, Silva FJG, Alexandre R. Study of TiAlN PVD Coating on Stamping Dies Used in Tinplate Food Package Production. *Micromachines*. 2019;10(3). https://doi.org/10.3390/mi10030182

70. Ait-Djafer AZ, Saoula N, Aknouche H, Guedouar B, Madaoui N. Deposition and characterization of titanium aluminum nitride coatings prepared by RF magnetron sputtering. *Appl Surf Sci*. 2015;350:6–9. https://doi.org/10.1016/j.apsusc.2015.02.053

71. Jehn HA, Hofmann S, Rückborn V, Münz W. Morphology and properties of sputtered (Ti,Al)N layers on high speed steel substrates as a function of deposition temperature and sputtering atmosphere. *J Vac Sci Technol A*. 1986;4(6):2701–2705. https://doi.org/10.1116/1.573709

72. Borodianska H, Ludvinskaya T, Sakka Y, Uvarova I, Vasylkiv O. Bulk Ti1−xAlxN nanocomposite via spark plasma sintering of nanostructured Ti1−xAlxN–AlN powders. *Scr Mater*. 2009;61(11):1020–1023. https://doi.org/https://doi.org/10.1016/j.scriptamat.2009.08.019

73. Radune M, Zinigrad M, Kalabukhov S, Sokol M, Chumanov VI, Frage N. Spark plasma sintering of Ti1−xAlxN nano-powders synthesized by high-energy ball milling. *Ceram Int*. 2016;42(9):11077–11084. https://doi.org/https://doi.org/10.1016/j.ceramint.2016.04.006

74. Radune M, Zinigrad M, Kalabukhov S, Sokol M, Chumanov VI, Frage N. Spark plasma sintering of Ti1-xAlxN nano-powders synthesized by high-energy ball milling. *Ceram Int*. 2016;42(9):11077–11084. https://doi.org/10.1016/j.ceramint.2016.04.006

75. Liu Y, Zhang Y, Zhang H, *et al.* Microstructure and mechanical properties of refractory HfMo0.5NbTiV0.5Sixhigh-entropy composites. *J Alloys Compd*. 2017;694:869–876. https://doi.org/10.1016/j.jallcom.2016.10.014

76. Dong Y, Ren K, Lu Y, Wang Q, Liu J, Wang Y. High-entropy environmental barrier coating for the ceramic matrix composites. *J Eur Ceram Soc*. 2019;39(7):2574–2579. https://doi.org/10.1016/j.jeurceramsoc.2019.02.022

77. Rost CM, Sachet E, Borman T, *et al.* Entropy-stabilized oxides. *Nat Commun*. 2015;6(1):8485. https://doi.org/10.1038/ncomms9485

78. Gild J, Zhang Y, Harrington T, *et al.* High-Entropy Metal Diborides: A New Class of High-Entropy Materials and a New Type of Ultrahigh Temperature Ceramics. *Sci Rep*. 2016;6(1):37946. https://doi.org/10.1038/srep37946

79. Zhang R-Z, Reece MJ. Review of high entropy ceramics: design, synthesis, structure and properties. *J Mater Chem A*. 2019;7(39):22148–22162. https://doi.org/10.1039/C9TA05698J

80. Wright AJ, Luo J. A step forward from high-entropy ceramics to compositionally complex ceramics: a new perspective. *J Mater Sci*. 2020;55(23):9812–9827. https://doi.org/10.1007/s10853-020-04583-w

81. Oses C, Toher C, Curtarolo S. High-entropy ceramics. *Nat Rev Mater*. 2020;5(4):295–309. https://doi.org/10.1038/s41578-019-0170-8

82. Akrami S, Edalati P, Fuji M, Edalati K. High-entropy ceramics: Review of principles, production and applications. *Mater Sci Eng R Reports*. 2021;146(March):100644. https://doi.org/10.1016/j.mser.2021.100644

83. Gild J, Braun J, Kaufmann K, *et al.* A high-entropy silicide: (Mo0.2Nb0.2Ta0.2Ti0.2W0.2)Si2. *J Mater*. 2019;5(3):337–343. https://doi.org/10.1016/j.jmat.2019.03.002

84. Tsai MH, Wang CW, Lai CH, Yeh JW, Gan JY. Thermally stable amorphous (AlMoNbSiTaTiVZr)50 N50 nitride film as diffusion barrier in copper metallization. *Appl Phys Lett*. 2008;92(5). https://doi.org/10.1063/1.2841810

85. Cui M, Yang C, Li B, *et al.* High-Entropy Metal Sulfide Nanoparticles Promise High-Performance Oxygen Evolution Reaction. *Adv Energy Mater*. 2021;11(3):1–8. https://doi.org/10.1002/aenm.202002887

86. Wang Z, Li ZT, Zhao SJ, Wu ZG. High-entropy carbide ceramics: a perspective review. *Tungsten*. 2021;3(2):131–142. https://doi.org/10.1007/s42864-021-00085-7

87. Das S, Durygin A, Cheng Z. High entropy nitride ceramics and methods of synthesizing the same. US11691923B1. 2023.

88. Pierson HO. Handbook of refractory carbides and nitrides: properties, characteristics, processing and applications. William Andrew; 1996

89. Balasubramanian K, Khare S V, Gall D. Valence electron concentration as an indicator for mechanical properties in rocksalt structure nitrides, carbides and carbonitrides. *Acta Mater*. 2018;152:175–185.

90. Sangiovanni DG. Inherent toughness and fracture mechanisms of refractory transition-metal nitrides via density-functional molecular dynamics. *Acta Mater*. 2018;151:11–20. https://doi.org/https://doi.org/10.1016/j.actamat.2018.03.038

91. Moskovskikh D, Vorotilo S, Buinevich V, *et al.* Extremely hard and tough high entropy nitride ceramics. *Sci Rep*. 2020;10(1):1–8. https://doi.org/10.1038/s41598-020-76945-y

92. Dippo OF, Mesgarzadeh N, Harrington TJ, Schrader GD, Vecchio KS. Bulk high-entropy nitrides and carbonitrides. *Sci Rep*. 2020;10(1):1–11. https://doi.org/10.1038/s41598-020-78175-8

93. Dippo OF, Mesgarzadeh N, Harrington TJ, Schrader GD, Vecchio KS. Bulk high-entropy nitrides and carbonitrides. *Sci Rep*. 2020;10(1):21288. https://doi.org/10.1038/s41598-020-78175-8

94. Novikov V, Stepanov N, Zherebtsov S, Salishchev G. Structure and Properties of High-Entropy Nitride Coatings. *Metals (Basel)*. 2022;12(5). https://doi.org/10.3390/met12050847

95. Tsai D-C, Huang Y-L, Lin S-R, Liang S-C, Shieu F-S. Effect of nitrogen flow ratios on the structure and mechanical properties of (TiVCrZrY)N coatings prepared by reactive magnetron sputtering. *Appl Surf Sci*. 2010;257(4):1361–1367. https://doi.org/https://doi.org/10.1016/j.apsusc.2010.08.078

96. Yan XH, Li JS, Zhang WR, Zhang Y. A brief review of high-entropy films. *Mater Chem Phys*. 2018;210:12–19. https://doi.org/https://doi.org/10.1016/j.matchemphys.2017.07.078

97. Liang S-C, Tsai D-C, Chang Z-C, *et al.* Structural and mechanical properties of multi-element (TiVCrZrHf) N coatings by reactive magnetron sputtering. *Appl Surf Sci*. 2011;258(1):399–403.

98. Chang Z-C, Liang S-C, Han S, Chen Y-K, Shieu F-S. Characteristics of TiVCrAlZr multi-element nitride films prepared by reactive sputtering. *Nucl Instruments Methods Phys Res Sect B Beam Interact with Mater Atoms*. 2010;268(16):2504–2509.

99. Pogrebnjak AD, Yakushchenko I V, Bagdasaryan AA, *et al.* Microstructure, physical and chemical properties of nanostructured (Ti–Hf–Zr–V–Nb)N coatings under different deposition conditions. *Mater Chem Phys*. 2014;147(3):1079–1091. https://doi.org/https://doi.org/10.1016/j.matchemphys.2014.06.062

100. Beresnev VM, Sobol' O V, Andreev AA, *et al.* Formation of Superhard State of the TiZrHfNbTaYN Vacuum–Arc High-Entropy Coating. *J Superhard Mater*. 2018;40(2):102–109. https://doi.org/10.3103/S1063457618020041

101. Liang S-C, Chang Z-C, Tsai D-C, *et al.* Effects of substrate temperature on the structure and mechanical properties of (TiVCrZrHf)N coatings. *Appl Surf Sci*. 2011;257(17):7709–7713. https://doi.org/https://doi.org/10.1016/j.apsusc.2011.04.014

102. Pogrebnjak AD, Yakushchenko I V, Abadias G, *et al.* The effect of the deposition parameters of nitrides of high-entropy alloys (TiZrHfVNb)N on their structure, composition, mechanical and tribological properties. *J Superhard Mater*. 2013;35(6):356–368. https://doi.org/10.3103/S106345761306004X

103. Shen WJ, Tsai MH, Tsai KY, *et al.* Superior Oxidation Resistance of (Al0.34Cr0.22Nb0.11Si0.11Ti0.22)50N50 High-Entropy Nitride. *J Electrochem Soc*. 2013;160(11):C531. https://doi.org/10.1149/2.028311jes

104. Firstov SA, Gorban' VF, Danilenko NI, Karpets M V, Andreev AA, Makarenko ES. Thermal Stability of Superhard Nitride Coatings from High-Entropy Multicomponent Ti–V–Zr–Nb–Hf Alloy. *Powder Metall Met Ceram*. 2014;52(9):560–566. https://doi.org/10.1007/s11106-014-9560-z

105. Sobol O. Structure and properties of high-entropy alloys based on refractory metals. *Mater Today Proc*. 2020;30:736–741.

106. Xing J, Foroughi P, Mondal S, Sun S, Cheng Z. Facile and economical routes toward novel high-entropy metal nitride high-temperature ceramic nanograin powders. *MRS Commun*. 2022;12(2):183–187. https://doi.org/10.1557/s43579-022-00159-8

107. Zhao L, Sun X, Zeng X, *et al.* Synthesis of a new class of high-entropy nitride ceramics and the effects of nitrogen vacancies on their magnetic properties. *Appl Surf Sci*. 2023;618(November 2022):156543. https://doi.org/10.1016/j.apsusc.2023.156543

108. Jin T, Sang X, Unocic RR, *et al.* Mechanochemical-Assisted Synthesis of High-Entropy Metal Nitride via a Soft Urea Strategy. *Adv Mater*. 2018;30(23):1707512. https://doi.org/https://doi.org/10.1002/adma.201707512

109. Moskovskikh D, Vorotilo S, Buinevich V, *et al.* Extremely hard and tough high entropy nitride ceramics. *Sci Rep*. 2020;10(1):19874. https://doi.org/10.1038/s41598-020-76945-y

110. Yao F-Z, Yuan Q, Wang Q, Wang H. Multiscale structural engineering of dielectric ceramics for energy storage applications: from bulk to thin films. *Nanoscale*. 2020;12(33):17165–17184. https://doi.org/10.1039/D0NR04479B

111. Oghbaei M, Mirzaee O. Microwave versus conventional sintering: A review of fundamentals, advantages and applications. *J Alloys Compd*. 2010;494(1):175–189. https://doi.org/https://doi.org/10.1016/j.jallcom.2010.01.068

112. Guillon O, Gonzalez-Julian J, Dargatz B, *et al.* Field-Assisted Sintering Technology/Spark Plasma Sintering: Mechanisms, Materials, and Technology Developments. *Adv Eng Mater*. 2014;16(7):830–849. https://doi.org/https://doi.org/10.1002/adem.201300409

113. Cologna M, Prette ALG, Raj R. Flash-Sintering of Cubic Yttria-Stabilized Zirconia at 750°C for Possible Use in SOFC Manufacturing. *J Am Ceram Soc*. 2011;94(2):316–319. https://doi.org/10.1111/J.1551-2916.2010.04267.X

114. Cologna M, Rashkova B, Raj R. Flash Sintering of Nanograin Zirconia in <5 s at 850°C. *J Am Ceram Soc*. 2010;93(11):3556–3559. https://doi.org/https://doi.org/10.1111/j.1551-2916.2010.04089.x

115. Biesuz M, Sglavo VM. Flash sintering of ceramics. *J Eur Ceram Soc*. 2019;39(2–3):115–143. https://doi.org/10.1016/J.JEURCERAMSOC.2018.08.048

116. Dong Y, Chen I-W. Onset Criterion for Flash Sintering. *J Am Ceram Soc*. 2015;98(12):3624–3627. https://doi.org/https://doi.org/10.1111/jace.13866

117. Yu M, Grasso S, Mckinnon R, Saunders T, Reece MJ. Review of flash sintering: materials, mechanisms and modelling. *Adv Appl Ceram*. 2017;116(1):24–60. https://doi.org/10.1080/17436753.2016.1251051

118. Dancer CEJ. Flash sintering of ceramic materials. *Mater Res Express*. 2016;3(10):102001. https://doi.org/10.1088/2053-1591/3/10/102001

119. Perez-Maqueda LA, Gil-Gonzalez E, Perejon A, Lebrun J-M, Sanchez-Jimenez PE, Raj R. Flash sintering of highly insulating nanostructured phase-pure BiFeO3. *J Am Ceram Soc*. 2017;100(8):3365–3369. https://doi.org/https://doi.org/10.1111/jace.14990

120. Shomrat N, Baltianski S, Randall CA, Tsur Y. Flash sintering of potassium-niobate. *J Eur Ceram Soc*. 2015;35(7):2209–2213. https://doi.org/https://doi.org/10.1016/j.jeurceramsoc.2015.01.017

121. Liu D, Gao Y, Liu J, *et al.* SiC whisker reinforced ZrO2 composites prepared by flash-sintering. *J Eur Ceram Soc*. 2016;36(8):2051–2055. https://doi.org/https://doi.org/10.1016/j.jeurceramsoc.2016.02.014

122. Francis JSC. A study on the phenomena of flash-sintering with tetragonal zirconia. University of Colorado at Boulder PP - United States -- Colorado; United States -- Colorado; 2013

123. Jha SK, Raj R. Electric Fields Obviate Constrained Sintering. *J Am Ceram Soc*. 2014;97(10):3103–3109. https://doi.org/https://doi.org/10.1111/jace.13136

124. Francis JSC, Cologna M, Montinaro D, Raj R. Flash Sintering of Anode–Electrolyte Multilayers for SOFC Applications. *J Am Ceram Soc*. 2013;96(5):1352–1354. https://doi.org/https://doi.org/10.1111/jace.12330

125. Zhou H, Li X, Zhu Y, *et al.* Review of flash sintering with strong electric field. *High Volt*. 2022;7(1):1–11. https://doi.org/10.1049/HVE2.12080

126. Todd RI, Zapata-Solvas E, Bonilla RS, Sneddon T, Wilshaw PR. Electrical characteristics of flash sintering: thermal runaway of Joule heating. *J Eur Ceram Soc*. 2015;35(6):1865–1877. https://doi.org/https://doi.org/10.1016/j.jeurceramsoc.2014.12.022

127. Du Y, Stevenson AJ, Vernat D, Diaz M, Marinha D. Estimating Joule heating and ionic conductivity during flash sintering of 8YSZ. *J Eur Ceram Soc*. 2016;36(3):749–759. https://doi.org/https://doi.org/10.1016/j.jeurceramsoc.2015.10.037

128. Naik K, Jha SK, Raj R. Correlations between conductivity, electroluminescence and flash sintering. *Scr Mater*. 2016;118:1–4. https://doi.org/https://doi.org/10.1016/j.scriptamat.2016.03.001

129. M'Peko J-C, Francis JSC, Raj R. Impedance Spectroscopy and Dielectric Properties of Flash Versus Conventionally Sintered Yttria-Doped Zirconia Electroceramics Viewed at the Microstructural Level. *J Am Ceram Soc*. 2013;96(12):3760–3767. https://doi.org/https://doi.org/10.1111/jace.12567

130. Grasso S, Saunders T, Porwal H, Milsom B, Tudball A, Reece M. Flash Spark Plasma Sintering (FSPS) of α and β SiC. *J Am Ceram Soc*. 2016;99(5):1534–1543. https://doi.org/https://doi.org/10.1111/jace.14158

131. Grasso S, Kim E-Y, Saunders T, *et al.* Ultra-Rapid Crystal Growth of Textured SiC Using Flash Spark Plasma Sintering Route. *Cryst Growth Des*. 2016;16(4):2317–2321. https://doi.org/10.1021/acs.cgd.6b00099

132. Zapata-Solvas E, Bonilla S, Wilshaw PR, Todd RI. Preliminary investigation of flash sintering of SiC. *J Eur Ceram Soc*. 2013;33(13):2811–2816. https://doi.org/https://doi.org/10.1016/j.jeurceramsoc.2013.04.023

133. Niu B, Zhang F, Zhang J, Ji W, Wang W, Fu Z. Ultra-fast densification of boron carbide by flash spark plasma sintering. *Scr Mater*. 2016;116:127–130. https://doi.org/https://doi.org/10.1016/j.scriptamat.2016.02.012

134. Gil-González E, Perejón A, Sánchez-Jiménez PE, Sayagués MJ, Raj R, Pérez-Maqueda LA. Phase-pure BiFeO3 produced by reaction flash-sintering of Bi2O3 and Fe2O3. *J Mater Chem A*. 2018;6(13):5356–5366. https://doi.org/10.1039/C7TA09239C

135. Jesus LM, Silva RS, Raj R, M'Peko J-C. Electric field-assisted ultrafast synthesis of nanopowders: a novel and cost-efficient approach. *RSC Adv*. 2016;6(109):107208–107213. https://doi.org/10.1039/C6RA18734J

136. Jha SK, Lebrun JM, Raj R. Phase transformation in the alumina–titania system during flash sintering experiments. *J Eur Ceram Soc*. 2016;36(3):733–739. https://doi.org/https://doi.org/10.1016/j.jeurceramsoc.2015.10.006

137. Belisario J, Mondal S, Khakpour I, Franco Hernandez A, Durygin A, Cheng Z. Synthesis and flash sintering of (Hf1-xZrx)B2 solid solution powders. *J Eur Ceram Soc*. 2021;41(4):2215–2225. https://doi.org/10.1016/j.jeurceramsoc.2020.12.015

138. Eskandariyun A, Das S, Dubois D, *et al.* Effects of processing conditions on flash sintering of commercial ZrN. *J Am Ceram Soc*. 2024;2(August 2023):1–16. https://doi.org/10.1111/jace.19719

139. Mondal S, Durygin A, Drozd V, Belisario J, Cheng Z. Multicomponent bulk metal nitride (Nb1/3Ta1/3Ti1/3)N1−δ synthesis via reaction flash sintering and characterizations. *J Am Ceram Soc*. 2020;103(9):4876–4893. https://doi.org/10.1111/jace.17226

140. Ma B, Zhu Y, Wang K, Sun Z, Ren K, Wang Y. Reactive flash sintering and electrical transport properties of high-entropy (MgCoNiCuZn)1-xLixO oxides. *J Am Ceram Soc*. 2022;105(6):3765–3773. https://doi.org/https://doi.org/10.1111/jace.18343

141. Liu J, Ren K, Ma C, Du H, Wang Y. Dielectric and energy storage properties of flash-sintered high-entropy (Bi0.2Na0.2K0.2Ba0.2Ca0.2)TiO3 ceramic. *Ceram Int*. 2020;46(12):20576–20581. https://doi.org/https://doi.org/10.1016/j.ceramint.2020.05.090

142. Kumar A, Sharma G, Aftab A, Ahmad MI. Flash assisted synthesis and densification of five component high entropy oxide (Mg, Co, Cu, Ni, Zn)O at 350 °C in 3 min. *J Eur Ceram Soc*. 2020;40(8):3358–3362. https://doi.org/https://doi.org/10.1016/j.jeurceramsoc.2020.02.036

143. Liu D, Peng X, Liu J, Chen L, Yang Y, An L. Ultrafast synthesis of entropy-stabilized oxide at room temperature. *J Eur Ceram Soc*. 2020;40(6):2504–2508. https://doi.org/https://doi.org/10.1016/j.jeurceramsoc.2020.01.018

144. Abstracts C, Registry S. Physical Constants of Inorganic Compounds. *CRC Handb Chem Phys*. 2021.

145. D. Pilloud , A.S. Dehlinger , J.F. Pierson *, A. Roman , L. Pichon aa a A, ACentre. Reactively sputtered zirconium nitride coatings: structural, mechanical, optical and electrical characteristics. *Surf Coatings Technol*. 1997;97(1):719–722. https://doi.org/10.1016/S0257-8972Ž03.00613-3

146. Sue JA, Chang TP. Friction and wear behavior of titanium nitride, zirconium nitride and chromium nitride coatings at elevated temperatures. *Surf Coatings Technol*. 1995;76–77:61–69. https://doi.org/10.1016/0257-8972(95)02506-5

147. Chang YY, Wu CJ. Mechanical properties and impact resistance of multilayered TiAlN/ZrN coatings. *Surf Coatings Technol*. 2013;231:62–66. https://doi.org/10.1016/j.surfcoat.2012.03.013

148. Tian W, Wang P, Zhang G, Kan Y, Li Y. Mechanical Properties of Cr 2 AlC Ceramics. *J Am Ceram Soc*. 2007;90(5):1663–1666. https://doi.org/10.1111/j.1551-2916.2007.01634.x

149. Manaud JP, Poulon A, Gomez S, Petitcorps Y Le. A comparative study of CrN, ZrN, NbN and TaN layers as cobalt diffusion barriers for CVD diamond deposition on WC-Co tools. *Surf Coatings Technol*. 2007;202(2):222–231. https://doi.org/10.1016/j.surfcoat.2007.05.024

150. Schwarz K, Williams A, Cuomo J. Zirconium nitride a new material for Josephson junctions. *Phys Rev B*. 1985;32(12):8312–8316. https://doi.org/https://doi.org/10.1103/PhysRevB.32.8312

151. Wu M, Lin X, Wang Y, *et al.* Economical Pt-free catalysts for counter electrodes of dye-sensitized solar cells. *J Am Chem Soc*. 2012;134(7):3419–3428. https://doi.org/10.1021/ja209657v

152. Cui Z, Zu C, Zhou W, Manthiram A, Goodenough JB. Mesoporous Titanium Nitride-Enabled Highly Stable Lithium-Sulfur Batteries. *Adv Mater*. 2016;28(32):6926–6931. https://doi.org/10.1002/adma.201601382

153. Yang P, Chao D, Zhu C, *et al.* Ultrafast-charging supercapacitors based on corn-like titanium nitride nanostructures. *Adv Sci*. 2015;3(6):1–7. https://doi.org/10.1002/advs.201500299

154. Gao Z, Chen Y, Kulczyk-Malecka J, *et al.* Comparison of the oxidation behavior of a zirconium nitride coating in water vapor and air at high temperature. *Corros Sci*. 2018;138(May 2017):242–251. https://doi.org/10.1016/j.corsci.2018.04.015

155. Yin XW, Cheng LF, Zhang LT, Travitzky N, Greil P. Fibre-reinforced multifunctional SiC matrix composite materials. *Int Mater Rev*. 2017;62(3):117–172. https://doi.org/10.1080/09506608.2016.1213939

156. Tang Y, Zhang GJ, Xue JX, Wang XG, Xu CM, Huang X. Densification and mechanical properties of hot-pressed ZrN ceramics doped with Zr or Ti. *J Eur Ceram Soc*. 2013;33(7):1363–1371. https://doi.org/10.1016/j.jeurceramsoc.2012.12.013

157. Alexandre N, Desmaison-Brut M, Valin F, Boncoeur M. Mechanical properties of hot isostatically pressed zirconium nitride materials. *J Mater Sci*. 1993;28(9):2385–2390. https://doi.org/10.1007/BF01151669

158. Lee G, Olevsky EA, Manière C, *et al.* Effect of electric current on densification behavior of conductive ceramic powders consolidated by spark plasma sintering. *Acta Mater*. 2018;144:524–533. https://doi.org/10.1016/j.actamat.2017.11.010

159. Lee G, Yurlova MS, Giuntini D, *et al.* Densification of zirconium nitride by spark plasma sintering and high voltage electric discharge consolidation: A comparative analysis. *Ceram Int*. 2015;41(10):14973–14987. https://doi.org/10.1016/j.ceramint.2015.08.042

160. Pshenichnaya O V., Kuzenkova MA, Kislyi PS. The sintering of zirconium nitride in vacuum and in nitrogen. *Sov Powder Metall Met Ceram*. 1975;14(12):986–989. https://doi.org/10.1007/BF00807873

161. Montes JM, Rodríguez JA, Cuevas FG, Cintas J. Consolidation by electrical resistance sintering of Ti powder. *J Mater Sci*. 2011;46(15):5197–5207. https://doi.org/10.1007/s10853-011-5456-1

162. Montes JM, Cuevas FG, Cintas J, Urban P. A One-Dimensional Model of the Electrical Resistance Sintering Process. *Metall Mater Trans A Phys Metall Mater Sci*. 2015;46(2):963–980. https://doi.org/10.1007/s11661-014-2643-0

163. Lagos MA, Agote I, Schubert T, *et al.* Development of electric resistance sintering process for the fabrication of hard metals: Processing, microstructure and mechanical properties. *Int J Refract Met Hard Mater*. 2017;66:88–94. https://doi.org/10.1016/j.ijrmhm.2017.03.005

164. Mazo I, Molinari A, Sglavo VM. Electrical Resistance Flash Sintering of Tungsten Carbide. *Mater Des*. 2021;213:110330. https://doi.org/10.1016/j.matdes.2021.110330

165. Kathuria YP. Laser surface nitriding of yttria stabilized tetragonal zirconia. *Surf Coatings Technol*. 2007;201(12):5865–5869. https://doi.org/10.1016/j.surfcoat.2006.10.041

166. Sun W, Bartel CJ, Arca E, *et al.* A map of the inorganic ternary metal nitrides. *Nat Mater*. 2019;18(7):732–739. https://doi.org/10.1038/s41563-019-0396-2

167. Bouamama K, Djemia P, Benhamida M. First-principles calculation of the structural and elastic properties of ternary metal nitrides TaxMo1-xN and TaxW1-xN. *J Phys Conf Ser*. 2015;640(1). https://doi.org/10.1088/1742-6596/640/1/012022

168. Abadias G, Koutsokeras LE, Siozios A, Patsalas P. Stress, phase stability and oxidation resistance of ternary Ti-Me-N (Me = Zr, Ta) hard coatings. *Thin Solid Films*. 2013;538:56–70. https://doi.org/10.1016/j.tsf.2012.10.119

169. Sudipta Seal. Transition Metal Nitride Functional Coatings. *Funct Coatings*. 2001;(ii):51–54.

170. Roldán MA, Alcalá MD, Real C. Characterisation of ternary TixV1-xNy nitride prepared by mechanosynthesis. *Ceram Int*. 2012;38(1):687–693. https://doi.org/10.1016/j.ceramint.2011.07.057

171. Rogström L, Ullbrand J, Almer J, Hultman L, Jansson B, Odén M. Strain evolution during spinodal decomposition of TiAlN thin films. *Thin Solid Films*. 2012;520(17):5542–5549. https://doi.org/10.1016/j.tsf.2012.04.059

172. Ran Y, Lu H, Zhao S, *et al.* Structural and plasmonic properties of Ti x Zr 1−x N y ternary nitride thin films. *Appl Surf Sci*. 2019;476(November 2018):560–568. https://doi.org/10.1016/j.apsusc.2019.01.108

173. Keckes J, Daniel R, Mitterer C, *et al.* Self-organized periodic soft-hard nanolamellae in polycrystalline TiAlN thin films. *Thin Solid Films*. 2013;545:29–32. https://doi.org/10.1016/j.tsf.2013.08.001

174. Ran Y, Lu H, Zhao S, *et al.* Effects of substrate bias and temperature on the structure and dielectric properties of TixZr1−xNy ternary nitride thin films. *Surf Coatings Technol*. 2019;359(November 2018):258–264. https://doi.org/10.1016/j.surfcoat.2018.12.023

175. Meng QN, Wen M, Qu CQ, Hu CQ, Zheng WT. Preferred orientation, phase transition and hardness for sputtered zirconium nitride films grown at different substrate biases. *Surf Coatings Technol*. 2011;205(8–9):2865–2870. https://doi.org/10.1016/j.surfcoat.2010.10.060

176. He JL, Setsuhara Y, Shimizu I, Miyake S. Structure refinement and hardness enhancement of titanium nitride films by addition of copper. *Surf Coatings Technol*. 2001;137(1):38–42. https://doi.org/10.1016/S0257-8972(00)01089-6

177. Tung HM, Wu PH, Yu GP, Huang JH. Microstructures, mechanical properties and oxidation behavior of vacuum annealed TiZrN thin films. *Vacuum*. 2015;115:12–18. https://doi.org/10.1016/j.vacuum.2015.01.029

178. Chim YC, Ding XZ, Zeng XT, Zhang S. Oxidation resistance of TiN, CrN, TiAlN and CrAlN coatings deposited by lateral rotating cathode arc. *Thin Solid Films*. 2009;517(17):4845–4849. https://doi.org/10.1016/j.tsf.2009.03.038

179. Mayrhofer PH, Hörling A, Karlsson L, *et al.* Self-organized nanostructures in the Ti-Al-N system. *Appl Phys Lett*. 2003;83(10):2049–2051. https://doi.org/10.1063/1.1608464

180. Liu MWJ, Huang JH. Effect of coating architecture on stress and energy relief efficiency of TiZrN coating on Si substrate. *Thin Solid Films*. 2022;751(December 2021):139219. https://doi.org/10.1016/j.tsf.2022.139219

181. Sharifi Malvajerdi S, Sharifi Malvajerdi A, Ghanaatshoar M, Habibi M, Jahdi H. TiCrN-TiAlN-TiAlSiN-TiAlSiCN multi-layers utilized to increase tillage tools useful lifetime. *Sci Rep*. 2019;9(1):1–12. https://doi.org/10.1038/s41598-019-55677-8

182. Huang JY, Tang LC, Lee MH. Ab initio study of the structural and optical properties of orthorhombic ternary nitride crystals. *J Phys Condens Matter*. 2001;13(46):10417–10431. https://doi.org/10.1088/0953-8984/13/46/312

183. Ammari Y, Hlil EK. Ab initio calculation of electronic and optical properties of CaNiN nitride and the signature of topological properties. *Chem Pap*. 2021;75(7):3197–3205. https://doi.org/10.1007/s11696-021-01543-9

184. Zhou J, Zhang L, Chen L, Du Y, Liu ZK. A thermodynamic description of metastable C-TiAlZrN coatings with triple spinodally decomposed domains. *J Min Metall Sect B Metall*. 2017;53(2):85–93. https://doi.org/10.2298/JMMB161017001Z

185. Zhou J, Zhong J, Chen L, *et al.* Phase equilibria, thermodynamics and microstructure simulation of metastable spinodal decomposition in c–Ti1−xAlxN coatings. *Calphad*. 2017;56(October 2016):92–101. https://doi.org/10.1016/j.calphad.2016.12.006

186. Cologna M, Rashkova B, Raj R. Flash sintering of nanograin zirconia in <5 s at 850°C. *J Am Ceram Soc*. 2010;93(11):3556–3559. https://doi.org/10.1111/j.1551-2916.2010.04089.x

187. Raj R. Joule heating during flash-sintering. *J Eur Ceram Soc*. 2012;32(10):2293–2301. https://doi.org/10.1016/j.jeurceramsoc.2012.02.030

188. Todd RI, Zapata-Solvas E, Bonilla RS, Sneddon T, Wilshaw PR. Electrical characteristics of flash sintering: Thermal runaway of Joule heating. *J Eur Ceram Soc*. 2015;35(6):1865–1877. https://doi.org/10.1016/j.jeurceramsoc.2014.12.022

189. Dong Y, Chen IW. Onset Criterion for Flash Sintering. *J Am Ceram Soc*. 2015;98(12):3624–3627. https://doi.org/10.1111/jace.13866

190. Zhang Y, Jung J Il, Luo J. Thermal runaway, flash sintering and asymmetrical microstructural development of ZnO and ZnO-Bi2O3 under direct currents. *Acta Mater*. 2015;94:87–100. https://doi.org/10.1016/j.actamat.2015.04.018

191. Avila V, Yoon B, Ingraci Neto RR, *et al.* Reactive flash sintering of the complex oxide Li0.5La0.5TiO3 starting from an amorphous precursor powder. *Scr Mater*. 2020;176:78–82. https://doi.org/10.1016/j.scriptamat.2019.09.037

192. Yoon B, Avila V, Raj R, Jesus LM. Reactive flash sintering of the entropy-stabilized oxide Mg0.2Ni0.2Co0.2Cu0.2Zn0.2O. *Scr Mater*. 2020;181(3):48–52. https://doi.org/10.1016/j.scriptamat.2020.02.006

193. Taibi A, Chaguetmi S, Sánchez-Jiménez PE, *et al.* Pure perovskite BiFeO3–BaTiO3 ceramics prepared by reaction flash sintering of Bi2O3–Fe2O3–BaTiO3 mixed powders. *Ceram Int*. 2021;47(19):26947–26954. https://doi.org/10.1016/j.ceramint.2021.06.108

194. Eva Gil-González, Antonio Perejón, Pedro E. Sánchez-Jiménez, María J. Sayagués, Rishi Raj LAP-M. Phase-pure BiFeO3 produced by reaction flash-sintering of BiO3 and Fe2O3. *J Mater Chem A*. 2018;6:5356–5366.

195. Lengauer W. Properties of bulk δ-TiN1-x prepared by nitrogen diffusion into titanium metal. *J Alloys Compd*. 1992;186(2):293–307. https://doi.org/10.1016/0925-8388(92)90016-3

196. Dauchot JP, Gouttebaron R, Wautelet M, Hecq M. Rapid growth of hard and compact layers of stoichiometric ZrN by DC reactive magnetron sputtering pulsed at low frequency. *Adv Eng Mater*. 2000;2(12):824–827. https://doi.org/10.1002/1527-2648(200012)2:12<824::AID-ADEM824>3.0.CO;2-I

197. Harrison RW, Lee WE. Processing and properties of ZrC, ZrN and ZrCN ceramics: a review. *Adv Appl Ceram*. 2016;115(5):294–307. https://doi.org/10.1179/1743676115Y.0000000061

198. Mohammadpour E, Altarawneh M, Al-Nu'airat J, Jiang ZT, Mondinos N, Dlugogorski BZ. Thermo-mechanical properties of cubic titanium nitride. *Mol Simul*. 2018;44(5):415–423. https://doi.org/10.1080/08927022.2017.1393810

199. Charalambous H, Jha SK, Okasinski J, Tsakalakos T. Spectral analysis and temperature measurement during flash sintering under AC electric field. *Materialia*. 2019;6(February):100273. https://doi.org/10.1016/j.mtla.2019.100273

200. Terauds K, Lebrun JM, Lee HH, *et al.* Electroluminescence and the measurement of temperature during Stage III of flash sintering experiments. *J Eur Ceram Soc*. 2015;35(11):3195–3199. https://doi.org/10.1016/j.jeurceramsoc.2015.03.040

201. Perez-Maqueda LA, Gil-Gonzalez E, Wassel MA, *et al.* Insight into the BiFeO3 flash sintering process by in-situ energy dispersive X-ray diffraction (ED-XRD). *Ceram Int*. 2019;45(2):2828–2834. https://doi.org/10.1016/j.ceramint.2018.07.293

202. Jha SK, Charalambous H, Wang H, *et al.* In-situ observation of oxygen mobility and abnormal lattice expansion in ceria during flash sintering. *Ceram Int*. 2018;44(13):15362–15369. https://doi.org/10.1016/j.ceramint.2018.05.186

203. Charalambous H, Jha SK, Lay RT, Cabales A, Okasinski J, Tsakalakos T. Investigation of temperature approximation methods during flash sintering of ZnO. *Ceram Int*. 2018;44(6):6162–6169. https://doi.org/10.1016/j.ceramint.2017.12.250

204. Charalambous H, Jha SK, Phuah XL, *et al.* In situ measurement of temperature and reduction of rutile titania using energy dispersive x-ray diffraction. *J Eur Ceram Soc*. 2018;38(16):5503–5511. https://doi.org/10.1016/j.jeurceramsoc.2018.08.032

205. Zhou J, Zhong J, Chen L, *et al.* Phase equilibria, thermodynamics and microstructure simulation of metastable spinodal decomposition in c–Ti1−xAlxN coatings. *Calphad*. 2017;56(December 2016):92–101. https://doi.org/10.1016/j.calphad.2016.12.006

206. Kuwahara H, Mazaki N, Takahashi M, Watanabe T, Yang X, Aizawa T. Mechanical properties of bulk sintered titanium nitride ceramics. *Mater Sci Eng A*. 2001;319–321:687–691. https://doi.org/10.1016/S0921-5093(01)00936-4

207. Lin YW, Huang JH, Yu GP. Effect of nitrogen flow rate on properties of nanostructured TiZrN thin films produced by radio frequency magnetron sputtering. *Thin Solid Films*. 2010;518(24):7308–7311. https://doi.org/10.1016/j.tsf.2010.04.099

208. Santana AE, Karimi A, Derflinger VH, Schütze A. Relating hardness-curve shapes with deformation mechanisms in TiAlN thin films enduring indentation. *Mater Sci Eng A*. 2005;406(1–2):11–18. https://doi.org/10.1016/j.msea.2005.06.010

209. Quinn GD. Fracture Toughness of Ceramics by the Vickers Indentation Crack Length Method: A Critical Review. 2008;45–62. https://doi.org/10.1002/9780470291313.ch5

210. Russias J, Cardinal S, Fontaine J, Fantozzi G, Esnouf C, Bienvenu K. Bulk titanium nitride material obtained from SHS starting powder: Densification, mechanical characterization and tribological approach. *Int J Refract Met Hard Mater*. 2005;23(4-6 SPEC. ISS.):344–349. https://doi.org/10.1016/j.ijrmhm.2005.05.013

211. Mondal S, Durygin A, Drozd V, Belisario J, Cheng Z. Multicomponent bulk metal nitride (Nb 1/3 Ta 1/3 Ti 1/3)N 1− δ synthesis via reaction flash sintering and characterizations. *J Am Ceram Soc*. 2020;103(9):4876–4893. https://doi.org/10.1111/jace.17226

212. Wu S, Wu S, Zhang G, Zhang W. Hardness and elastic modulus of titanium nitride coatings prepared by pirac method. *Surf Rev Lett*. 2018;25(1):1–8. https://doi.org/10.1142/S0218625X18500403

213. Mei AB, Howe BM, Zhang C, *et al.* Physical properties of epitaxial ZrN/MgO(001) layers grown by reactive magnetron sputtering. *J Vac Sci Technol A Vacuum, Surfaces, Film*. 2013;31(6). https://doi.org/10.1116/1.4825349

214. James F, Shackelford EJF, Alexander W. Material Science & Engineering Handbook. 2001

215. Yeh JW, Chen SK, Lin SJ, *et al.* Nanostructured high-entropy alloys with multiple principal elements: Novel alloy design concepts and outcomes. *Adv Eng Mater*. 2004;6(5):299–303. https://doi.org/10.1002/adem.200300567

216. Cantor B, Chang ITH, Knight P, Vincent AJB. Microstructural development in equiatomic multicomponent alloys. *Mater Sci Eng A*. 2004;375–377(1-2 SPEC. ISS.):213–218. https://doi.org/10.1016/j.msea.2003.10.257

217. Tsai MH, Yeh JW. High-entropy alloys: A critical review. *Mater Res Lett*. 2014;2(3):107–123. https://doi.org/10.1080/21663831.2014.912690

218. Yeh JW. Recent progress in high-entropy alloys. *Ann Chim Sci des Mater*. 2006;31(6):633–648. https://doi.org/10.3166/acsm.31.633-648

219. Ye YF, Wang Q, Lu J, Liu CT, Yang Y. High-entropy alloy: challenges and prospects. *Mater Today*. 2016;19(6):349–362. https://doi.org/10.1016/j.mattod.2015.11.026

220. Chen TK, Shun TT, Yeh JW, Wong MS. Nanostructured nitride films of multi-element high-entropy alloys by reactive DC sputtering. *Surf Coatings Technol*. 2004;188–189(1-3 SPEC.ISS.):193–200. https://doi.org/10.1016/j.surfcoat.2004.08.023

221. Chen TK, Wong MS, Shun TT, Yeh JW. Nanostructured nitride films of multi-element high-entropy alloys by reactive DC sputtering. *Surf Coatings Technol*. 2005;200(5–6):1361–1365. https://doi.org/10.1016/j.surfcoat.2005.08.081

222. Chang X, Zeng M, Liu K, Fu L. Phase Engineering of High-Entropy Alloys. *Adv Mater*. 2020;32(14):1–22. https://doi.org/10.1002/adma.201907226

223. Tsai C-W, Lai S-W, Cheng K-H, *et al.* Strong amorphization of high-entropy AlBCrSiTi nitride film. *Thin Solid Films*. 2012;520(7):2613–2618. https://doi.org/https://doi.org/10.1016/j.tsf.2011.11.025

224. Shen WJ, Tsai MH, Tsai KY, *et al.* Superior Oxidation Resistance of (Al 0.34 Cr 0.22 Nb 0.11 Si 0.11 Ti 0.22) 50 N 50 High-Entropy Nitride . *J Electrochem Soc*. 2013;160(11):C531–C535. https://doi.org/10.1149/2.028311jes

225. Wen T, Ye B, Nguyen MC, Ma M, Chu Y. Thermophysical and mechanical properties of novel high-entropy metal nitride-carbides. *J Am Ceram Soc*. 2020;103(11):6475–6489. https://doi.org/10.1111/jace.17333

226. Belisario J, Mondal S, Khakpour I, Franco Hernandez A, Durygin A, Cheng Z. Synthesis and flash sintering of (Hf1-xZrx)B2 solid solution powders. *J Eur Ceram Soc*. 2021;41(4):2215–2225. https://doi.org/10.1016/j.jeurceramsoc.2020.12.015

227. Das S, Durygin A, Drozd V, Sozal MSI, Cheng Z. Reactive flash sintering of TiZrN and TiAlN ternary metal nitrides. *J Eur Ceram Soc*. 2024;44(4):2037–2051. https://doi.org/https://doi.org/10.1016/j.jeurceramsoc.2023.11.079

228. Lifshin E. Handbook of Ceramic Hard Materials. 2001

229. Gao L, Li S, Han T, *et al.* Microstructure, properties and fracture mechanism of MAX phase Ti3AlC2 ceramics with Si doping via Ti–Al–C system by powder metallurgy. *J Mater Res Technol*. 2021;15:3663–3672. https://doi.org/https://doi.org/10.1016/j.jmrt.2021.10.012

230. Pfeiler M, Scheu C, Hutter H, *et al.* On the effect of Ta on improved oxidation resistance of Ti–Al–Ta–N coatings. *J Vac Sci Technol A*. 2009;27(3):554–560. https://doi.org/10.1116/1.3119671

231. Pravica M, Bhattacharya N, Liu Y, *et al.* High pressure infrared and X-ray Raman studies of aluminum nitride. *Phys Status Solidi Basic Res*. 2013;250(4):726–731. https://doi.org/10.1002/pssb.201200485

232. Zhao JG, Yang LX, Yu Y, *et al.* Isostructural phase transition of TiN under high pressure. *Chinese Phys Lett*. 2005;22(5):1199–1201. https://doi.org/10.1088/0256-307X/22/5/048

233. Cheng P, Ye T, Zeng H, Ding J. Raman spectra investigation on the pressure-induced phase transition in titanium nitride (TiN). *AIP Adv*. 2020;10(4). https://doi.org/10.1063/1.5128882

234. Xiang T, Cai Z, Du P, Li K, Zhang Z, Xie G. Dual phase equal-atomic NbTaTiZr high-entropy alloy with ultra-fine grain and excellent mechanical properties fabricated by spark plasma sintering. *J Mater Sci Technol*. 2021;90:150–158. https://doi.org/https://doi.org/10.1016/j.jmst.2021.03.024

235. Koželj P, Vrtnik S, Jelen A, *et al.* Discovery of a Superconducting High-Entropy Alloy. *Phys Rev Lett*. 2014;113(10):107001. https://doi.org/10.1103/PhysRevLett.113.107001

236. Poole CP, Farach HA, Creswick RJ, Prozorov R. Superconductivity. *Superconductivity*. 2007;35(1961). https://doi.org/10.1016/B978-0-12-088761-3.X5021-2

237. Zou Y, Qi X, Zhang C, *et al.* Discovery of superconductivity in hard hexagonal ϵ-NbN. *Sci Rep*. 2016;6(February):1–9. https://doi.org/10.1038/srep22330

238. Müller M, Hoepfl R, Liensberger L, *et al.* Growth optimization of TaN for superconducting spintronics. *Mater Quantum Technol*. 2021;1(4). https://doi.org/10.1088/2633-4356/AC2E14

239. Kalok D, Bilušić A, Baturina TI, *et al.* Non-linear conduction in the critical region of the superconductor- insulator transition in TiN thin films. *J Phys Conf Ser*. 2012;400(PART 2). https://doi.org/10.1088/1742-6596/400/2/022042

240. Yonenaga I. Hardness of bulk single-crystal GaN and AlN. *MRS Internet J Nitride Semicond Res*. 2020;7(1):6. https://doi.org/10.1557/S1092578300000326

241. Wei S, Xie Z, Xue W, Yi Z, Chen J, Cheng L. Fracture toughness of aluminum nitride ceramics at cryogenic temperatures. *Ceram Int*. 2014;40(8, Part B):13715–13718. https://doi.org/https://doi.org/10.1016/j.ceramint.2014.05.012

242. Chen X-J, Struzhkin V V, Wu Z, *et al.* Hard superconducting nitrides. *Proc Natl Acad Sci*. 2005;102(9):3198–3201. https://doi.org/10.1073/pnas.0500174102

243. Müllauer L. Screening for intrinsically hard and tough ceramic-like materials. 2019. https://doi.org/https://doi.org/10.34726/hss.2019.57382

244. Yusa H, Kawamura F, Taniguchi T, Hirao N, Ohishi Y, Kikegawa T. High-pressure synthesis and compressive behavior of tantalum nitrides. *J Appl Phys*. 2014;115(10):103520. https://doi.org/10.1063/1.4867986

245. Delbari SA, Nayebi B, Ghasali E, Shokouhimehr M, Shahedi Asl M. Spark plasma sintering of TiN ceramics codoped with SiC and CNT. *Ceram Int*. 2019;45(3):3207–3216. https://doi.org/https://doi.org/10.1016/j.ceramint.2018.10.223

246. Russias J, Cardinal S, Fontaine J, Fantozzi G, Esnouf C, Bienvenu K. Bulk titanium nitride material obtained from SHS starting powder: Densification, mechanical characterization and tribological approach. *Int J Refract Met Hard Mater*. 2005;23(4):344–349. https://doi.org/https://doi.org/10.1016/j.ijrmhm.2005.05.013

247. Alexandre N, Desmaison-Brut M, Valin F, Boncoeur M. Mechanical properties of hot isostatically pressed zirconium nitride materials. *J Mater Sci*. 1993;28(9):2385–2390. https://doi.org/10.1007/BF01151669

248. Muchiri PW, Mwalukuku VM, Korir KK, Amolo GO, Makau NW. Hardness characterization parameters of Niobium Carbide and Niobium Nitride: A first principles study. *Mater Chem Phys*. 2019;229(September 2018):489–494. https://doi.org/10.1016/j.matchemphys.2019.03.001

249. Li D, Tian F, Duan D, *et al.* Mechanical and metallic properties of tantalum nitrides from first-principles calculations. *RSC Adv*. 2014;4(20):10133–10139. https://doi.org/10.1039/c3ra46734a

250. E. Török, A.J. Perry, L. Chollet WDS. YOUNG ' S MODULUS OF TiN , TIC , ZrN AND HfN * The Young ' s modulus of group IVB nitride and TiC films coated onto stainless steel substrates by reactive sputtering has been derived from their flexural resonance frequency . The values found for stoichiom. *Thin Solid Films*. 2000;153(1987):37–43. https://doi.org/https://doi.org/10.1016/0040-6090(87)90167-2

251. Sozal MSI, Tang W, Das S, *et al.* Electrical, thermal, and H2O and CO2 poisoning behaviors of PrNi0.5Co0.5O3-δ electrode for intermediate temperature protonic ceramic electrochemical cells. *Int J Hydrogen Energy*. 2022;47(51):21817–21827. https://doi.org/10.1016/j.ijhydene.2022.05.011

252. Sozal MSI, Li W, Das S, *et al.* Fabrication and preliminary testing of patterned silver cathodes for proton conducting IT-SOFCs. *Mater Adv*. 2024;1940–1951. https://doi.org/10.1039/d3ma00793f

VITA

SUPRABHA DAS

EDUCATION AND EXPERIENCE:

January 2020 – May 2024	Doctoral Candidate (Ph.D.) in Materials Science and Engineering, Florida International University, Miami, US.
January 2020 – July 2023	Master of Science (M.S) in Materials Science and Engineering, Florida International University, Miami, US.
May 2018-July 2018	Summer Research Intern, Indian Institute of Engineering Science and Technology, India.
July 2017 – August 2019	Master of Science (M.S) in Materials Science, University of Allahabad, India.
April 2014 – May 2017	Bachelor of Science (B.S) in Physics, University of Calcutta, India.

PUBLICATIONS AND PRESENTATION:

1. Suprabha Das, Andriy Durygin, Zhe Cheng. (2023)
   High entropy nitride ceramics and methods of synthesizing the same, US Patent 11,691,923 [87]
   https://patents.google.com/patent/US11691923B1/en
2. Suprabha Das, Diego Dubois, Md Shariful Islam Sozal, Yusuf Emirov, Borzooye Jafarizadeh, Chunlei Wang, Vadym Drozd, Andriy Durygin, Zhe Cheng
   "Synthesis and flash sintering of zirconium nitride powder", Journal of American Ceramic Society (2022) [6]
   https://doi.org/10.1111/jace.18421
3. Suprabha Das, Andriy Durygin, Vadym Drozd, Md Shariful Islam Sozal, Zhe Cheng.
   "Reaction Flash Sintering of Ternary Metal Nitrides", Journal of European Ceramic Society (2023) [227]
   https://doi.org/10.1016/j.jeurceramsoc.2023.11.079
4. Suprabha Das, Vadym Drozd, Andriy Durygin, Md Shariful Islam Sozal, Michael Cinibulk, Yong Ding, Yingdong Guan, Zhiqiang Mao, Zhe Cheng
   "Synthesis and Characterization of High Entropy Nitrides", (under preparation) (2023)

5. Amirali Eskandariyun, Suprabha Das, Diego Dubois, Andriy Durygin, Vadym Drozd, Zhe Cheng. [138]
   “Effects of processing conditions on flash sintering of commercial ZrN”, Journal of American Ceramic Society (2024)
   https://doi.org/10.1111/jace.19719
6. Md Shariful Islam Sozal, Wei Tang, Suprabha Das, Wenhao Li, Andriy Durygin, Vadym Drozd, Cheng Zhang, Borzooye Jafarizadeh, Chunlei Wang, Arvind Agarwal, Dong Ding, Zhe Cheng, [251]
   “Electrical, thermal, and H2O and CO2 poisoning behaviors of PrNi0.5Co0.5O3-δ electrode for intermediate temperature protonic ceramic electrochemical cells”, International Journal of Hydrogen Energy (2022)
   https://doi.org/10.1016/j.ijhydene.2022.05.011
7. Sozal, Md Shariful Islam; Li, Wenhao; Das, Suprabha; Jafarizadeh, Borzooye; Chowdhury, Azmal Huda; Durygin, Andriy; Drozd, Vadym; Wang, Chunlei; Cheng, Zhe*. (2024) [252]
   “Fabrication and Preliminary Testing of Silver Pattern Cathodes for Proton Conducting IT-SOFC”, Materials Advances (2024)
   https://doi.org/10.1039/D3MA00793F
8. Suprabha Das, Zhe Cheng, "Reaction Flash Sintering of Ternary Metal Nitrides",
   Materials Science & Technology (MS&T 2023), Ohio, October 2023. (Oral)
9. Suprabha Das, Zhe Cheng, "Synthesis and Characterization of High Entropy Nitrides",
   Materials Science & Technology (MS&T 2023), Ohio, October 2023. (Oral)
10. Suprabha Das, Zhe Cheng, "Reaction Flash Sintering of Ternary Metal Nitrides",
    FIU Graduate Research Symposium, Florida, March 2023 (Poster)
11. Suprabha Das, Zhe Cheng, "Reaction Flash Sintering of Ternary Metal Nitrides",
    FIU MME Graduate Research Symposium, Florida, February 2023. (Poster)
12. Suprabha Das, Zhe Cheng, "Reaction Flash Sintering of Ternary Metal Nitrides",
    47th International Conference and Exposition on Advanced Ceramics and Composites, Florida, January 2023. (Oral)
13. Suprabha Das, Zhe Cheng, "Synthesis and Characterization of High Entropy Nitrides",
    47th International Conference and Exposition on Advanced Ceramics and Composites, Florida, January 2023. (Oral)
14. Suprabha Das, Zhe Cheng, "Synthesis and Flash Sintering of Zirconium Nitride Powder",
    FIU MME Graduate Research Symposium, Florida, February 2022. (Poster)
15. Suprabha Das, Zhe Cheng, “Synthesis and Flash Sintering of Zirconium Nitride Powder",
    46th International Conference and Exposition on Advanced Ceramics and Composites, Florida, January 2022. (Oral)